

## ABSTRACT

BAI, SANZHONG. Grid Integration of Distributed Energy Storage Devices in DC and AC Distribution Systems. (Under the direction of Dr. Srdjan Lukic).

Energy storage plays a vital role in solving many challenges experienced by the power system, such as the integration of renewable energy sources, load leveling, power quality control, etc. Energy storage systems suitable for distributed storage applications typically produce a DC voltage. Thus the focus of this dissertation is the efficient control and integration of DC energy storage devices in DC and AC distribution systems.

DC distribution systems are still in their infancy; however, a number of applications are ideally suited for DC power distribution, including data centers, fast charging stations for electric vehicles, more electric ships and aircrafts, etc. Among these applications, the fast charging station is of particular interest because of the widespread adoption of plug-in hybrid electric vehicles (PHEV) and pure electric vehicles (EV). A network of gas-station-equivalent fast charging stations is of great importance for solving the so-called “range anxiety” issue. As with gas stations, it is expected that multiple chargers will be co-located to form a charging station. This layout allows for the fast charging station to make use of a common AC/DC rectifier stage. After studying the power demand of the fast charging station, the power delivery architecture is proposed with DC power distribution and energy storage integration. With the energy storage system to provide peak power, the AC/DC frontend for the charging station can be sized based on the average power demand which is substantially lower than the peak power demand.

Following the design of the fast charging station, the AC/DC frontend plays a vital role in the sense that it provides the DC bus that powers all the chargers. It is justified that the 12-

pulse diode rectifier is a suitable choice for the AC/DC frontend because of its high reliability and low cost. However, the 12-pulse diode rectifier suffers from relatively high level of current harmonics on the AC side. Traditional way to mitigate harmonic issues is to add separate filters (active or passive). In this dissertation, a novel approach is proposed to use the same DC/DC converter to integrate energy storage while simultaneously improving the power quality on both sides of 12-pulse diode rectifier. The first implementation of this approach utilizes the DC/DC converter to shape the DC side current drawn from the rectifier and thus indirectly eliminate AC side current harmonics. During this study, a new way to design the LC filters of the 12-pulse diode rectifier is developed, which results in substantially lower value of inductance and capacitance for the LC filter and lower harmonics on the AC side. Based on this result, the second implementation utilizes the DC/DC converter to inject virtual resistance into the LC filter and thus shape the rectifier output current. This implementation provides even better results in terms of harmonics elimination and minimizing VA rating of the DC/DC converter. It also provides the third functionality of the DC/DC converter, which is compensating the voltage ripple of the DC bus. Experiment and simulation results are given to verify all the presented statements.

For energy storage integration in AC distribution system, the goal is to find an efficient way to integrate dissimilar batteries into the grid. Since these batteries can be very different, they cannot be directly connected together to form a high voltage high capacity battery pack. The approach is to design DC/AC power converter that interface with each of the low voltage battery modules and form a module that includes energy storage device and power converter. A number of these modules can be linked together on the AC side of the power converter, to reach the required AC output voltage and directly interface with the grid. This approach

holds the promise of higher system level efficiency and simplicity than the two-stage solution typically used. The well-known H-Bridge topology is used for the DC/AC power conversion. When the H-Bridges are cascaded together, the independent control of each H-Bridge becomes challenging because all of them are linked together. Existing control strategies all need a central controller to directly control all the H-Bridges or communicate with local controllers located within the H-Bridge modules, which limits the modularity of the system. In this dissertation, a new control strategy for cascaded H-Bridges is proposed with no central controller. The control strategy for each H-Bridge is completely implemented in the local controller and there is no communication between these local controllers. Experiment results verified the effectiveness of this control strategy and a small scale community energy storage system (CES) is built and integrated into the Future Renewable Electric Energy Distribution and Management (FREEDM) system.

© Copyright 2013 by Sanzhong Bai

All Rights Reserved

Grid Integration of Distributed Energy Storage Devices in DC and AC Distribution Systems

by  
Sanzhong Bai

A dissertation submitted to the Graduate Faculty of  
North Carolina State University  
in partial fulfillment of the  
requirements for the degree of  
Doctor of Philosophy

Electrical Engineering

Raleigh, North Carolina

2013

APPROVED BY:

---

Dr. Srdjan Lukic  
Committee Chair

---

Dr. Alex Q. Huang

---

Dr. Subhashish Bhattacharya

---

Dr. Mo-Yuen Chow

**DEDICATION**

To my grandfather

Bai, Xinran

## **BIOGRAPHY**

Sanzhong Bai received his B.S. and M.S. degree in Electrical Engineering from Sichuan University, Chendu, China, in 2003 and 2006, respectively. Between 2006 and 2008 he was a Research Assistant in the Electric and Technology Institute of Sichuan University. He is currently pursuing his Ph.D degree in North Carolina State University, Raleigh, NC, USA. Since 2008, he has been a Research Assistant in the NSF funded Future Renewable Electric Energy Delivery and Management (FREEDM) systems center at North Carolina State University.

His primary areas of interest are power converters, energy storage systems and electric power qualities.

## ACKNOWLEDGMENTS

I would like to express my gratitude to my advisor, Dr. Srdjan Lukic, for his continuous support and guidance for the past five years. As a young professor, Dr. Lukic has shown that he is a capable advisor, a talent research partner, and a great friend. I feel deeply grateful and lucky to have this journey with him.

I would like to thank my committee members, Dr. Alex Q. Huang, Dr. Subhashish Bhattacharya, Dr. Mo-Yuen Chou and Dr. Xiangwu Zhang, for reviewing my dissertation and providing insightful comments and suggestions. I also would like to thank all the other faculties and staffs in the FREEDM systems center for their support and help.

I am glad I have joined the FREEDM systems center, not only because of the world-class research environment it provides, but also because of the great friends I have made here. I would like to thank my friends and research partners, Dr. Zeljko Pantic, Dr. Yu Du, Mr. Shane Hutchinson, Mr. Mark Lomaskin, and Mr. Youxi Shao, for their friendship and support. I also would like to thank all the other friends in FREEDM systems center including Dr. Jun Li, Dr. Tiefu Zhao, Dr. Xiaohu Zhou, Dr. Jiwei Fan, Dr. Wenchao Song, Dr. Zhigang Liang, Dr. Rong Guo, Dr. Yu Liu, Dr. Liyu Yang, Dr. Xiaopeng Wang, Dr. Jun Wang, Dr. Parkhideh Babak, Dr. Qian Chen, Dr. Zhengping Xi, Dr. Xijun Ni, Dr. Wencong Su, Dr. Edward Van Brunt, Dr. Pochih Lin, Ms. Zhan Shen, Mr. Xiao Bian, Mr. Arvind Govindaraj, Mr. Siddharth Ballal, Mr. Kibok Lee, Mr. Rui Gao, Mr. Rui Wang, Mr. Mohammad Etemadrezaei, Mr. Urvir Singh, Mr. Xu She, Ms. Huan Hu, Mr. Zhuoning Liu, Mr. Xunwei Yu, Mr. Gangyao Wang, Mr. Fei Wang, Mr. Yen-Mo Chen, Mr. Baek Seunghun, Ms. Mengqi Wang, Mr. Sumit Dutta, Mr. Kai Tan, Ms. Suxuan Guo, Mr. Haotao Ke, Mr.

Bharadwaj Vasudevan, Mr. Mingkui Wei, Mr. Xing Huang, Mr. Xingchen Yang, Mr. Habiballah Rahimi-Eichi, Mr. Li Jiang, Mr. Yalin Wang, Mr. Daniel Fregosi, Mr. Xiaomin Li and Mr. Xiaoqing Song. Thank you all for the friendship and support over the years.

I would like to express my great appreciation to all the family members, my grandparents, my parents, my aunt, my uncle, my sisters and brothers. You are the ones who define who I am and I am proud to be part of this family.

Finally, I would like to say thank you to my beloved wife, Qian Sun, for her love and support that gives me the courage to face any challenges I may encounter.

## TABLE OF CONTENTS

LIST OF TABLES .....	ix
LIST OF FIGURES .....	x
Chapter 1. Introduction .....	1
1.1 Energy Storage Technologies .....	2
1.2 Energy Storage Applications in Power Systems.....	4
1.2.1 Energy Storage with Renewable Energy Sources.....	4
1.2.2 Utility Energy Storage .....	5
1.2.3 Load-side Energy Storage.....	6
1.3 Issues with State-of-the-Art Distributed Energy Storage Systems and Contributions of this Dissertation .....	7
Chapter 2. DC Distribution System with Energy Storage Integration – A Fast Charging Station Design Case .....	10
2.1 Review of the Charging Methods .....	11
2.2 Study of the Power Demand from the Fast Charging Station.....	12
2.3 Proposed Fast Charging Station with DC Bus and Energy Storage System.....	17
2.4 Conclusions.....	22
Chapter 3. AC/DC Frontend Design for the Proposed DC Distribution System.....	24
3.1 Topology Selection for AC/DC Frontend.....	24
3.2 Efficiency Comparison between Proposed 12-pulse Diode Rectifier and PWM Rectifier .....	32
3.3 Traditional Approach to Integrate Energy Storage and Eliminate AC Side Harmonics .....	35
3.4 AC Harmonics Elimination by Profiling DC Rectifier Current for the 12-Pulse Rectifier .....	38
3.4.1 Analysis of the Principle for AC Harmonics Elimination by Profiling DC Rectifier Current .....	39

3.4.2	Existing Methods .....	42
3.5	Direct Current Shaping Approach to Integrate Energy Storage and Achieve AC Side Harmonics Elimination .....	44
3.5.1	Proposed Direct Current Shaping Approach.....	44
3.5.2	System Analysis and Parameter Optimization.....	47
3.5.3	Injected Current Flow .....	51
3.5.4	Control Strategy .....	52
3.5.5	Simulation and Experimental Results.....	55
3.6	Virtual Impedance Injection Approach to Integrate Energy Storage and Achieve both AC and DC Side Harmonics Elimination.....	68
3.6.1	Proposed Method-Virtual Impedance Injection.....	69
3.6.2	Simulation and Experiment Results.....	82
3.7	Conclusions.....	99
Chapter 4. Modular Design of Cascaded H-Bridge for Energy Storage Integration in AC Distribution System – Dissimilar Batteries Utilization in Community Energy Storage Systems .....		
		101
4.1	Approaches to Integrate Energy Storage into the Grid.....	104
4.1.1	Centralized Design of Energy Storage Integration and Its Drawbacks .....	104
4.1.2	Modular Design of Energy Storage Integration.....	106
4.2	Control of Cascaded H-Bridge Converters-A Review.....	110
4.3	Modular Design of a Cascaded H-Bridge Converter for Energy Storage Integration .....	117
4.3.1	Proposed Control Strategy to Have Independent Control of Each Module.....	119
4.3.2	Strategies for Active and Reactive Power Distribution .....	124
4.3.3	Modeling and Analysis of the Voltage Controller .....	132
4.3.4	Modeling and Analysis of the Current Controller .....	136
4.4	Experiment Verification.....	150
4.4.1	Setup 1: Concept Verification.....	151
4.4.2	Setup 2: Practical system implementation .....	157

4.4.3	Efficiency Test .....	165
4.5	Conclusions.....	170
Chapter 5.	Conclusions and Future Work.....	172
5.1	Summary of the Contributions.....	172
5.2	Future Work.....	175
REFERENCES	.....	177

## LIST OF TABLES

Table 2.1 Electrical Ratings of Different Charge Method (North America) .....	12
Table 2.2 Battery capacity of available EVs/PHEVs in the market .....	15
Table 2.3 Monte Carlo Simulation Results for Energy Storage Ratings .....	21
Table 2.4 Operation Performance of the Charging Station.....	22
Table 3.1 Comparison of the Diode Losses for Two Configurations (at 1.1MW) .....	30
Table 3.2 Comparison of the proposed diode rectifier and PWM rectifier .....	34
Table 3.3 Parameters of the AC/DC Rectifier for Simulations .....	57
Table 3.4 Parameters of the AC/DC Rectifier for Experiment.....	60
Table 3.5 Parameters of the Rectifier for Simulation .....	83
Table 3.6 Parameters of the Rectifier for Experiment .....	89
Table 4.1 Power commands for the simulation .....	131
Table 4.2 Parameters of the system for controller design.....	140
Table 4.3 Parameters of setup 1 .....	152
Table 4.4 Parameters of setup 2.....	160
Table 4.5 Parameters of setup for efficiency test.....	166
Table 4.6 Power consumptions of auxiliary components .....	170

## LIST OF FIGURES

Figure 2.1 Charging profile of Nissan Leaf with Terra 51 charger .....	14
Figure 2.2 Power demand of the charging station .....	17
Figure 2.3 Charging station architecture using AC bus.....	19
Figure 2.4 Charging station architecture using DC bus.....	19
Figure 3.1 fast charging station architecture with different AC/DC frontend .....	25
Figure 3.2 Typical input current waveform of 6-pulse, 12-pulse, and 18-pulse diode rectifier .....	28
Figure 3.3 Two types of configuration for 12-pulse diode rectifier .....	29
Figure 3.4 Power loss calculation results of one leg of the 1.1 MW PWM rectifier .....	33
Figure 3.5 Distribution system with DC side energy storage integration and AC side filters/compensators .....	36
Figure 3.6 Distribution system with AC side energy storage integration and AC side filters/compensators .....	36
Figure 3.7 Distribution system with AC side active compensator and energy storage integration .....	37
Figure 3.8 Proposed DC distribution system with energy storage integration and harmonic elimination .....	38
Figure 3.9 The 12-pulse diode rectifier.....	40
Figure 3.10 Construction of the AC input current for direct current shaping approach.....	41
Figure 3.11 Existing methods for shaping the rectifier current .....	43
Figure 3.12 Proposed method with parallel connected current sources.....	45
Figure 3.13 Configuration of the proposed AC/DC rectifier with current sources formed by two Buck-Boost converters.....	46
Figure 3.14 Equivalent circuit of the 12-pulse rectifier .....	48
Figure 3.15 Rectifier output voltage and current .....	49
Figure 3.16 Decoupling of the currents produced by the fundamental of .....	50
Figure 3.17 Equivalent circuit for the upper current source using the superposition principle .....	52

Figure 3.18 Equivalent circuit of the 12-pulse rectifier with the current sources included....	53
Figure 3.19 Control diagram of direct current shaping approach.....	54
Figure 3.20 Verification of optimized ESR .....	56
Figure 3.21 Simulation results with switching model of proposed system .....	58
Figure 3.22 Experimental Setup for direct current shaping approach .....	61
Figure 3.23 Comparison of line current and rectifier output current.....	62
Figure 3.24 Compensation current when the load current $I_L$ is 4.2A .....	64
Figure 3.25 Harmonics distribution with and without the current profiling when load current $I_L$ is 4.2A .....	64
Figure 3.26 Comparison of THD with and without current profiling.....	65
Figure 3.27 VA rating of the current sources $i_{s1}+i_{s2}$ .....	65
Figure 3.28 Power Factor as a function of load current with and without the current profiling .....	66
Figure 3.29 Rectifier efficiency as a function of load current with and without the current profiling.....	67
Figure 3.30 Active power injection for direct current shaping approach .....	67
Figure 3.31 Proposed method with parallel connected current sources.....	70
Figure 3.32 Construction of the AC input current for virtual impedance injection approach	72
Figure 3.33 Configuration of the proposed AC/DC rectifier with current sources formed by two buck-and-boost converters .....	74
Figure 3.34 Equivalent circuit of the 6-pulse rectifier with parallel connected current source and virtual resistors .....	74
Figure 3.35 Block diagram model of the 6-pulse rectifier equivalent circuit with virtual resistors .....	75
Figure 3.36 Equivalent circuit of the 6-pulse rectifier with parallel connected current source .....	76
Figure 3.37 Phasor diagram of the 6-pulse rectifier with virtual resistance injection .....	78
Figure 3.38 Phasor diagram of the 6-pulse rectifier with virtual impedance injection ( $VR_I>0$ ) .....	80

Figure 3.39 Block diagram model of the 6-pulse rectifier equivalent circuit with virtual impedance injection .....	80
Figure 3.40 Control diagram of the 12-pulse rectifier with parallel connected current sources .....	81
Figure 3.41 Comparison of proposed method (virtual resistor injection) and method in section 3.5 (direct current shaping).....	85
Figure 3.42 Experiment setup for virtual impedance injection approach.....	88
Figure 3.43 Comparison of line current and rectifier output current for light load (load current is 1.4A) .....	91
Figure 3.44 Comparison of line current and rectifier output current for heavy load (load current is 6.2A) .....	92
Figure 3.45 Harmonics distribution of line current with and without virtual resistance injection (load current is 6.2A) .....	93
Figure 3.46 Injected current $i_{s1}$ and $i_{s2}$ (load current is 2.2A).....	94
Figure 3.47 Comparison of line current THD with and without virtual resistance injection .	95
Figure 3.48 Comparison of load side output voltage ripple with and without active compensation .....	95
Figure 3.49 VA rating of the current sources .....	96
Figure 3.50 LC filter detuning compensation.....	97
Figure 3.51 Active power injection for virtual impedance injection approach .....	98
Figure 4.1 Overview of CES fleet layout.....	102
Figure 4.2 Simplified block diagram of a CES unit.....	103
Figure 4.3 Grid integration of centralized energy storage system .....	106
Figure 4.4 Grid integration of parallel connected energy storage modules .....	108
Figure 4.5 Grid integration of series connected energy storage modules.....	109
Figure 4.6 Generic Cascaded H-Bridge converter .....	111
Figure 4.7 Control strategy for cascaded H-Bridge: method I.....	112
Figure 4.8 Control strategy for cascaded H-Bridge: method II .....	113
Figure 4.9 Control strategy for cascaded H-Bridge: method III.....	114
Figure 4.10 System block diagram with centralized control strategy.....	115

Figure 4.11 Distributed control system with central controller and local controllers .....	117
Figure 4.12 Proposed modular design approach with distributed controllers .....	119
Figure 4.13 Power stage of the proposed system and its partitioning for controller design.	120
Figure 4.14 Proposed control strategy to have independent control of each module .....	122
Figure 4.15 Phasor diagram of the system quantities .....	126
Figure 4.16 Phasor diagram of the system with $v_{H2} \sim v_{Hn}$ in phase with $v_g$ .....	127
Figure 4.17 Example of two different ways to distribute active and reactive power among modules .....	129
Figure 4.18 Simulation result for two different power distribution strategies.....	131
Figure 4.19 Equivalent circuit of the 2 <sup>nd</sup> to n <sup>th</sup> modules .....	132
Figure 4.20 Average model of the H-Bridge .....	133
Figure 4.21 Average model of the 2 <sup>nd</sup> to n <sup>th</sup> module .....	134
Figure 4.22 Small signal model of the circuit that is of interest for 2 <sup>nd</sup> to n <sup>th</sup> module .....	134
Figure 4.23 Proposed controller for the 2 <sup>nd</sup> to n <sup>th</sup> module .....	135
Figure 4.24 Equivalent circuit of the first module .....	137
Figure 4.25 Average model of the first module .....	137
Figure 4.26 Small signal model of the circuit that is of interest for the first module .....	138
Figure 4.27 Bode plot of the control to output transfer function of the system.....	141
Figure 4.28 Bode plot of the delay caused by the digital controller .....	143
Figure 4.29 Proposed controller for the first module.....	143
Figure 4.30 Block diagram of the first module with double loop control .....	144
Figure 4.31 Bode plot of the control to output transfer function of the inner loop .....	145
Figure 4.32 Loop gain of the inner loop for stiff and weak grid .....	147
Figure 4.33 Bode plot of the close loop transfer function of the inner loop.....	148
Figure 4.34 Loop gain of the outer loop for stiff and weak grid .....	149
Figure 4.35 System configuration of experimental setup 1 .....	152
Figure 4.36 Picture of experimental setup 1 with three H-Bridge modules and single controller .....	153
Figure 4.37 Output power step change: low to high.....	154
Figure 4.38 Output power step change: high to low .....	154

Figure 4.39 Change of power distribution between modules (power commands for the three modules change from 30W, 50W and 70W to 60W, 50W and 40W, respectively) .....	156
Figure 4.40 Change of operating mode: discharging to charging .....	156
Figure 4.41 Change of operating mode: charging to discharging .....	157
Figure 4.42 System overview of the demonstration setup .....	158
Figure 4.43 Webpage hosted in SCADA server for controlling of the CES unit .....	159
Figure 4.44 System configuration of experimental setup 2 .....	159
Figure 4.45 Pictures of experimental setup 2 with four H-Bridge modules and distributed controllers .....	161
Figure 4.46 Detailed view of the four H-Bridge modules in setup 2 .....	162
Figure 4.47 Step change of output power from 200W to 400W .....	163
Figure 4.48 Change of operating mode: from charging to discharging .....	164
Figure 4.49 Step change of output power from 180W to 360W with reactive power injection .....	164
Figure 4.50 Configuration of the setup for efficiency test .....	165
Figure 4.51 Reinforcement of the PCB traces .....	166
Figure 4.52 Efficiency of the H-Bridge with different load and switching frequency .....	167
Figure 4.53 Efficiency of the H-Bridge with different load and DC side voltage .....	168
Figure 4.54 Efficiency of the H-Bridge with different modulation index ( $R_L=1.67 \Omega$ ) .....	169

## Chapter 1. Introduction

For more than a century, the AC power system has been serving the globe with relatively high quality and reliable electricity. The AC transmission and distribution system will continue to be the backbone of electric power system in the foreseeable future. However, the existing power system is facing the greatest challenge in its history now. One challenge is the continuously growing power demand and environmental impacts caused by traditional power generation. For the past several decades, electric energy has been the world's fastest growing form of end-use energy consumption [1]. Unfortunately, most electricity currently is generated from fossil fuels. All types of fossil fuels have two things in common: they will be depleted eventually and they all create carbon dioxide when burned. The worries about the limited availability of fossil fuels and the environmental impact it causes have driven people to utilize alternative energy resources. Currently, renewable energy is the fastest growing source of electricity generation [1]. Although renewable energy alleviates the environmental and energy security issues of fossil fuels, it could be problematic to integrate renewable energy into grid due to their intermittent and stochastic nature. Large scale integration of renewable energy into weak grid could also cause unacceptable power fluctuations and thus severely deteriorate the power quality [2]–[5]. To address this issue, energy storage can be used to mitigate the intermittency of renewable energy and improve the power quality [5], [6].

Another challenge the power system faces is the demands for a more flexible and controllable power system. In response to this challenge, flexible AC transmission system (FACTS) has been introduced to gain more control of power system and improve power

quality and reliability. Traditional FACTS devices can only supply reactive power and thus the functionality is limited. With the integration of energy storage systems the FACTS devices can supply both reactive power and active power, and thus go above and beyond the functionalities of traditional FACTS systems [7], [8].

In this chapter, different types of electric energy storage technologies and their applications in power system are summarized in section 1.1 and 1.2, respectively. Issues with current distributed energy storage systems are identified in section 1.3, with the contributions of this dissertation being introduced as well.

## **1.1 Energy Storage Technologies**

Depending on the applications, energy storage could have many different forms. Different energy storage technologies have different characteristics, as summarized in [8]–[12], and briefly listed here.

Pumped-Hydro storage is the largest energy storage in terms of power level. Existing facilities are rated up to 1000 MW [11]. Pumped hydro facilities pump water from lower reservoir to higher reservoir during off-peak hours, and release the water back down to the lower reservoir, passing through hydraulic turbines to generate electricity. The implementation of pumped hydro storage plants is limited because of the high construction cost, long construction time, and large amounts of land that is needed for the reservoirs. In addition, pumped hydro is site-specific, and is not very well suited for distributed storage applications.

Compressed Air Energy Storage (CAES) uses excess power during off-peak hours to compress air into an underground reservoir, and release the air to burn with fuel to drive power generator. CAES is the only other commercially available technology (besides pumped-hydro) able to provide very large power deliverability (above 100 MW for single unit). This technology has the same issues as pumped hydro in distributed installations.

Regenerative fuel cells store and release energy through a reversible electrochemical reaction between two electrolytes. Its storage capacity is mainly determined by the size of the electrolytic tanks, and thus makes it at the large scale energy storage range. Existing facilities have above 10 MW power and above 100 MWh capacities [11].

Battery energy storage also utilizes electrochemical reaction to store and release energy. There are many types of battery technologies like lead-acid, Lithium-ion, and sodium sulfur. Traditionally, lead-acid batteries are widely used due to its low cost. In recent years, Lithium-ion battery has gained more interest because of its high power/energy density and decreasing cost. Almost all electric vehicles in the market use Lithium-ion batteries as the main storage.

Superconducting Magnetic Energy Storage (SMES) stores electric energy in the magnetic field created by the DC current flowing through a superconducting coil. SMES has very high efficiency for storing electricity (larger than 95%). It can also provide very high power for a short period of time, with negligible response time. The superconducting coil of SMES needs to be cryogenically cooled and thus results in high construction and operating costs.

Flywheel energy storage stores energy in the form of kinetic energy through accelerating a rotor or disk up to a high speed. The flywheel is coupled with an electrical machine which

acts as a motor to drive the wheel during charging and acts like a generator to transfer the kinetic energy into electricity. The stored energy is proportional to the square of the angular speed of the rotor. Thus advanced composite materials are used for the rotor to lower its weight and allow for higher operating speeds. Flywheel energy storage has high power density and high cycle life, and found its applications mostly in the auto and aerospace industry.

Capacitors and electrochemical double layer capacitors (also called supercapacitors or ultracapacitors) store electric energy by accumulating positive and negative charges on two parallel electrode plates which are separated by insulating dielectric. The stored energy in a capacitor is proportional to the capacitance and the square of the applied voltage. The capacitance of a capacitor is proportional to the permittivity of the dielectric, the area of the plates, and inversely proportional to the distance between the plates. Capacitors are generally used for high power short term applications.

## **1.2 Energy Storage Applications in Power Systems**

Energy storage systems have found their place in many applications to improve and extend utility services. They can be roughly categorized into three types, as presented in the following sections.

### **1.2.1 Energy Storage with Renewable Energy Sources**

Nowadays, renewable energy sources are becoming more and more popular due to their clean nature. Among various renewable energy sources, wind and solar power are the fastest growing ones. Wind power sees over 20% annual capacity increase, with a global cumulative

installation capacity of 238GW as of 2011 [13]. For the Photovoltaic energy (PV), the growth rate reached almost 70% at 2011, with a global cumulative installation capacity of 69GW as of 2011[14]. While having more renewable energy in the power system is a positive development, the intermittent and stochastic nature of renewable energy sources has brought a number of challenges to the existing power system. It has been estimated that for a stable power system, every 10% wind penetration will need a balancing power from other generation sources that counts for 2%-4% of the installed wind power capacity [12]. Energy storage has been proved to be a good solution to this problem [15]–[19]. Usually, the energy storage is tightly coupled with the renewable energy sources to stabilize the intermittent and stochastic output power. Additional benefits include load leveling, voltage and frequency regulation, etc.

### **1.2.2 Utility Energy Storage**

Utility scale energy storage systems usually have MW/MWh level power and capacity, and thus have the capability to substantially change the power system operation. In [10], an example is given to show that the energy storage could reduce operating cost, mitigate congestion, and improve the security of the power system.

Load leveling is another function that energy storage can provide. By storing electricity during off-peak hours and discharging the stored energy during peak hours, the peak power demand from the power plant is reduced. This in turn could lead to a slow-down in the need to construct more grid infrastructure. Similarly, energy storage can also be used for energy arbitrage. Energy arbitrage refers to earning a profit by storing electricity when the price is low and sell it when price is high. Traditionally, pumped hydro storage is used to perform

this function. Recently, the concept of using the energy stored in plug-in vehicles' batteries as the source of power for energy arbitrage (i.e. vehicle-to-grid) has gained interest. While a single electric vehicle has very limited energy storage capacity, the electric vehicle fleet as a whole could form an utility scale energy storage and introduce a new energy trading market [20].

Utility integrated energy storage can also be used to improve power quality. In comparison with traditional power system regulation, the energy storage system can provide much faster response and precise control. Many applications have been proposed that make use of FACTS devices (STATCOM, DVR, etc.) or Active Power Filters (APF) to provide voltage and frequency regulation, compensate voltage sags, eliminate harmonics, and so on [7], [21]–[23]. These applications open the possibility to build a more flexible, controllable and reliable power system.

### **1.2.3 Load-side Energy Storage**

Load side energy storage systems have been used for decades as Uninterruptable Power Supply (UPS) or Standby Power Supply (SPS) to provide power to critical loads [24]–[26]. Besides this basic function, load side energy storage is also used to smooth the load profile and provide peak shaving. In [27] it shows that by adding a fairly small energy storage, the peak power demand from the grid is substantially reduced and the grid sees a very smooth load instead of a very dynamic power demand with fast changing spikes. The load side energy storage could potentially serve the same role as utility energy storage. As mentioned earlier, the storage in electric vehicle is load side energy storage but it could feed power back

to grid. And a fleet of electric vehicles could form utility scale energy storage and perform corresponding functionalities.

### **1.3 Issues with State-of-the-Art Distributed Energy Storage**

#### **Systems and Contributions of this Dissertation**

There are two parts of this dissertation, dealing with energy storage integration in DC and AC distribution systems, respectively. It is worthwhile to mention that the electric energy storage devices that output DC voltage (batteries, capacitors, fuel cells, etc.) are the focus of this dissertation.

Traditionally, energy storage integration and power quality control (for both AC and DC side) are two independent applications. To have both functions, the energy storage system and power quality control devices are added separately [19], [28], [29]. There are some applications ([7], [21]–[23], [30]) that utilize the AC side active compensator (APF or STATCOM) as the energy storage interface. But they are not applicable to DC distribution system. In this dissertation, a fast charging station for EVs/PHEVs is first presented as a design case of DC distribution system. It is justified that the architecture based on the 12-pulse diode rectifier is a cost effective and robust approach to providing a common DC bus at 1 MW power rating. The main issue with low-pulse rectification is the unacceptable harmonic content, therefore two novel solutions specific to the 12-pulse diode rectifier are proposed. The first approach utilizes current sources to directly shape the rectifier output current, while the second approach uses virtual resistance injection to profile the rectifier output current. With rectifier output current being profiled to specific shape, the AC side

current harmonics will be reduced. The hardware that is used to do current profiling and virtual resistance injection can also be used to integrate energy storage and compensate DC side voltage ripple. Therefore, the system structure remains simple which is desirable for improved reliability and for minimizing the construction and maintenance costs.

For the AC side energy storage integration, the focus of this dissertation is to enable efficient modularization of the energy storage system. It is important to have modular design for the energy storage systems because the traditional centralized design has many drawbacks. To begin with, the centralized energy storage system needs to assemble a large number of energy storage cells into one unit to get sufficient voltage and capacity. To do this, it is desirable to have identical energy storage cells, which is difficult in practice. Moreover, the cells tend to degrade differently during their cycle lives. This brings serious problems to the system. If the cells are connected in parallel, they will discharge power into the weakest or lowest voltage cell instead of delivering power to the load. If the cells are connected in series, the current capacity of the energy storage system will be limited by the current capability of the weakest cell; in addition, a failure by a single cell in either parallel or series connection could render the whole system unusable. Another drawback of centralized energy storage system is that it lacks the flexibility to easily expand the system, or the system needs to be over-designed to accommodate future needs.

Modular design of energy storage system solves all of the aforementioned problems. Because each module has independent local controller, dissimilar or even different types of storage modules can be seamlessly integrated to act as a single unit. This opens the gate to

some new applications, such as the secondary use of reclaimed hybrid and electric vehicle batteries [31].

In this dissertation, a new control strategy is proposed to have modular design of cascaded H-Bridge. By using cascaded H-Bridge, low voltage energy storage modules can be used to get sufficient voltage to directly interface with the grid. Since only one stage of power conversion is needed, the system efficiency is maximized. The power flow from each energy storage module is independently controllable, so dissimilar or different types of energy storage devices can be integrated into the same system.

The remainder of this dissertation is organized as follows: in chapter 2, the design of fast charging station is presented as a typical DC distribution system. The AC/DC frontend for the fast charging station is investigated in chapter 3. The 12-pulse diode rectifier is selected as a suitable choice for this application. Two different approaches are presented to use the same DC/DC converter to integrate energy storage system and improved power quality of the 12-pulse diode rectifier as well. In chapter 4, the modular design of cascaded H-Bridge is presented to integrate dissimilar batteries into the grid. Conclusions are drawn in chapter 5 and future work is proposed as well.

## **Chapter 2. DC Distribution System with Energy Storage Integration – A Fast Charging Station Design Case**

Availability of reliable and inexpensive semiconductor devices has led to numerous power electronics intensive industrial loads requiring DC power supply for operation. When a number of DC powered loads are in proximity, it becomes viable for them to share a common DC bus. Many such systems benefit from local DC storage to (1) reduce the power demand from the grid, (2) provide backup power, and (3) store locally-generated renewable power rather than feeding it back to the grid. Local DC distribution has been considered for data centers [32], more electric ships and aircrafts [33]. Another potential application is the power distribution system for fast charging stations, which is the focus of this chapter.

With the introduction of electric vehicles (EV) and plug-in hybrid electric vehicles (PHEV) by major car manufacturers, electrically propelled cars are becoming more viable. One of the main roadblocks to the widespread adoption of these vehicles is said to be the so-called range anxiety, resulting from the limited ability to recharge electric vehicles in a time commensurable with filling the tank of a petroleum-powered vehicle. Therefore, there is a need to design fast chargers that can quickly replenish the charge in an EV/PHEV battery. And a network of fast charging stations is necessary to accelerate the mainstream acceptance of EVs/PHEVs. The focus of this chapter is to design a fast charging station that can replenish the batteries in a time comparable to tank filling on conventional vehicles, while

minimizing the strain on the grid by introducing energy storage. The charging methods are first reviewed in section 2.1 to determine the power level of the chargers. The power demand of the fast charging station is studied in section 2.2, showing that the introduction of energy storage substantially reduces the peak power requirement and therefore the grid tie rating requirement. The power delivery architecture for the fast charging station is proposed in section 2.3 and some conclusions are drawn in section 2.4.

## **2.1 Review of the Charging Methods**

Appropriate power levels for individual fast chargers have recently become a topic of some debate. Different standards have been proposed and are still under developing [34], [35]. Take the SAE J1772 standard as an example. The 2001 revision of this standard defines three levels of charging, AC level 1, AC level 2 and DC charging [34]. When this standard was adopted in 2010, it only standardized the AC level 1 and AC level 2 charging method, with the charging power of AC level 2 being extended to 19.2 kW. The 2012 version of this standard adds DC level 1 and DC level 2 charging. The AC level 3 and DC level 3 charging is still under development. Table 2.1 gives a summary of the charging methods that have been standardized or proposed by SAE J1772. From this table, it can be seen that the charging power varies substantially, which will inevitably result in different charging time for a certain battery. While it is acceptable to charge the EVs/PHEVs for several hours during night or during work time, the focus here is the fast charging (or ultra-fast charging as in other literatures) which allows the shortest possible charging time. The goal is to design a gas station equivalent fast charging station that can be constructed in highway rest areas and city

convenience points. With this in mind, the only charging method that suits this application is the DC level 3 charging configuration, which has a charging power of up to 240 kW. At this power level, the 80% charging time of a 24 kWh battery is around 5 minutes, and about 12 minutes for a 48 kWh battery [36].

Table 2.1 Electrical Ratings of Different Charge Method (North America)

Charge Method	Nominal Supply Voltage (Volts)	Max. Current (Amps-continuous)	Max. Power
AC Level 1	120 V AC, Single phase	16 A	1.9 kW
AC Level 2	240 V AC, Single phase	80 A	19.2 kW
AC Level 3 (TBD)	Single phase and 3-phase	>80 A	>20 kW
DC Level 1	200-500 V DC	80 A	40 kW
DC Level 2	200-500 V DC	200 A	100 kW
DC Level 3 (TBD)	200-600 V DC	400 A	240 kW

At DC level 3 charging, the power level of the fast charging station could easily go beyond MW level, considering that each fast charging station will have multiple chargers. At this power level, the power delivery architecture becomes critical to ensure a robust, cost effective and easy-to-construct system.

## 2.2 Study of the Power Demand from the Fast Charging Station

To design the power delivery architecture of the fast charging station, the power demand during the charging process needs to be identified first. A 50 kW charger (Terra 51) manufactured by ABB along with Nissan Leaf EV are tested to get the charging profile of state of the art EV. The charger follows the CHAdeMO standard [35]. According to this

standard, the charging process involves several stages and there is communication between electric vehicle supply equipment (EVSE) and battery management system (BMS) at different stages during charging to ensure high reliability and safety. A brief summarization of the charging process is given here:

(1) *Preparation for charging:* At this stage the EVSE and the BMS will exchange information. The BMS will report the battery information, such as the voltage limit, battery capacity, and acceptable maximum charging current. The EVSE will then check if it can charge the battery. If the answer is positive, the EVSE will let the BMS know its maximum output voltage and current and the BMS will double check the compatibility. After the BMS confirms the compatibility, it will send out the charging permission signal. Upon receiving this signal, the EVSE will initiate the charging procedure by running an isolation test to prevent potential fault conditions.

(2) *Charging:* At this stage the charging begins with the BMS sending a current command based on the measured battery state of charge (SoC), temperature, and other conditions. The EVSE will then deliver the commanded current.

(3) *End of charging:* The charging process is terminated if the BMS sends out zero current command. Should any abnormal conditions occur during charging, both the EVSE and the BMS can terminate the charging process.

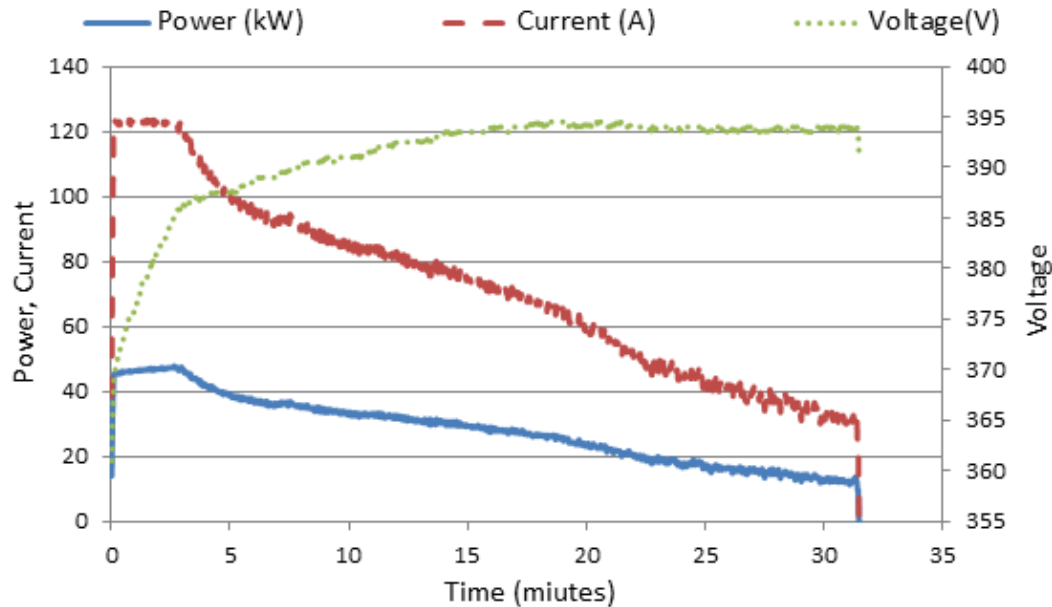


Figure 2.1 Charging profile of Nissan Leaf with Terra 51 charger

Figure 2.1 shows charging profile of the Nissan Leaf EV 24 kWh Li-ion battery by using the Terra 51 charger. The battery state of charge (SoC) is 10% initially, and 80% at the end of charge. The charging power has a peak value of 44.8 kW, with the average of 23.5 kW. The highly dynamic charging power profile is caused by the conservative charging strategy adopted by the manufacturer. The constant current charging only takes a few minutes, followed by a constant voltage charge. The charging profile will be a function of the battery initial state of charge, battery temperature, ambient temperature, battery state of health and other factors. The charging profile is proprietary to the manufacturer, and cannot be directly controlled by the user.

This test result gives us an idea of the charging profile of a state of the art charger and EV. However, the fast charging station proposed here will have DC level 3 charging method

(with 240 kW chargers) which has much higher charging power. There is no real world operating data available for such a fast charging station. Therefore, it is necessary to make assumptions based on available information and simulate the operation of the fast charging station.

As discussed in the beginning of this chapter, to have fast charging DC level 3 charging method which has 240 kW charging power is necessary. On the battery side, the maximum capacity needs to be determined. By summarizing the battery capacity of available EVs/PHEVs in the market, as shown in Table 2.2, it is clear that most of the EVs/PHEVs have less than 25 kWh battery pack. Tesla Model S has the highest battery capacity, which has 60 kWh for the base model and 85 kWh for upgraded model. Without losing generality, 60 kWh will be used as the maximum battery capacity.

Table 2.2 Battery capacity of available EVs/PHEVs in the market

<b>Manufacturer</b>	<b>Model</b>	<b>Vehicle type</b>	<b>Battery Capacity</b>	<b>Nominal Battery Voltage</b>
Toyota	Prius Plug-in 2013	PHEV	4.4 kWh	207.2 V
Ford	C-Max Energi 2013	PHEV	7.6 kWh	300 V
Mitsubishi	i-MiEV 2012	EV	16 kWh	330 V
GM	Chevrolet Volt 2013	PHEV	16.5 kWh	355.2 V
Honda	Fit EV 2013	EV	20 kWh	331 V
Ford	Focus Electric 2013	EV	23 kWh	325 V
Nissan	Leaf 2013	EV	24 kWh	364.8 V
Toyota	RAV 4 EV 2013	EV	41.8 kWh	386 V
Tesla	Model S 2013	EV	60/85 kWh	400 V

To conduct simulations of the operation of the fast charging station, the assumptions made are summarized here:

(1) There are 10 chargers in the fast charging station.

(2) Battery State of Charge (SoC) range is 20%-50% when the EV/PHEV arrives the charging station (normally distributed with the mean of 35% and standard deviation of 7.5%).

(3) Battery voltage is linearly proportional to battery SoC, and battery voltage is 80% of rated voltage when SoC is zero.

(4) Battery capacity range is between 5 kWh-60 kWh (normally distributed with the mean of 32.5 kWh and standard deviation of 13.75 kWh).

(5) Charge rate is between 3C-5C (normally distributed with the mean of 4C and standard deviation of 0.5C). However, the maximum power is limited by the charger (with 240 kW rated power). For example, for 60 kWh battery the maximum charging rate is limited to 4C. Charging rate below 3C is not considered as fast charging and is not available in this charging station.

(6) The efficiency of the power transformation is not considered.

(7) All chargers will be working all the time except for the interval between one vehicle leaving and next vehicle starting to charge, which takes 3 minutes.

Based on these assumptions, a preliminary simulation of the operation of this system is performed to get the profile of the power demand. Figure 2.2 is the simulation result which gives the power demand of the fast charging station in a cycle of 12 hours' operation. It should be mentioned that this scenario based on the assumptions above is going to happen in

reality, however, it is unlikely that it will last for 12 hours. In fact this scenario is expected to represent the worst case scenario that occurs during the peak use of the fast charging station.

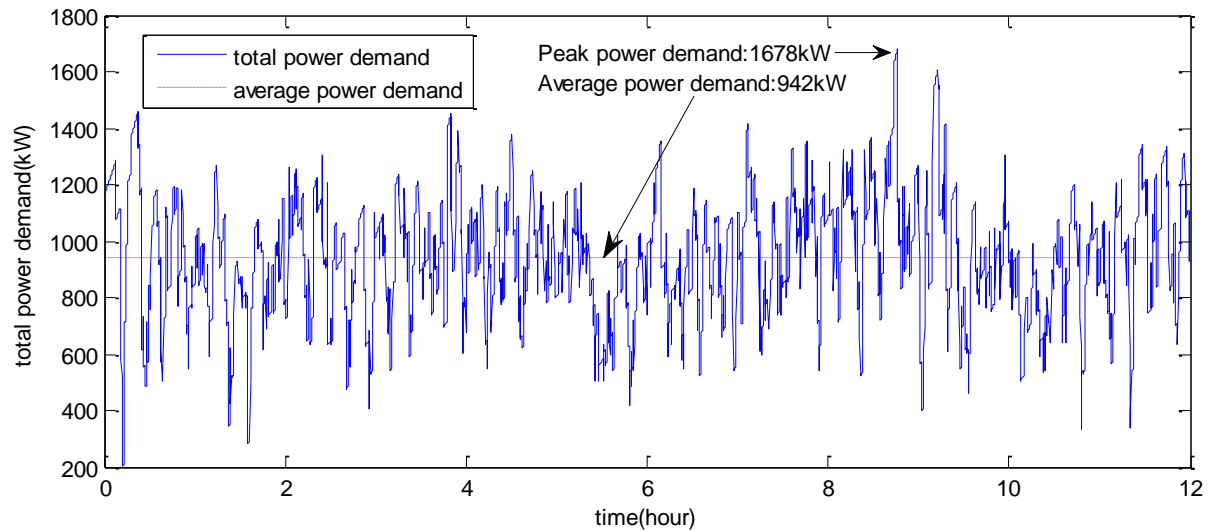


Figure 2.2 Power demand of the charging station

From Figure 2.2 it can be seen that the average power demand (942 kW) is significantly lower than the peak power demand (1678 kW). This profile suggests the possibility to ‘smooth’ the power demand and thus substantially reduce the grid tie capacity.

## 2.3 Proposed Fast Charging Station with DC Bus and Energy

### Storage System

As studied in section 2.2, the power demand of the fast charging station is very dynamic with the average power demand much lower than the peak power demand. To smooth out the power demand, a straightforward way is to size the grid tie at the average power demand

level and use energy storage to provide peak power demand. The energy storage will provide extra power when power demand is higher than the grid tie capacity, and will be charged when power demand is lower than the grid tie capacity.

A bus is a necessity in this system to enable energy sharing between chargers. Figure 2.3 and Figure 2.4 give two candidate architectures based on AC bus and DC bus, respectively. From the practical point of view, the AC bus based system is preferred because AC distribution system has been used for years and there are well developed standards and technologies available. However, DC distribution system provides a more convenient way to integrate renewable energy sources. Because both the sources and the DC loads are interfaced to a common DC bus, it requires fewer stages of power conversion and thus reduces losses and hardware costs. Moreover, the DC system utilizes one AC/DC converter instead of 10 smaller ones in the AC system, which is beneficial in terms of both efficiency and cost. So the DC bus based architecture is chosen for the charging station in question.

Some parameters need to be determined for the charging station, as given in Figure 2.4. For the transformer primary voltage, 4160 V is recommended for plants with loads of less than 10 MVA [37]. For the secondary voltage and the DC bus voltage, application oriented considerations need to be taken into account. Generally, for high power load, higher voltage level is preferred to reduce the current. But for this application, the output voltage of the charger could be as low as 207V (as seen in Table 2.2). If higher DC bus voltage is used, the charger would have to use a transformer to match the voltage level, which will significantly complicate the topology of the charger and increase the hardware cost. Therefore, the 480V line-to-line grid tie is considered, which gives 678V on the DC bus under ideal condition.

Based on the simulation result as given in Figure 2.2, the power rating of the AC/DC converter is sized as 1.1 MW, which is slightly higher than the average power demand.

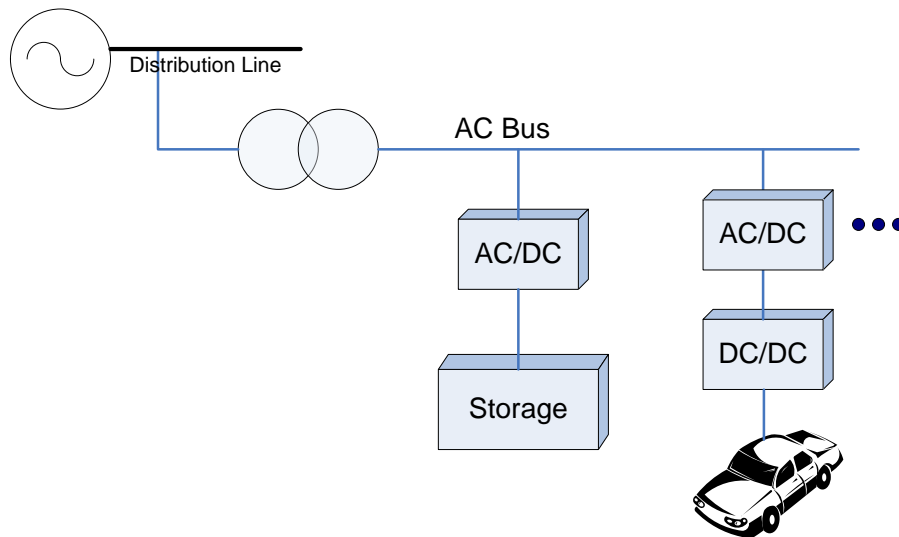


Figure 2.3 Charging station architecture using AC bus

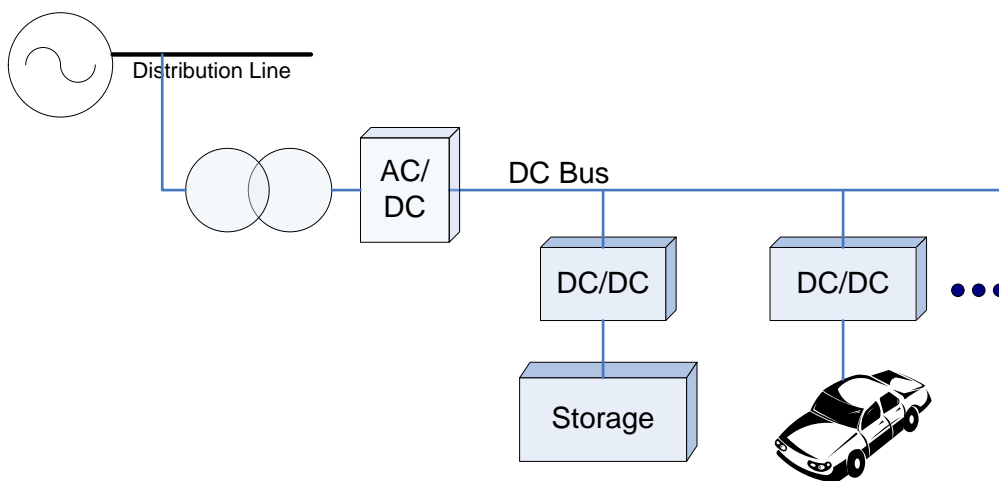


Figure 2.4 Charging station architecture using DC bus

Another important component in this system is the energy storage, which has a significant impact on the load shape. A simulation was conducted to determine a proper capacity of the energy storage. The scenario for this simulation is that 10 vehicles, with different arrival time, come to the charging station for battery charging. The simulation ends when all 10 vehicles finish charging. Assumptions (1)-(6) in section 2.2 still apply here, with additional assumption that vehicle arrival time is between 0-5 minutes (normally distributed with the mean of 2.5 minutes and standard deviation of 1.25 minutes). During the simulation, if the power demand exceeds available power from DC bus, the extra power needed which should be provided by energy storage will be recorded, and finally get the needed storage power and capacity rating. Monte Carlo method is used here to get statistical results, as given in Table 2.3. The results from each row of the table are based on 1000 simulations. For both the storage power and capacity, the mean value is much lower than the maximum value. So it is not reasonable to size the storage with the maximum value to guarantee 100% satisfaction. Instead, sizing the storage based on the mean value would be much more cost efficient. The mean value for needed storage capacity is roughly 13 kWh, and 170 kW for needed storage power. With this capacity-power combination, the best choice for the energy storage is ultracapacitor. Because there will be a large voltage drop as the ultracapacitor discharges, it is assumed that only 50% of the voltage range is usable due to the limitations of the power electronics. With the 50% of the capacitor voltage range in use, 75% of the available energy is accessible. Based on the results from Table 2.3, the capacity is chosen as 20 kWh, with 15 kWh are usable. The power limitation for ultracapacitors comes from the power electronics

since ultracapacitors can be used at very high discharge rates, much above the 10C. According to Table 2.3, the DC/DC converter for the ultracapacitor will be sized at 180 kW.

With the configurations as stated above, and assumption (1)-(6) as given in section 2.2, the operation of this charging station can be simulated. Table 2.4 summarized the simulation results. Each simulation simulates a 12-hour operation of the charging station. It can be seen that with relatively small storage system (20 kWh with 15 kWh being usable) and AC/DC converter (1.1MW), more than 98% of the power demand is satisfied. The percentage of customers been delayed is pretty high, however, the average delayed time is no more than 10 seconds.

Table 2.3 Monte Carlo Simulation Results for Energy Storage Ratings

No.	Needed storage capacity (kWh)			Needed storage power (kW)		
	max.	mean	median	max.	mean	median
1	66.68	13.01	9.72	646.81	170.18	163.58
2	88.79	12.77	8.51	741.20	166.96	145.62
3	84.15	12.88	9.42	779.07	169.18	155.38
4	72.07	12.63	8.59	694.85	166.59	144.60
5	74.62	13.42	10.13	698.88	173.48	159.28

A further Monte Carlo simulation shows that if there is no energy storage, only 93.7% of the power demand can be delivered, and the average delayed time is 35.7 seconds (average value based on 10 operation cycles).

Table 2.4 Operation Performance of the Charging Station

No. of simulation	Average power demand (kW)	Delivered power over total power demand	Total customer served	Percentage of customers been delayed	Max. delay time(sec)	Average delay time(sec)
1	954	98.78%	515	66.99%	142	10.0
2	936	98.94%	516	63.95%	127	9.1
3	942	98.97%	511	61.64%	100	9.8
4	935	99.10%	516	65.50%	87	8.1
5	924	99.53%	511	59.10%	77	4.7

## 2.4 Conclusions

In this chapter, the importance of fast charging station infrastructure in the mainstream acceptance of EV/PHEV is identified. With the goal of designing a gas station equivalent fast charging station that can be constructed in highway rest areas and city convenience points, the power demand of such charging station is first studied. The results show that the average power demand of the fast charging station is much lower than its peak power demand. Therefore, a fast charging station architecture that has a common DC bus and energy storage integration is proposed. With the common DC bus, multiple advantages can be achieved: (1) possible efficiency and cost savings from using a single centralized rectifier stage; (2) seamless integration of local storage on the DC bus that can support the entire charging station; (3) integration of renewables such as photovoltaic arrays to offset the power demand of the charging station; (4) more efficient energy sharing between EV batteries due to fewer conversion stages. With the integration of energy storage system, the power demand from the

grid could be substantially reduced. As a result, the demand charges will be reduced and the grid side load profile is much smoother. It is shown that with a 1.1 MW AC/DC rectifier and 20 kWh energy storage, the DC bus can support 10 DC level 3 chargers with rated power of 240 kW. With this configuration the charging time for some customers may be longer than desired, but the delay time is acceptable (average delay time is less than 10 seconds).

## **Chapter 3. AC/DC Frontend Design for the Proposed DC Distribution System**

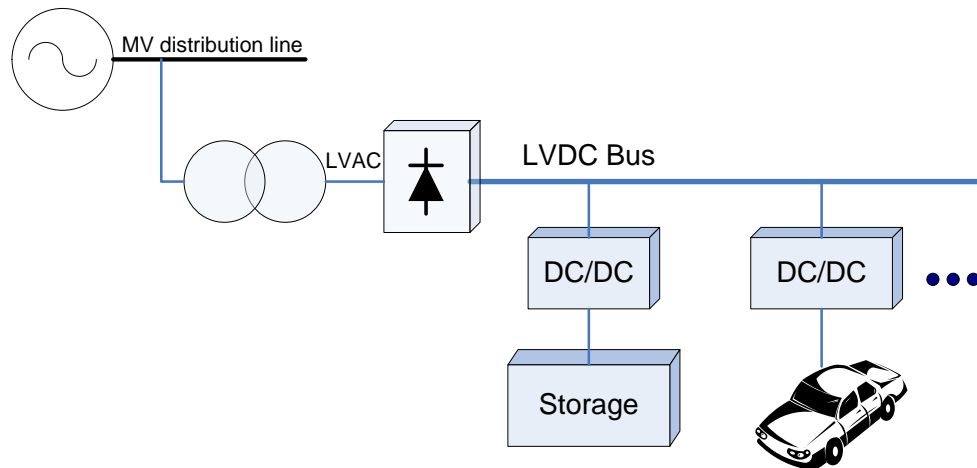
In the previous chapter, the power delivery architecture of the fast charging station is proposed. An open question in designing the fast charging station is the optimal choice for the AC/DC and DC/DC converter stages. A thorough tradeoff study for both isolated and non-isolated DC/DC topologies was presented in [38] and [39]. The focus of this chapter is the conversion stage that delivers the common DC bus to the system. In section 3.1, the topology for the AC/DC frontend is selected. The efficiency comparison between the selected 12-pulse diode rectifier and active PWM rectifier is given in section 3.2. Traditional approaches to integrate energy storage and eliminate harmonics are discussed in section 3.3. In section 3.4, the concept of eliminating AC side harmonics by profiling DC side currents is reviewed. A new method to implement this concept is presented in section 3.5, while in section 3.6 this method is modified to have better performance. Conclusions are drawn in section 3.7.

### **3.1 Topology Selection for AC/DC Frontend**

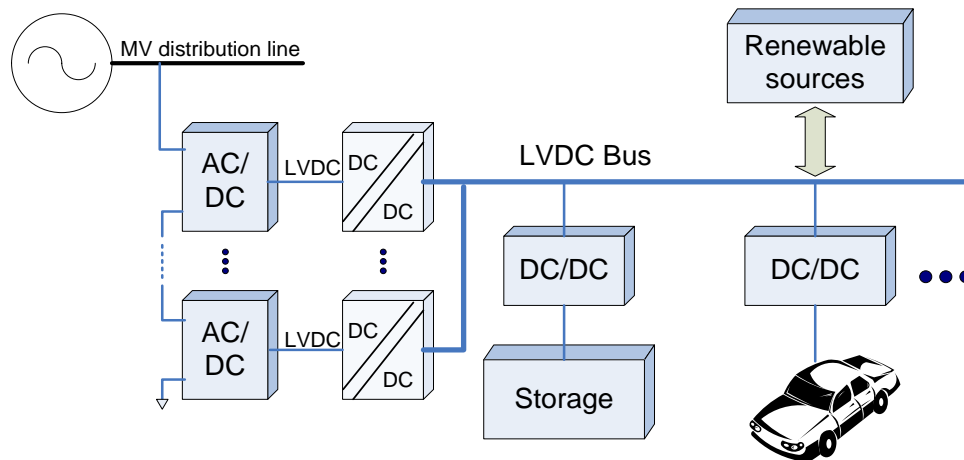
The AC/DC frontend plays an important role as the interface between DC distribution system and the utility. It needs to be reliable, cost effective, and meet the power quality standards such as IEEE 519 [40].

At high power level, the high frequency switching power converters may not be a good choice when considering the cost of high power high frequency switches. Several converters

can be connected in parallel to provide higher power, but this will complicate the system and thus deteriorate system reliability.



(a) Fast charging station architecture with unidirectional AC-DC converter



(b) Fast charging station architecture with bi-directional AC-DC converter [41], [42]

Figure 3.1 fast charging station architecture with different AC/DC frontend

Diode rectifier is the simplest way in practice to convert AC source to DC source. Its high reliability and low cost makes it very competitive in high power applications. Figure 3.1(a) summarizes the approach, with the diode rectifier as the unidirectional AC/DC

frontend. In [41] and [42] authors have proposed to use a cascade of two-stage bi-directional AC/DC converters, that provide isolation with medium frequency DC/DC converters (see Figure 3.1(b)). The same concept was presented in [43], except that the charging station is interfaced with a MVDC distribution system, eliminating the AC/DC stage. In [44], authors present a charging station with the same front end as shown in Figure 3.1(b), but lacking a common DC bus, which rules out the possibility to perform power distribution optimization throughout the system.

Comparing the two architectures, the one shown in Figure 3.1(b) has the ability to feed power back to the grid. However, since the main functionality of the fast charging station is to *charge* the vehicle batteries as quickly as possible, this capability is of little importance. Given that the functionality of the two architectures is the same, the architecture choice will be a function of the designer preference. The design in Figure 3.1(a) uses standardized components which result in low hardware costs, increases system robustness and reduces the construction and maintenance requirements. The design in Figure 3.1(b) may have a higher power density due to the use of medium frequency transformers. An open question is the relative efficiency of the two systems. This question cannot be uniquely answered, as it will be the function of the grid-tie voltage, choice of switching devices, DC bus voltage, and system power ratings. In addition, the system level efficiency numbers are not given in other referenced works ([41]–[43], [45]) limiting the ability to perform a fair comparison. Nevertheless, the switching device power losses for diode rectifier and PWM rectifier (with the same input-output parameters) are calculated and compared at the following section.

A possible disadvantage of using the diode rectifier is the lack of capability to control the rectified DC bus voltage. The DC bus fluctuations due to the grid voltage fluctuations are acceptable in this application since the DC/DC converter (i.e. fast charger) can easily handle a fairly large input voltage fluctuation. Moreover, the voltage fluctuation in this system is expected to be fairly small. According to ANSI C84.1 standard [46], the medium voltage service is in the range of 0.975 to 1.05 p.u. of the rated voltage. Also, according to IEEE Std. 141-1993 [37], the full load voltage drop on a three phase, 1 MVA, 0.95 power factor<sup>1</sup> transformer cannot exceed 2.75%.

The main disadvantage of the diode rectifier is the relatively high harmonic level on both the AC and DC side of the rectifier. One way to reduce harmonics is to increase the pulse number of the diode rectifier. Figure 3.2 gives the typical input current waveform of the 6-pulse, 12-pulse and 18-pulse diode rectifier. The improvement of the power quality by increasing the pulse is significant. However, neither 6-pulse nor the 12-pulse rectifier can meet the IEEE 519 standard requirements [40] without additional filters. By using a dedicatedly designed transformer, the 18-pulse rectifier can have less than 3% total input current distortion [47]. But the structure of this kind of transformer is complicated and thus is difficult to manufacture in practice.

---

<sup>1</sup> The current shaping strategy employed in the method proposed in this chapter results in near-unity power factor.

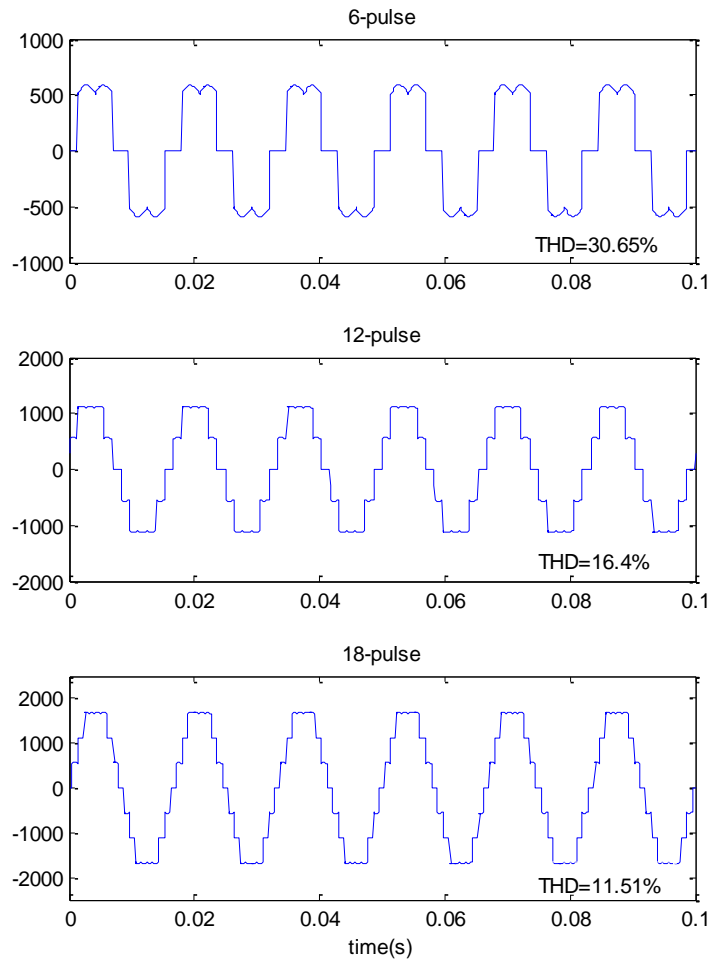
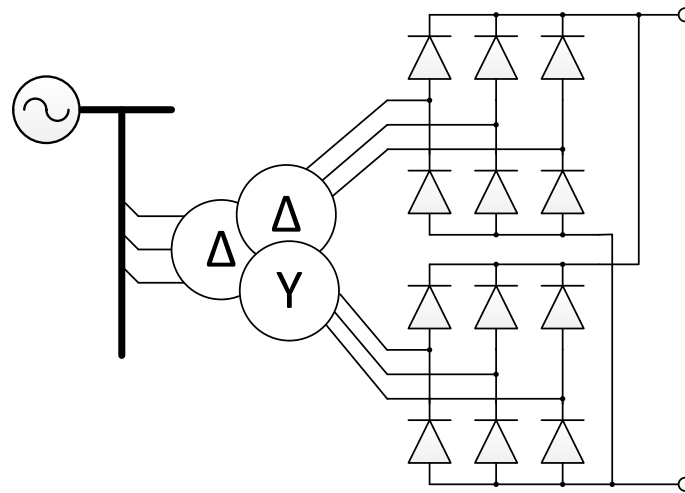
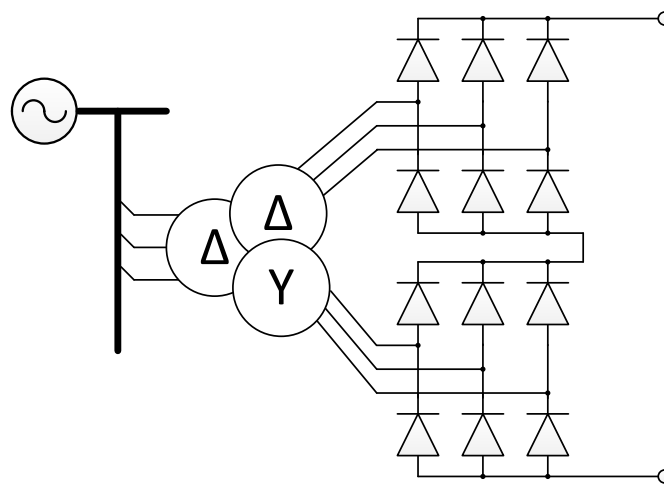


Figure 3.2 Typical input current waveform of 6-pulse, 12-pulse, and 18-pulse diode rectifier

The 12-pulse diode rectifier utilizes commercially available standard delta/ye and delta/delta transformers to achieve harmonic cancellation. And thus is a good tradeoff between harmonic reduction and subsystem complexity. Also, with additional harmonic reduction methods the 12-pulse diode rectifier can have less than 5% of total harmonic distortion (THD) [48]–[54].



(a) Parallel configuration



(b) Series configuration

Figure 3.3 Two types of configuration for 12-pulse diode rectifier

The 12-pulse diode rectifier utilizes two 6-pulse diode rectifiers to achieve harmonic cancellation. There are two ways to configure these two 6-pulse rectifiers, as shown in Figure 3.3. In comparison with the series configuration, the parallel one has lower diode forward voltage drop, and thus is suitable for high current applications. However, proper measures

need to be taken to balance the current between the paralleled rectifiers. The interphase transformer can be used to prevent instantaneous uneven DC voltages from two paralleled rectifiers [47]. But it has no effect on the steady state uneven DC voltage. Considering that the pre-existing voltage distortion in the AC source is the main reason for uneven DC output voltage, the Harmonic Blocking Reactors (HBR) can be used to block the pre-existing harmonics [55]. Note that the interphase transformer is inserted into the DC output and the HBRs are inserted into the AC input lines, which means the entire load current will flow through the interphase transformer and all the input current will flow through the HBRs. Therefore, an increased conduction loss is expected and this may cancel out the advantage of lower diode conduction loss when compared with series configuration.

Table 3.1 Comparison of the Diode Losses for Two Configurations (at 1.1MW)

	Parallel connection	Series connection
Diode type	R9G0121225 (1200A/1200V)	R9G0062215 (2200A/600V)
Diode current (average)	274 A	547 A
Output voltage of each 6-pulse diode rectifier	670 V	335 V
Diode forward voltage drop	1.21V	0.83 V
Conduction loss	3978 W	5448 W
Reverse leakage current	150 mA	150 mA
Reverse leakage loss	603 W	302 W
Total loss	4581 W	5750 W

On the other hand, the series configuration does not have the current sharing problem, and the increase in diode conduction loss may not be so significant. To confirm this, the

diodes for both configurations are selected and their losses are calculated. The AC side voltage is 480 V (RMS) as determined in chapter 2, and thus the rectified DC voltage is 678 V under ideal condition. Considering the voltage drops on the diodes and and/or the filters, the DC side voltage is assumed to be 670 V. This is the output voltage of each 6-pulse diode rectifier for the parallel-connected 12-pulse diode rectifier. For series-connected 12-pulse diode rectifier, each 6-pulse diode rectifier outputs half of that voltage, which is 335V.

Assume that the rectifier output current is purely DC. The output power of the rectifier is 1.1 MW as determined in chapter 2, then the output current is

$$I_{DC} = 1.1MW / 670V = 1642A \quad (3.1)$$

According to the operation of the three phase diode rectifier [56], each diode will conduct the rectifier output current for a period of 1/3 of the line period. For the series-connected 12-pulse diode rectifier, the average current through each diode will be

$$I_{d_s} = I_{DC} / 3 = 547A \quad (3.2)$$

For the parallel-connected 12-pulse diode rectifier, the load current is evenly distributed between the two 6-pulse diode rectifiers. Therefore, the average current through each diode for the parallel-connected 12-pulse diode rectifier is

$$I_{d_p} = I_{DC} / 2 / 3 = 274A \quad (3.3)$$

With the voltage-current configurations of the two setups, the appropriate diodes are chosen as given in Table 3.1. The dominant power losses on the diodes are the conduction losses. With the diode average conducting current known and diode forward voltage drop being given in the datasheet, the conduction losses can be easily calculated, as shown in Table 3.1. The maximum leakage current is used to calculate the reverse leakage loss, as

given in Table 3.1. The reverse recovery time is very small for these two diodes ( $25\mu\text{s}$  for R9G0121225 and  $15\mu\text{s}$  for R9G0062215), so the losses caused by reverse recovery are neglected here. As a result, the total losses for these two connections are given in Table 3.1 and the total loss difference is 1169 W. For a 1.1 MW system, this will cause a decrease of the efficiency by less than 0.11%. This is acceptable when considering the simplicity of the series configuration, not to mention that the interphase transformer and HBRs for the parallel configuration will also bring additional losses. Therefore, for reasons of simplicity, the series configuration of the 12-pulse diode rectifier is preferred.

## **3.2 Efficiency Comparison between Proposed 12-pulse Diode Rectifier and PWM Rectifier**

As discussed in the beginning of section 3.1, the high frequency switching power converters are not good options mainly because of the high cost and the complexity of the control. Nevertheless, the efficiency comparison of the proposed 12-pulse diode rectifier and high frequency switching power converters is of great interest. While it is difficult to compare the overall efficiency of the whole system for these two options, it is straightforward to calculate the power losses of the switches. The power losses of the diodes for the proposed 12-pulse diode rectifier are already given in Table 3.1. For the high frequency switching power converters, the PWM rectifier is chosen as an example. The power loss can be easily calculated by using the Power Module Loss Simulator (named “Melcosim”) provided by Mitsubishi. Figure 3.4 gives the calculated results of the power

loss of the 1.1 MW PWM rectifier. The power loss of one leg is shown. The other two legs have the same power loss. The AC side current is determined as

$$I_{ac\_rms} = 1.1MW / 480V / \sqrt{3} = 1299A \quad (3.4)$$

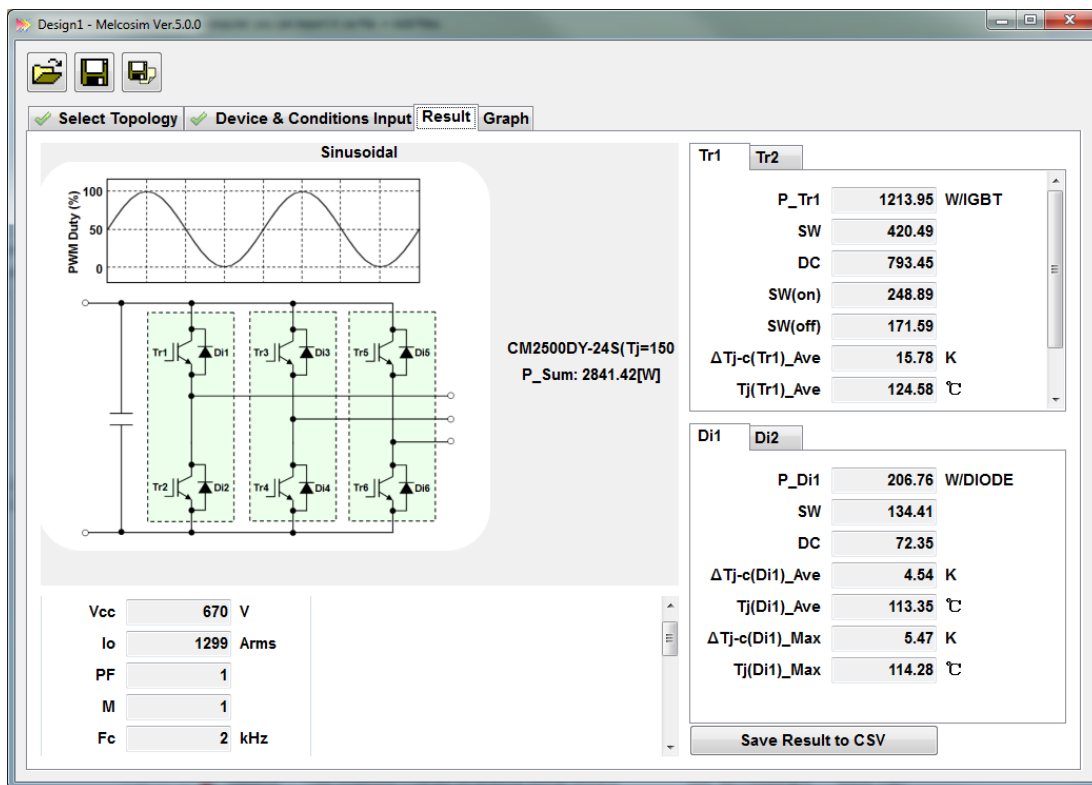


Figure 3.4 Power loss calculation results of one leg of the 1.1 MW PWM rectifier

The IGBT module used here is CM2500DY-24S (2500A/1200V dual IGBT) which is the only module from Mitsubishi that satisfies the voltage and current requirements of this application. The switching frequency is 2 kHz which is the suggested value for this IGBT module. Gate resistance is set to 0 Ω as suggested by the datasheet. In practice, a higher gate

resistance may be needed to slow down the switching speed and reduce EMI, which will result in higher switching loss.

The comparison between the proposed diode rectifier and the PWM rectifier in terms of power loss and device cost is given in Table 3.2. It is clear that the proposed 12-pulse diode rectifier has substantially lower power loss and device cost. Not to mention that the PWM rectifier also needs gate drivers and controller, which will result in additional costs.

Table 3.2 Comparison of the proposed diode rectifier and PWM rectifier

	PWM rectifier	Proposed diode rectifier
Conduction loss of one IGBT	793.45 W	n.a.
Conduction loss of one diode	72.35 W	454 W
Total conduction loss	5195 W	5448 W
Switching loss of one IGBT	420.49 W	n.a.
Switching loss of one diode	134.41 W	neglected
Total switching loss	3329.4 W	neglected
Total reverse leakage loss	neglected	302 W
Total power loss	8524 W	5750 W
Unit price of the module/diode	\$1871.56	\$178.45
Total cost of the switches	\$5614.68	\$2141.4

The next question is how to control the harmonic level of the 12-pulse diode rectifier, which will be the focus of the following sections.

### **3.3 Traditional Approach to Integrate Energy Storage and Eliminate AC Side Harmonics**

A standard way to eliminate AC side harmonics is to use active, passive or hybrid power filters [57]–[59]. Though these methods are well understood and widely used, a drawback is that passive filters are bulky, while active filters require complex control and specialized power electronics.

The integration of energy storage is straightforward and can be achieved by connecting the energy storage in parallel with DC distribution bus. A power conversion system is usually needed as the interface between energy storage and DC distribution system, but it could be absent in certain applications.

Traditionally, the energy storage integration and AC side harmonics elimination are two independent functions. If the system needs both functions, the energy storage system and the harmonics elimination filters will be designed separately. The harmonics elimination filters are usually connected to the AC side, while the energy storage could be on the DC ([28] and [29]) or AC side ([19]). Note that in [19], a STATCOM is used on the AC side, instead of harmonic filters. The simplified and generalized diagrams of these two systems are given in Figure 3.5 and Figure 3.6. The dashed line indicates alternative connecting point for the filters/compensators (which could be passive, active or hybrid filters, STATCOM, etc.).

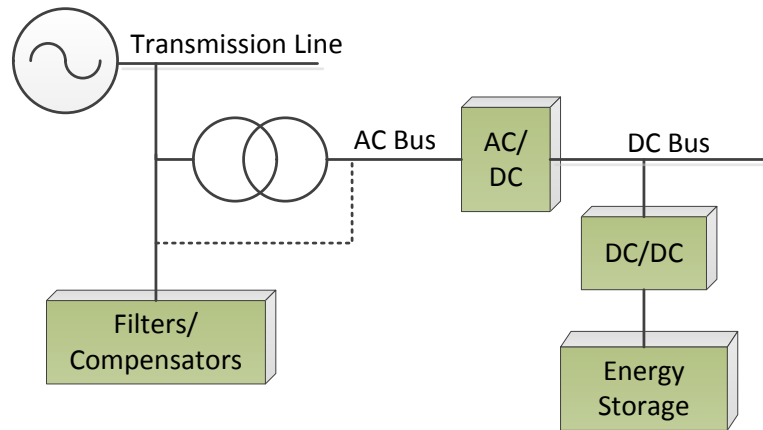


Figure 3.5 Distribution system with DC side energy storage integration and AC side filters/compensators

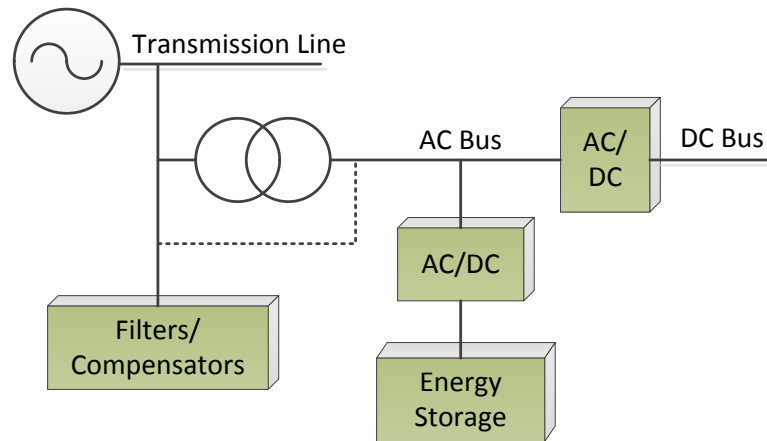


Figure 3.6 Distribution system with AC side energy storage integration and AC side filters/compensators

While the aforementioned approach is straightforward, it neglects the possibility that the active filters/compensators could also be used to integrate energy storage, and thus simplify the system and cut hardware costs. In [7], [21]–[23], [30] authors present AC side active

compensators (APF or STATCOM) with energy storage integrations. The generalized system diagram is shown in Figure 3.7. This approach is good for AC distribution systems. However, for DC distribution system, it is not efficient to integrate the DC energy storage in the AC side. The main disadvantage is that integrating the energy storage on the AC side requires the power delivered from the energy storage system to go through two conversion stages when power is delivered from the energy storage system to the DC load. In addition, the integration of the storage on the DC side can allow for a limited integration of renewables on the DC side without the need for bi-directional AC/DC stage. Moreover, the control of such system is complicated.

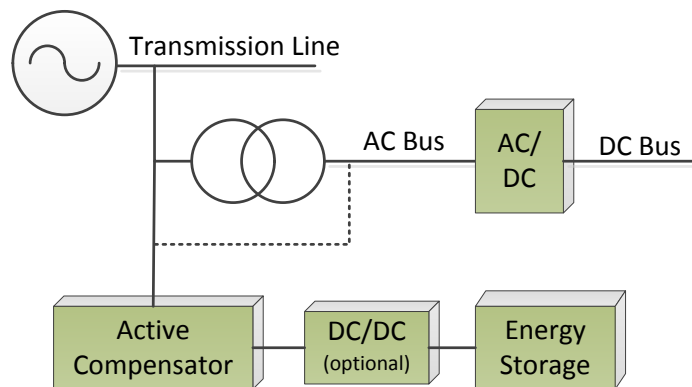


Figure 3.7 Distribution system with AC side active compensator and energy storage integration

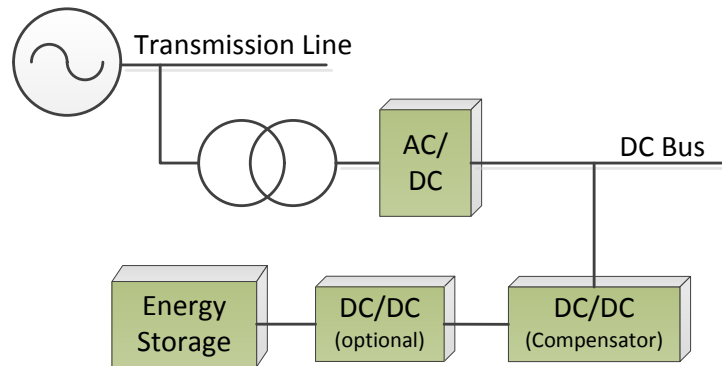


Figure 3.8 Proposed DC distribution system with energy storage integration and harmonic elimination

In this chapter, a new approach is proposed, to integrate energy storage and eliminate AC side harmonics, as depicted in Figure 3.8. The novelty is that the same DC/DC converter/compensator is used to integrate the energy storage, eliminate DC side ripple, and eliminate AC side harmonics. While the first two functions are considered the state of the art, the challenge is to use DC side compensator to eliminate AC side harmonics. This approach will be presented in the following sections.

### 3.4 AC Harmonics Elimination by Profiling DC Rectifier

#### Current for the 12-Pulse Rectifier

In analyzing the operation of 12-pulse rectifier (Figure 3.9), some methods are dedicatedly designed to shape the output current of 12-pulse rectifier ( $i_{rec1}$ ,  $i_{rec2}$ ) so as to minimize AC side harmonics ( $i_a$ ,  $i_b$ ,  $i_c$ ) formed by the operation of the rectifier. The exact shape of the rectifier output current that results in complete elimination of AC input current harmonics has been derived in [48], [49]. Authors in [48]–[52] show that the triangular

waveform, shown in Figure 3.10, presents a good approximation of the ideal rectifier output current that completely eliminates the AC current harmonics. Detailed analysis of this approach is given in the following sections and existing harmonic eliminating methods are reviewed.

### 3.4.1 Analysis of the Principle for AC Harmonics Elimination by Profiling DC

#### Rectifier Current

Assuming that the rectifier current is profiled to be triangular, its Fourier series expansion gives:

$$\begin{aligned}
 i_{rec1} &= I_L + 4I_L \cdot \sum_{n=1}^{\infty} \frac{1 - (-1)^n}{n^2 \pi^2} \cdot \cos\left(6\left(n\omega t + \frac{\pi}{6}\right)\right) \\
 i_{rec2} &= I_L + 4I_L \cdot \sum_{n=1}^{\infty} \frac{1 - (-1)^n}{n^2 \pi^2} \cdot \cos(6n\omega t)
 \end{aligned} \tag{4.1}$$

where  $\omega$  is the line frequency and  $I_L$  is the load current delivered to the DC load, and  $i_{rec1}$  and  $i_{rec2}$  are defined in Figure 3.9.

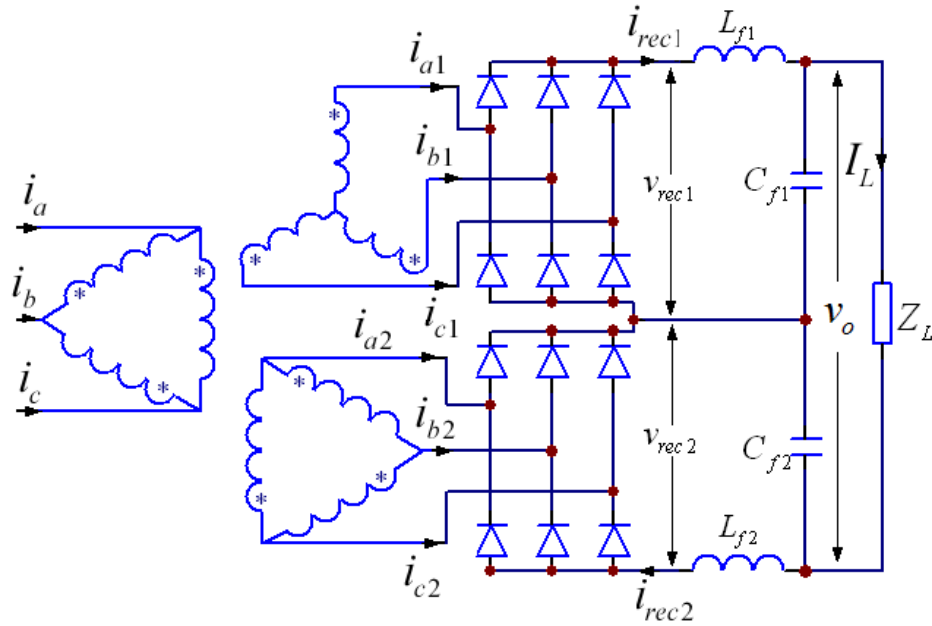


Figure 3.9 The 12-pulse diode rectifier

Following the diagrams in Figure 3.10, the line current can be expressed as a function of  $i_{rec1}$  and  $i_{rec2}$ .

$$\begin{aligned}
 i_{a1} &= \frac{\sqrt{3}I_a}{4I_L} \cdot i_{rec1} \cdot S \angle 30^\circ \\
 i_{c1} &= \frac{\sqrt{3}I_a}{4I_L} \cdot i_{rec1} \cdot S \angle 150^\circ \\
 i_{a2} &= \frac{\sqrt{3}I_a}{4I_L} \cdot i_{rec2} \cdot S \angle 0^\circ
 \end{aligned} \tag{4.2}$$

where  $S$  is defined as:

$$S = \frac{2\sqrt{3}}{\pi} \left( \sin(\omega t) - \frac{1}{5} \sin(5\omega t) - \frac{1}{7} \sin(7\omega t) + \frac{1}{11} \sin(11\omega t) + \frac{1}{13} \sin(13\omega t) \dots \right) \tag{4.3}$$

which is the switching function shown in Figure 3.10.

The AC side phase A current  $i_a$  can be expressed as:

$$i_a = (i_{a1} - i_{c1})/\sqrt{3} + i_{a2} \quad (4.4)$$

By numerically evaluating (4.1)~(4.4), the AC side line current THD is shown to be close to 1% [48], [49].

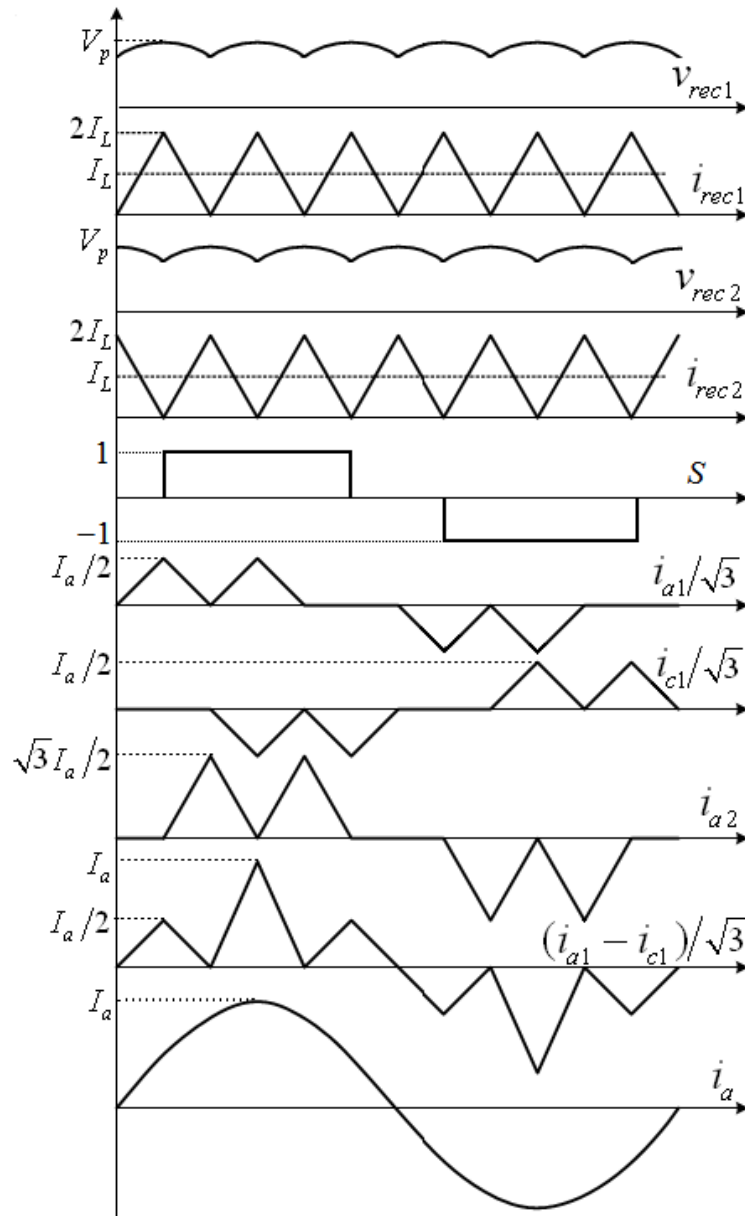


Figure 3.10 Construction of the AC input current for direct current shaping approach

Based on the operation of the 6-pulse rectifier, the Fourier series expansion of rectifier output voltage is:

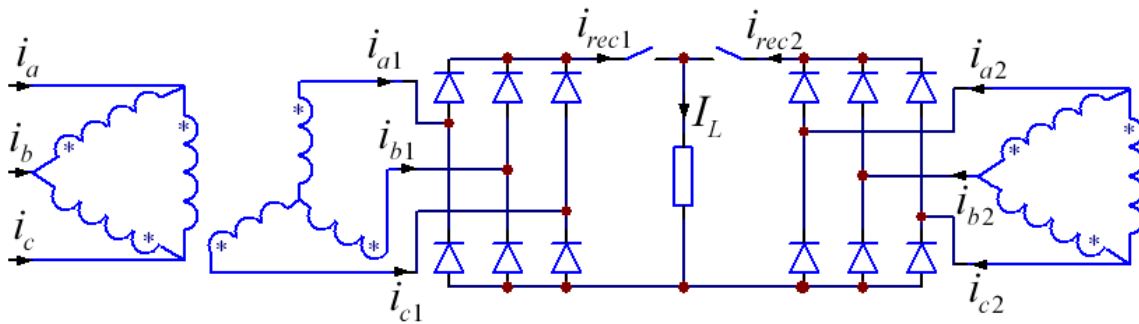
$$\begin{aligned}
 v_{rec1} &= v_{rec1\_dc} + v_{rec1\_ac} = \frac{3 \cdot V_p}{\pi} + \frac{6 \cdot V_p}{\pi} \cdot \sum_{n=1}^{\infty} \frac{-(-1)^n}{36n^2 - 1} \cdot \cos\left(6\left(n\omega t + \frac{\pi}{6}\right)\right) \\
 v_{rec2} &= v_{rec2\_dc} + v_{rec2\_ac} = \frac{3 \cdot V_p}{\pi} + \frac{6 \cdot V_p}{\pi} \cdot \sum_{n=1}^{\infty} \frac{-(-1)^n}{36n^2 - 1} \cdot \cos(6n\omega t)
 \end{aligned} \tag{4.5}$$

where  $V_p$  is the peak value of the AC input voltage and  $v_{rec1}$  and  $v_{rec2}$  are defined in Figure 3.9 as the rectified voltages.

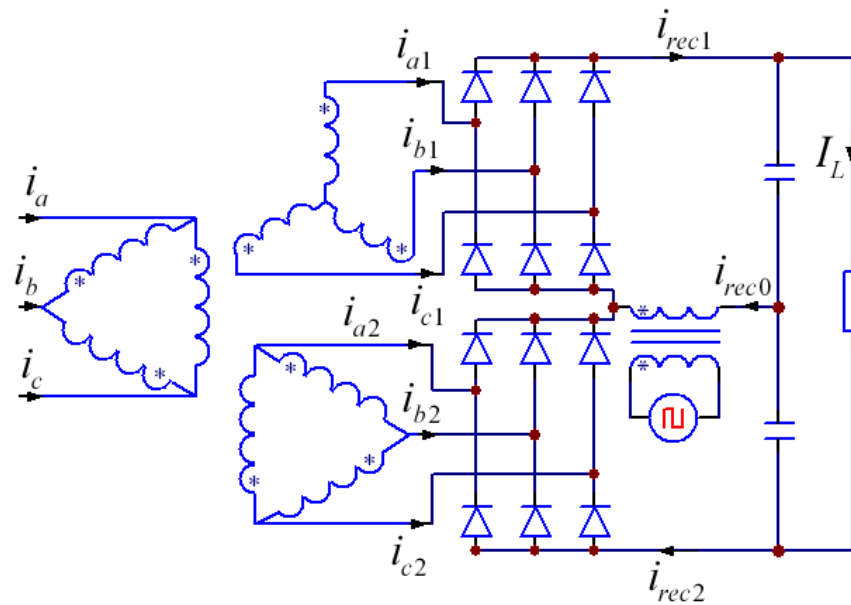
Analyzing (4.1) and (4.5), both  $v_{rec}$  and  $i_{rec}$  have a strong AC component at six times the source frequency. The fundamental AC components of the voltage and the current are in phase for each 6-pulse rectifier, while these AC components are out of phase when comparing the upper and lower rectifiers, as evident from Figure 3.10 and (4.1) and (4.5). The fact that the fundamental AC components of the voltage and the current are in phase for each 6-pulse rectifier is exploited in the LC filter design as discussed in later sections.

### 3.4.2 Existing Methods

Numerous topologies have been proposed to shape the rectifier output current in order to eliminate the AC harmonics. They generally rely on directly shaping the rectifier current [52] or on inserting a voltage source between the capacitor bank and the rectifier [48]–[51]. In [52] the authors propose to directly shape the rectifier output current by the use of active switches to directly control the rectifier output current (see Figure 3.11a). Since the entire rectifier output current has to be processed by the active switches, this method is not very efficient.



(a) Direct shaping the rectifier current [52]



(b) Insertion of a voltage source between the capacitor bank and the rectifier [48]–[51]

Figure 3.11 Existing methods for shaping the rectifier current

Other approaches [48]–[51] insert a voltage source into the rectifier output loop as shown in Figure 3.11b. The voltage source generates a rectangular pulse voltage with proper amplitude and a frequency of 6 times of line frequency, resulting in triangular rectifier output current. Researchers present a rough implementation of this idea in [50] by using the tap-changer, while [48] uses a 5-level fixed-amplitude voltage source. The control accuracy of

these setups is limited. In [49], [51] authors shape the rectifier output current by using PWM controlled active converter to control the inserted voltage source.

The problem with the approaches in [48]–[51] is that they require continuous rectifier output current to function. In addition, the rectifier output voltage needs to be constant (no ripple) to have expected results. This requires a large filter capacitor. Moreover, the current through the 360 Hz transformer (for 60 Hz grid), has an amplitude of  $\pm 2I_L$  resulting in a large conduction loss. The noise generated by the low frequency transformer poses another problem.

### **3.5 Direct Current Shaping Approach to Integrate Energy**

#### **Storage and Achieve AC Side Harmonics Elimination**

To solve the aforementioned problems with existing methods, a new approach is proposed in this section. This approach relies on parallel connected current sources to directly shape the rectifier output current. The energy storage integration is also straightforward with the parallel connection. Detailed analysis will be given in the following sections. Simulation and experiment results are also given to verify the performance of proposed method.

##### **3.5.1 Proposed Direct Current Shaping Approach**

A novel approach proposed in this dissertation inserts three current sources into the circuit as shown in Figure 3.12. The two current sources ( $i_{s1}$  and  $i_{s2}$ ) in parallel with each 6-pulse rectifier are used to shape the rectifier currents  $i_{rec1}$  and  $i_{rec2}$  in order to eliminate the AC side harmonics. The third current source  $i_{s3}$  is used to inject active power from an energy

storage system. In addition to providing the ability to inject real power on the DC side, it is also shown that with the correct choice of the LC filter parameters, the VA rating of the current source used for filtering can be substantially reduced. A direct comparison with other proposed solutions is more difficult, since the VA ratings of the voltage source will be a function of the design of the entire system.

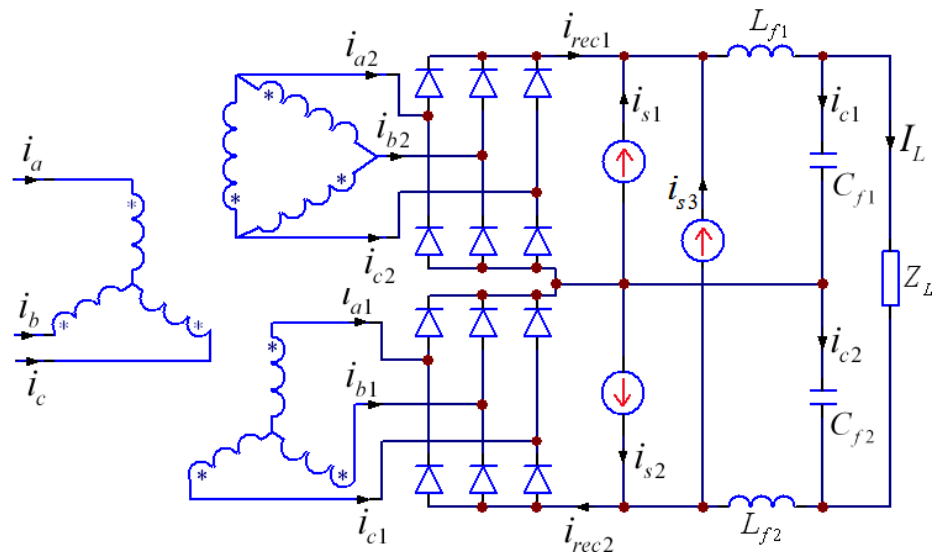


Figure 3.12 Proposed method with parallel connected current sources



(1) The parallel connected current sources can be used to interface energy storage system to inject active power;

(2) Additional 360 Hz transformer presented in approaches outlined in [48]–[51] is eliminated;

(3) The proposed method works even if the initial rectifier current is discontinuous;

Since the current sources only need to compensate the current difference, the VA rating of the current sources will be comparable to (or less than) those in [48]–[51].

### 3.5.2 System Analysis and Parameter Optimization

To improve the efficiency of the proposed approach, the VA rating of these current sources can be minimized through appropriate choice of filtering components.

For sake of simplicity, from now on the numbering of subscripts will be omitted (e.g.  $i_{rec}$  instead of  $i_{rec1}$  and  $i_{rec2}$ ) since the analysis can be generalized for either 6-pulse rectifier.

The equivalent circuit of the 12-pulse rectifier is shown in Figure 3.14. Considering the DC and fundamental component, each six-pulse rectifier can be represented by a DC and AC source in series ( $v_{rec\_ac}$  and  $v_{rec\_dc}$ ). Looking at the equivalent circuit of the system, the two DC voltage sources are connected in series, and will produce a DC current in the load which is also the DC component of  $i_{rec}$ . The DC load current can be calculated as:

$$I_L = \frac{v_{rec1\_dc} + v_{rec2\_dc}}{R_L} = \frac{6}{\pi} \cdot \frac{V_p}{R_L} \quad (4.6)$$

where  $v_{rec1\_dc}$  and  $v_{rec2\_dc}$  are given in (4.5).

To attenuate the effect of  $v_{rec\_ac}$  on the DC load, an LC filter is inserted between the rectifier and the load. The inductor is formed by the leakage inductance of the transformer  $L_{leak}$ , and additional inductor  $L_f$  on the DC side.

In this investigations, rather than using the LC filter to attenuate the effect of  $v_{rec\_ac}$  on the load, the LC filter is used to shape the rectifier output current,  $i_{rec}$ , to be as close as possible to the desired shape  $i_{rec\_ref}$ , as illustrated in Figure 3.15. As described by (4.1) and (4.5) the fundamental component of  $v_{rec\_ac}$  is dominant, and it is in phase with the fundamental component of the triangular current reference  $i_{rec\_ref}$ , as given in (4.1). The THD of  $i_{rec\_ref}$  can be calculated based on (1), as 12.12%, which suggests that the fundamental component of  $i_{rec\_ref}$  is also dominant.

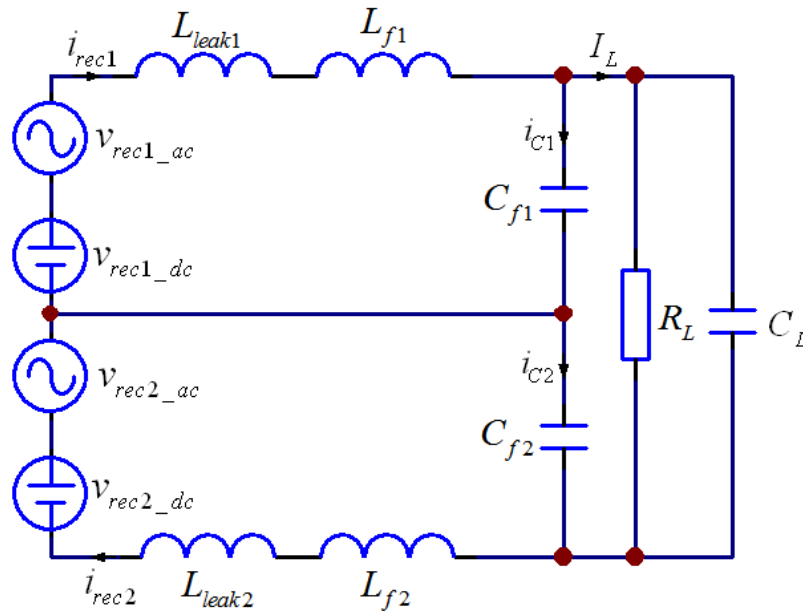


Figure 3.14 Equivalent circuit of the 12-pulse rectifier

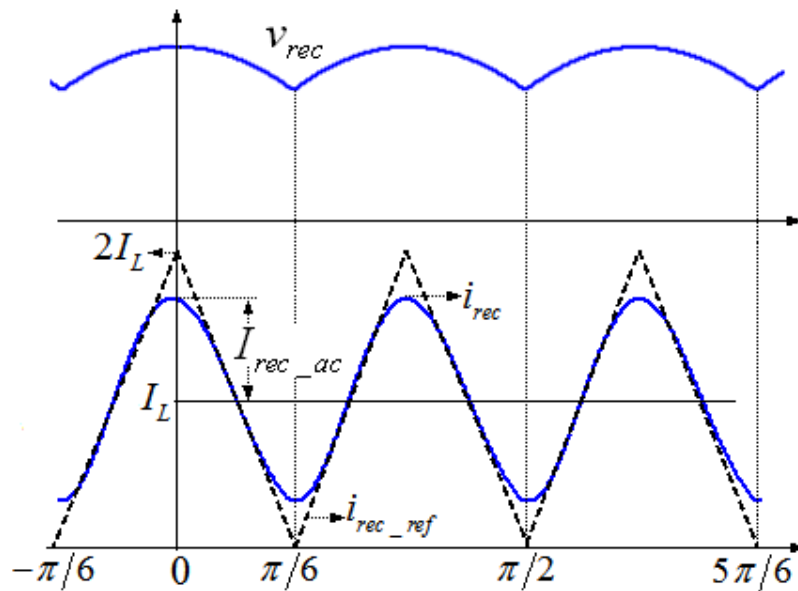


Figure 3.15 Rectifier output voltage and current

To ensure that  $v_{rec1}$  and  $i_{rec1}$  remain in phase, the LC filter should be purely resistive (i.e. at resonance) at the frequency of interest, namely  $6\omega$ . Using the superposition principle, and assuming resonance in the two LC filters at  $6\omega$  results in a current flow only in the respective LC filter. This is the result of the infinite impedance presented by the parallel resonance in the other branch, as depicted graphically in Figure 3.16<sup>2</sup> for  $v_{rec1\_ac}$ ; the analysis is similar for  $v_{rec2\_ac}$ . Therefore, the AC component of  $i_{rec}$  will only be determined by  $v_{rec\_ac}$  and the equivalent series resistance (ESR) of the LC filter (which is not shown in the figure). By only considering the fundamental component of  $v_{rec\_ac}$  and  $i_{rec}$ , and assuming  $i_{rec}$  is continuous, the peak value of the AC component of  $i_{rec}$  can be calculated:

<sup>2</sup> In reality, the impedance of the LC circuit is determined by the ESR of the LC, and the resistance of the load. In practice the resulting current through the branch is negligible.

$$I_{rec\_ac, peak} = \frac{6}{35\pi} \cdot \frac{V_p}{ESR_{LC}} \quad (4.7)$$

where  $ESR_{LC}$  is the total ESR of the LC filter.

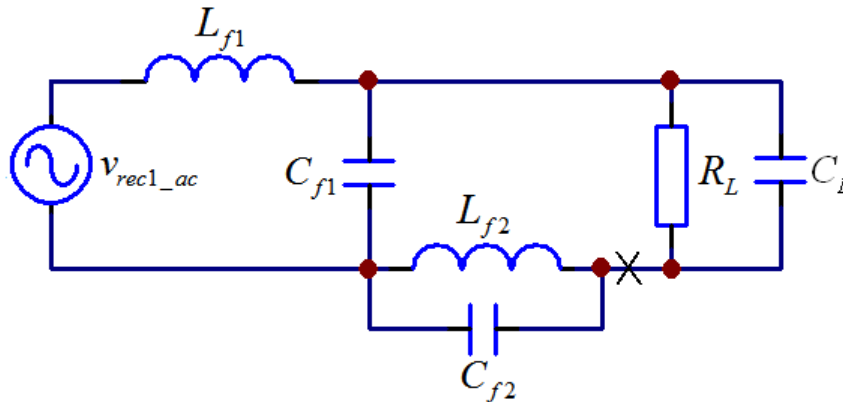


Figure 3.16 Decoupling of the currents produced by the fundamental of

The optimal value of  $ESR_{LC}$  will depend on the load current, and the ESR can only be optimized for one value of load. To derive the optimal ratio between  $ESR_{LC}$  and  $R_L$  the parameter  $m$  is defined as:

$$m = \frac{I_{rec\_ac, peak}}{I_L} \quad (4.8)$$

Solving numerically for a value of  $m$  that gives the minimum difference between the fundamental component of  $i_{rec\_ac}$  and the triangular reference  $i_{rec\_ref}$ , there is:

$$m = 0.77 \quad (4.9)$$

The rectifier output current and triangular reference are shown in Figure 3.15 for  $m=0.77$ . It is apparent that the two waveforms are quite close. Combining (4.6), (4.7), and (4.8) results in:

$$\frac{ESR_{LC}}{R_L} = \frac{1}{35m} \quad (4.10)$$

Based on (4.9) and (4.10) the optimized ESR can be chosen for a certain load resistance.

### 3.5.3 Injected Current Flow

Next, using the superposition principle, the current flow from the inserted current source is analyzed. Based on the equivalent circuit as given in Figure 3.17, three paths are possible. Ideally, the current should flow primarily through path I. Assuming the worst case where the initial rectifier output current is purely DC, the current source will need to inject:

$$i_s = 4I_L \cdot \sum_{n=1}^{\infty} \frac{1 - (-1)^n}{n^2 \pi^2} \cdot \cos(6n\omega t) \quad (4.11)$$

Therefore, the fundamental of the current source will be at 360Hz. It is apparent that if  $L_f$  is larger than  $L_{leak}$  the higher order harmonics will take the desired path. At 360Hz, when  $L_f$  and  $C_f$  are in resonance at 360 Hz, only paths I and II are possible, as shown earlier. To ensure the current takes the desired path, it is preferable to minimize the transformer leakage inductance and ESR (which is not shown in Figure 3.17) so that most of the current takes Path I.

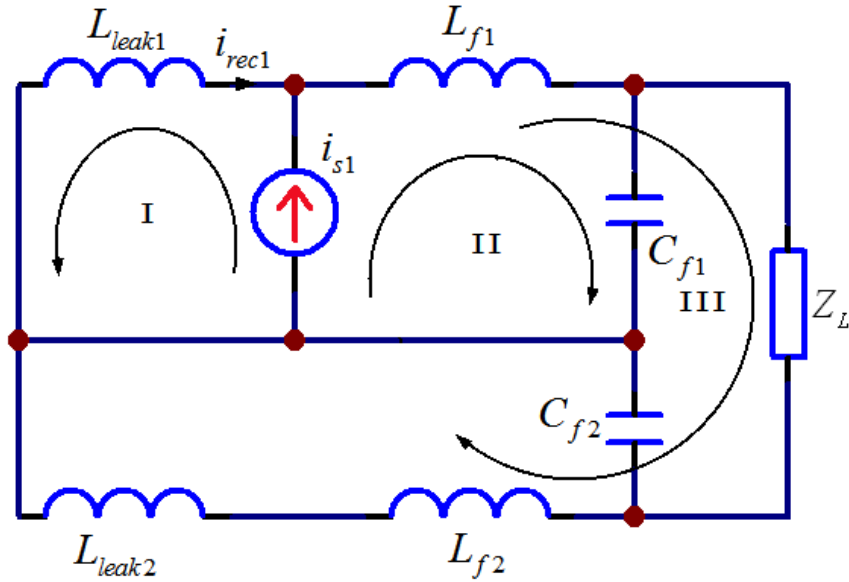


Figure 3.17 Equivalent circuit for the upper current source using the superposition principle

### 3.5.4 Control Strategy

According to previous analysis of the proposed approach, the system operates as a controlled current source that is controlled by the difference of the desired and actual rectifier output current ( $i_{rec\_ref}$  and  $i_{rec}$ ). Proportional control is applied, similar to the approach adopted by DC or AC active power filters. The equivalent circuit of the proposed system is given in Figure 3.18.

Let:

$$i_{s1\_ref} = k \cdot (i_{rec1} - i_{rec1\_ref}); \quad i_{s2\_ref} = k \cdot (i_{rec2\_ref} - i_{rec2}) \quad (4.12)$$

where  $k$  is the proportional gain of the controlled current source. By analyzing this topology, there is:

$$i_{rec1} = i_{L1} - i_{s1}; \quad i_{rec2} = i_{L2} + i_{s2} \quad (4.13)$$

Assuming that the current source is ideal, meaning it can output the commanded current:

$$i_{s1} = i_{s1\_ref}; \quad i_{s2} = i_{s2\_ref} \quad (4.14)$$

Combining (4.12) , (4.13) and (4.14):

$$i_{rec1} = \frac{ki_{rec1\_ref} + i_{L1}}{k+1}; \quad i_{rec2} = \frac{ki_{rec2\_ref} + i_{L2}}{k+1} \quad (4.15)$$

From (4.15) it can be seen that the performance of the current source is determined by the proportional gain  $k$ . When  $k$  is infinite  $i_{rec1}=i_{rec1\_ref}$  and  $i_{rec2}=i_{rec2\_ref}$ .

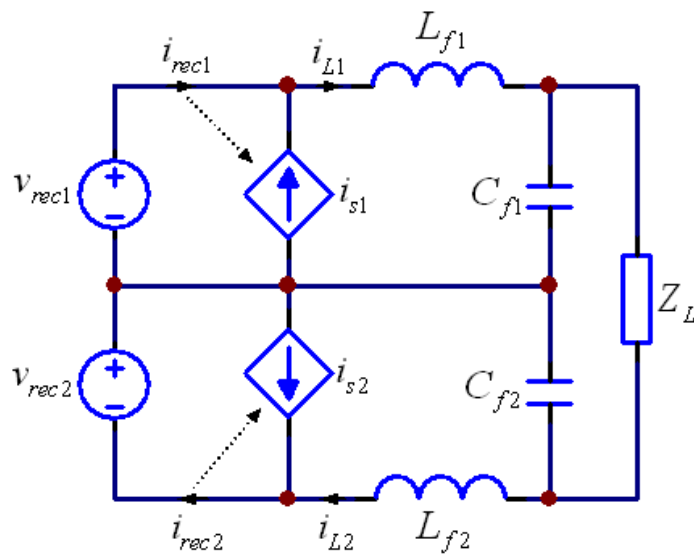


Figure 3.18 Equivalent circuit of the 12-pulse rectifier with the current sources included

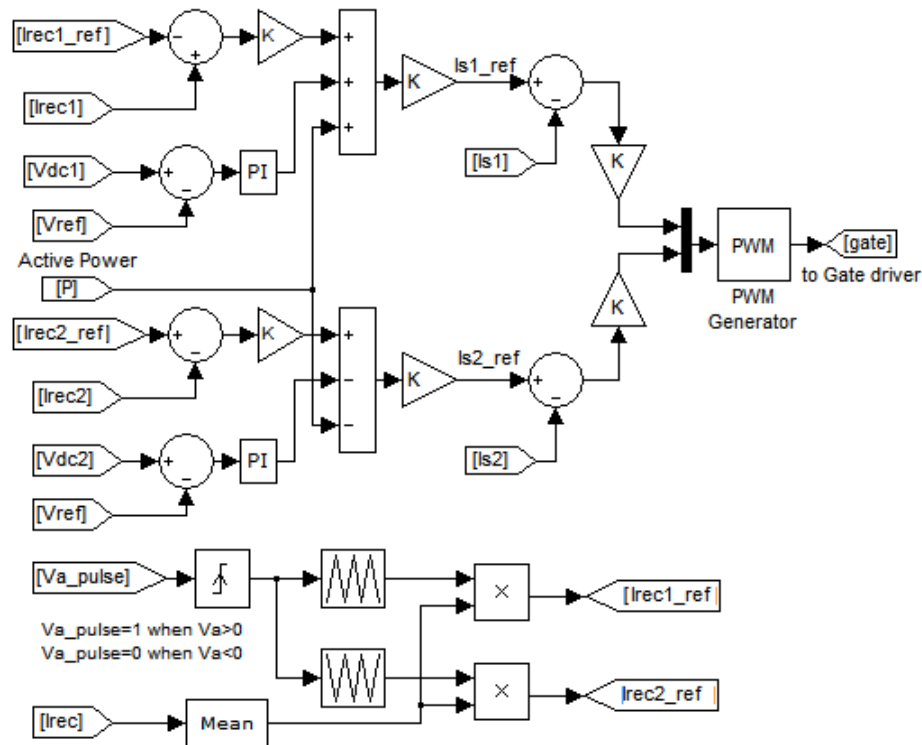


Figure 3.19 Control diagram of direct current shaping approach

The control diagram of the system is given in Figure 3.19. There are two control loops. The inner loop controls the current source output current  $i_{s1}$  and  $i_{s2}$ . The outer loop controls the rectifier output current  $i_{rec1}$  and  $i_{rec2}$ . The reference for  $i_{s1}$  and  $i_{s2}$  consists of three parts. The first part serves to compensate current  $i_{rec1}$  and  $i_{rec2}$ . It is the difference between the actual and desired rectifier output current. The desired rectifier output currents,  $i_{rec1\_ref}$  and  $i_{rec2\_ref}$ , are generated by multiplying the averaged rectifier output current ( $i_{rec1}$  and  $i_{rec2}$ ) and the triangular reference which is synchronized with the line voltage. The dynamics of the averaging can be fairly slow, since the result of a mismatch between the estimated and actual value of  $I_L$  simply results in real power injection/absorption by current source into/from the

load during the transient. The second part serves to maintain a constant and balanced voltage at the DC links of the two Buck-Boost converters. The voltages of the upper and lower capacitor ( $C_{DC1}$  and  $C_{DC2}$  as in Figure 3.13) are  $V_{dc1}$  and  $V_{dc2}$ , respectively. Since the capacitor voltage is DC signal with fairly large time constant, a proportional-integral (PI) control is used to ensure zero steady state error. The third part serves to inject active power to the load. Overall, the control is much simpler than that of the AC side active power filters [60], [61].

### 3.5.5 Simulation and Experimental Results

Two systems are studied in this investigation: a large industrial 1 MVA system is analyzed through simulations, and a smaller setup is built to validate the proposed concept. The main limitation of the experimental setup is the high leakage inductance and the high ESR of the transformer. However, the setup was successfully utilized to validate the system functionality. Specifically, the harmonic reduction and active power injection are validated experimentally, while the VA rating of the current sources, which is significantly affected by the component parameters (ESR, leakage inductance, etc.), was studied through simulations.

#### 3.5.5.1 Simulation Results

A 1 MVA AC/DC rectifier is simulated using SimPowerSystems Toolbox in Simulink. The specifications of the setup are given in Table 3.3. The LC filter ESR is optimized according to (4.10) to give the minimum current source VA rating at  $R_L = 0.5\Omega$  (where  $R_L = 0.37\Omega$  is the full load resistance). The 12-pulse diode rectifier is simulated to get the rectifier

output current  $i_{rec1}$  and  $i_{rec2}$ . The required current source output is then calculated by subtracting the rectifier output current from the reference  $i_{rec1\_ref}$  and  $i_{rec2\_ref}$ .

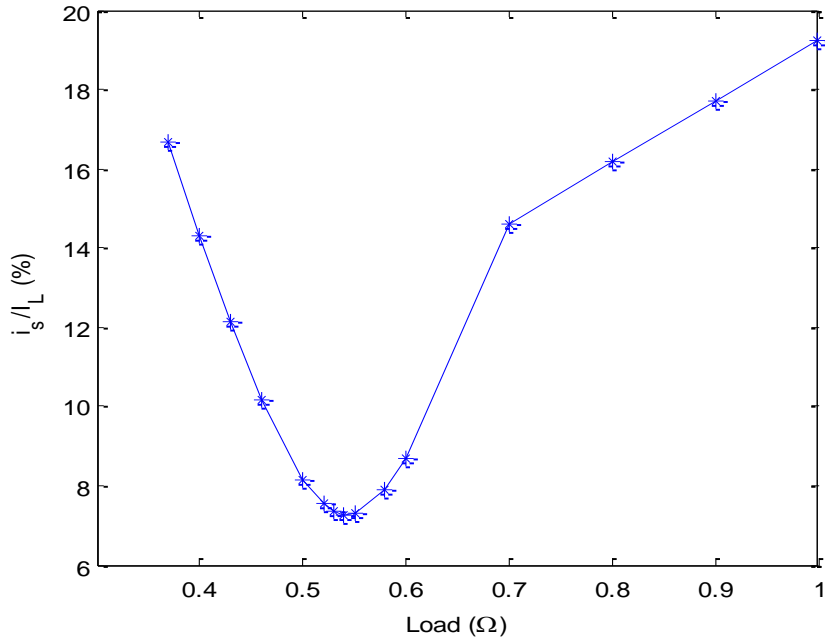


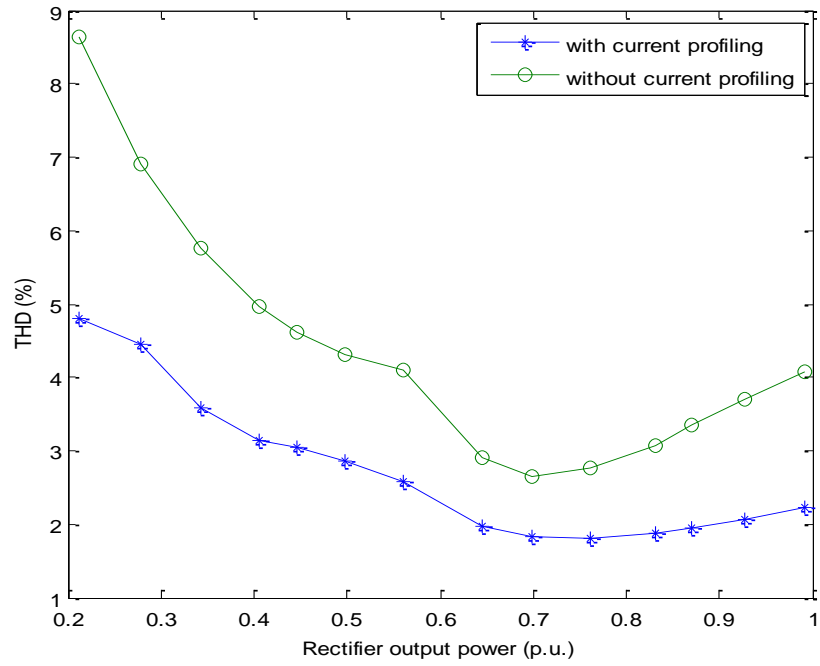
Figure 3.20 Verification of optimized ESR

Simulation results summarized in Figure 3.20 show that the RMS current of current source normalized by the load current reaches a minimum at  $R_L = 0.54\Omega$  which is close to the designed value of  $R_L = 0.5\Omega$ . The simulations show that the current required in shaping the rectifier into triangle as a proportion of the load current reaches its minimum close to the value derived in section 3.5.2. The small difference comes from the omission of higher order harmonics in the original analysis, and neglected cross-coupling between LC filters due to non-infinite impedance of the LC resonant circuit. At the point when the load resistance is

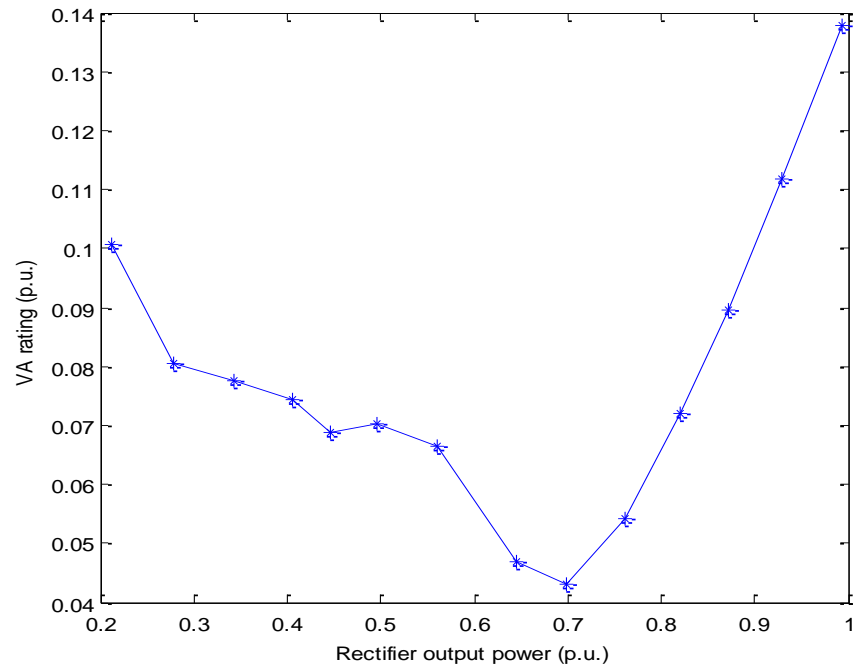
0.7 $\Omega$ , there is a mode change of the rectifier output current, from continuous to discontinuous. When the rectifier output current is discontinuous the ratio of injected current  $i_s$  and load current  $i_L$  tends to be linear. It is difficult and not necessary to analytically derive this linearity, though.

Table 3.3 Parameters of the AC/DC Rectifier for Simulations

Parameter	Value
Output power	1 MW
Transformer primary voltage (line to line RMS)	4160 V
Transformer secondary voltage (line to line RMS)	240 V (two in series)
Transformer leakage inductance (equivalent)	5 $\mu$ H (0.82% p.u.)
DC side inductor	44.3 $\mu$ H
ESR of $L_f$ and $C_f$	10m $\Omega$ /8.6m $\Omega$
Rectifier output capacitor ( $C_{f1}, C_{f2}$ )	3.6 mF
Buck-Boost switching frequency	20 kHz
Buck-Boost DC link voltage	600 V
Buck-Boost output filtering inductor	100 $\mu$ H



(a) THD of line current



(b) Combined VA rating of the current sources

Figure 3.21 Simulation results with switching model of proposed system

It is of note that since the compensation current  $i_s$  is calculated as the difference between the rectifier output current and the reference, it is assumed that all of the current generated by the current source flows through the rectifier. In practice, some current will flow through the LC branch, as described in section 3.5.3. In addition, in a practical implementation due to the actuation limitations of the current source hardware (mainly defined by the inductor size and voltage source magnitude), the rectifier output current cannot be completely compensated. This results in (slightly) higher THD and a lower VA rating of the current source. To prove this point, a switching model is built and simulations are performed at different load conditions. The results are given in Figure 3.21. The VA rating remains low, especially at optimized point. The system can be optimized at different load conditions depending on application requirements. Note that in all cases, the THD is below 5%. It is also worth noting here that the rectifier current becomes discontinuous at 0.56 (p.u.), yet the filter is still able to control the harmonics all the way down to 0.2 (p.u.). This is one of the benefits of the proposed approach compared to other approaches that shape the 12-pulse rectifier output current. Additionally, the LC filter VA rating is kept quite low.

### 3.5.5.2 Experiment Results

A small scale experiment setup is built to verify the functionality of the proposed system. The specifications of this setup are given in Table 3.4. A picture of this setup is shown in Figure 3.22. The 3-phase transformer consists of three single phase transformers (VPT48-10400) and the secondary windings are rewound to get desired voltage level. The 12-pulse diode rectifier consists of two 3-phase diode bridges (SC50VB80). Two inductors are connected in series to get  $L_f$ . The filter inductors were hand-wound around a ferrite E80 core.

The MOSFETs used for the Buck-Boost converters are IXFH40N50Q2. The TDS5034B oscilloscope from Tektronix and associated measurement and analysis software are used to capture the experimental waveforms and perform power quality analysis.

Table 3.4 Parameters of the AC/DC Rectifier for Experiment

Parameter	Value
Output power	270 W
Transformer primary voltage (L-L RMS)	60 V
Transformer secondary voltage (L-L RMS)	25 V (two in series)
Transformer leakage inductance	0.3 mH
ESR of upper/lower transformer (equivalent)	(0.28/0.31) $\Omega$
DC side inductor ( $L_{f1}, L_{f2}$ )	2.6 mH
Rectifier output capacitor ( $C_{f1}, C_{f2}$ )	66 $\mu$ F
ESR of $L_{f1}/ C_{f1}/ L_{f2}/ C_{f2}$	(0.52/0.015/0.48/0.015) $\Omega$
Buck-Boost switching frequency	20 kHz
Buck-Boost DC link voltage	65 V
Buck-Boost output filtering inductor	2 mH

As mentioned at the beginning of this section, this setup has some limitations. Based on the analysis in section 3.5, the experimental setup described in Table 3.4 will result in relatively high VA rating of the filter, due to the relatively high leakage inductance and ESR of the transformers.

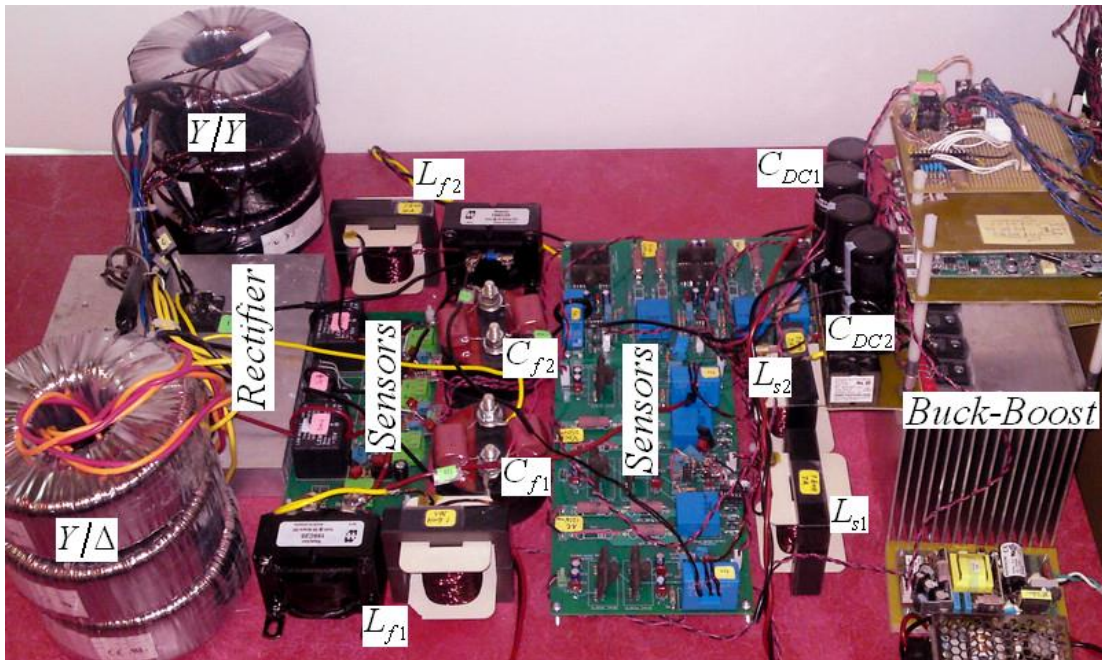
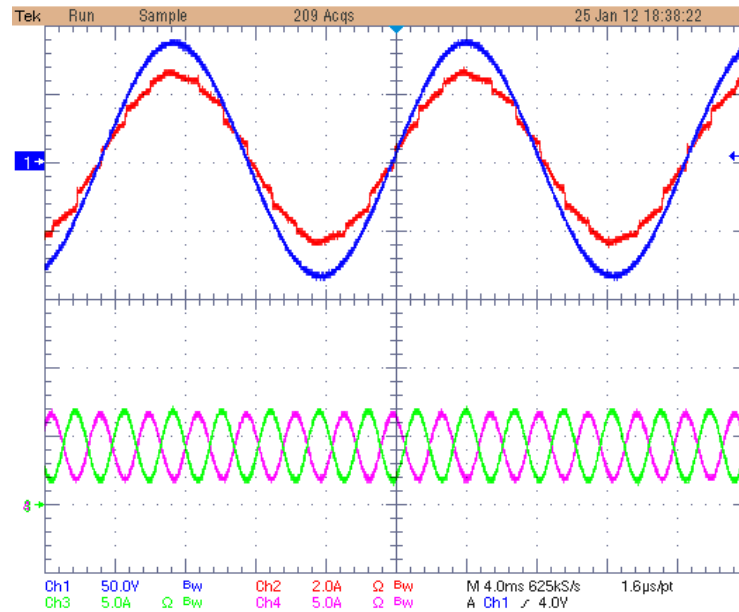


Figure 3.22 Experimental Setup for direct current shaping approach

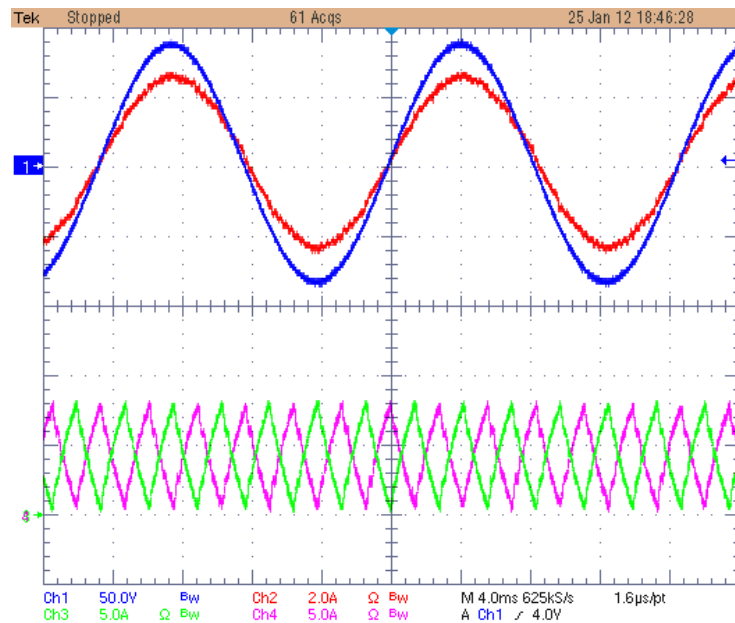
Figure 3.23 shows the experimentally obtained waveforms with and without the compensation current when the load current  $I_L$  is 4.2A. Figure 3.24 shows the compensation currents  $i_{s1}$  and  $i_{s2}$ . At the same load. The improvement of the line current harmonic level is apparent: the THD drops from 4.60% to 2.41%. The magnitude of each harmonic is plotted in Figure 3.25. It is interesting to note that even the initial harmonics are fairly low and much lower than for the 12-pulse rectifier with LC filter design for DC ripple minimization. This is due to the choice of the LC filter that amplifies the 360Hz harmonic in the current. In Figure 3.23, results show that the rectifier current is successfully shaped into the triangular form.



Ch1: line voltage (phase A), 50V/Div Ch2: line current (phase A), 2A/Div

Ch3:  $i_{rec1}$ , 5A/Div Ch4:  $i_{rec2}$ , 5A/Div

(a) Without rectifier current profiling



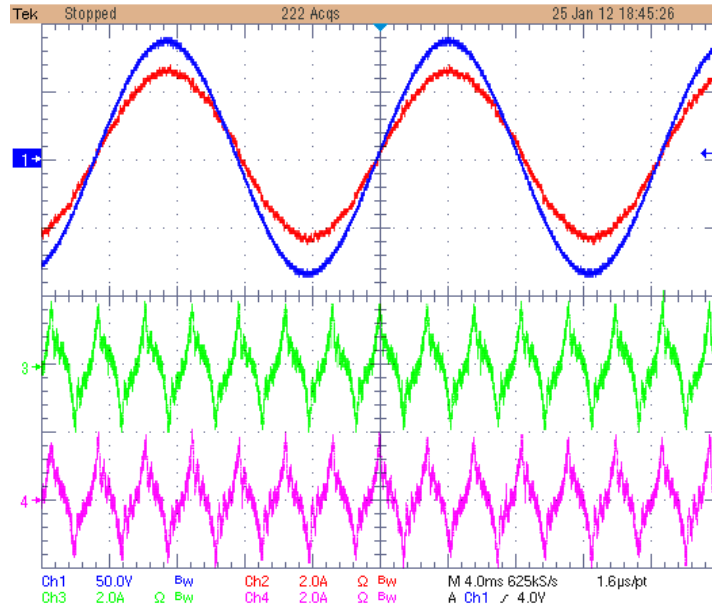
Ch1: line voltage (phase A), 50V/Div Ch2: line current (phase A), 2A/Div

Ch3:  $i_{rec1}$ , 5A/Div Ch4:  $i_{rec2}$ , 5A/Div

(b) With rectifier current profiling

Figure 3.23 Comparison of line current and rectifier output current

Further comparisons are given in Figure 3.26, with different load conditions. Figure 3.26 shows that the proposed method is effective at reducing the harmonics in the input line current even as the rectifier output current becoming discontinuous. The VA rating of the current sources at different load conditions are given in Figure 3.27. It can be seen that the optimized point (where the VA rating is minimized) is when load current is 2.6 A (with load resistance as  $25\Omega$ ). While according to (7) and (8) and Table 3.4, the calculated optimal point is when load resistance is  $22\Omega$ . The VA rating is relatively high because of the high leakage inductance and ESR of the transformer. According to the current flow analysis described in the previous section, and considering the filter parameters from Table 3.4, only 57.1% (for  $i_{s1}$ ) and 56.1% (for  $i_{s2}$ ) of the compensation current goes through loop I. Therefore, almost half of the compensation current goes towards reducing the LC filter current rather than towards shaping the rectifier current into the triangular reference.



Ch1: line voltage (phase A), 50V/Div Ch2: line current (phase A), 2A/Div  
Ch3:  $i_{s1}$ , 2A/Div Ch4:  $i_{s2}$ , 2A/Div

Figure 3.24 Compensation current when the load current  $I_L$  is 4.2A

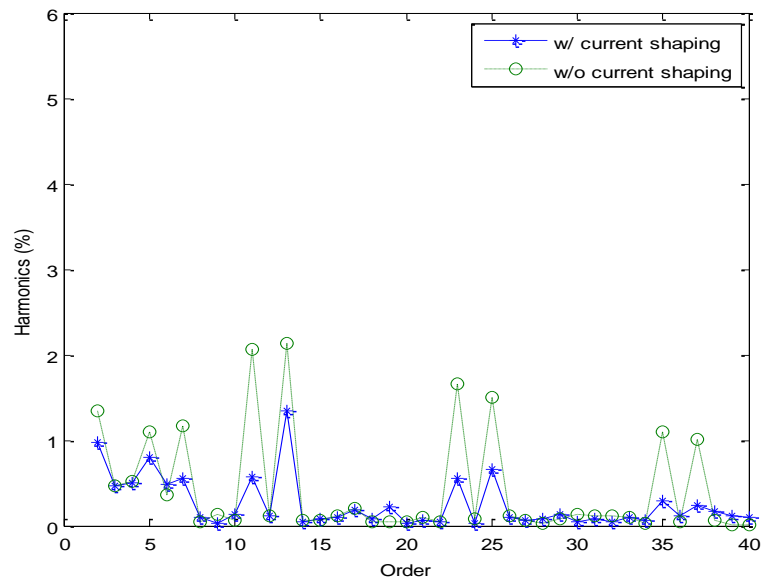


Figure 3.25 Harmonics distribution with and without the current profiling when load current  $I_L$  is 4.2A

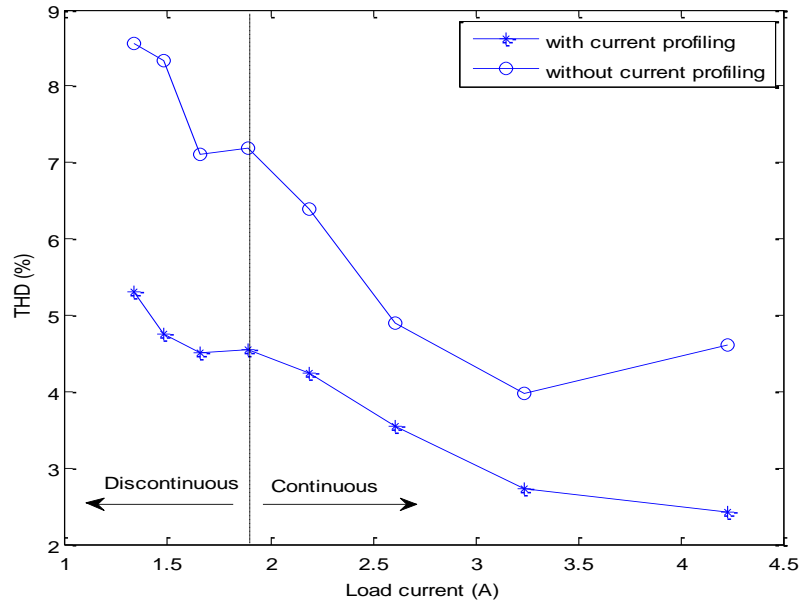


Figure 3.26 Comparison of THD with and without current profiling

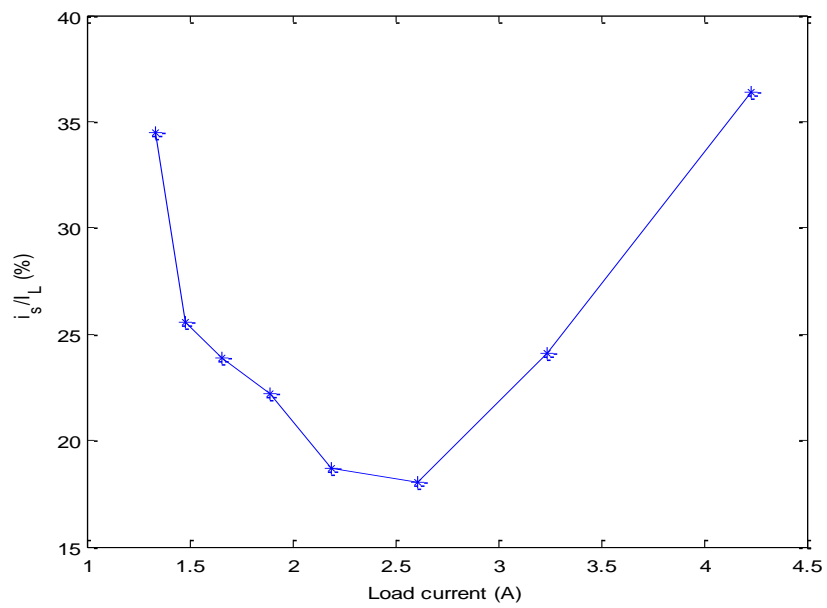


Figure 3.27 VA rating of the current sources  $i_{s1} + i_{s2}$

Figure 3.28 and Figure 3.29 compare the power factor and efficiency of the rectifier with and without the current profiling circuitry enabled. As expected the current profiling circuitry does not significantly affect the power factor of the system, which is close to unity regardless of the load. On average, the efficiency is slightly reduced when the current profiling circuitry is enabled. This is due to the energy lost in the current profiling components that are replenished by the rectifier circuit in the form of a charging current going into  $C_{DC}$ .

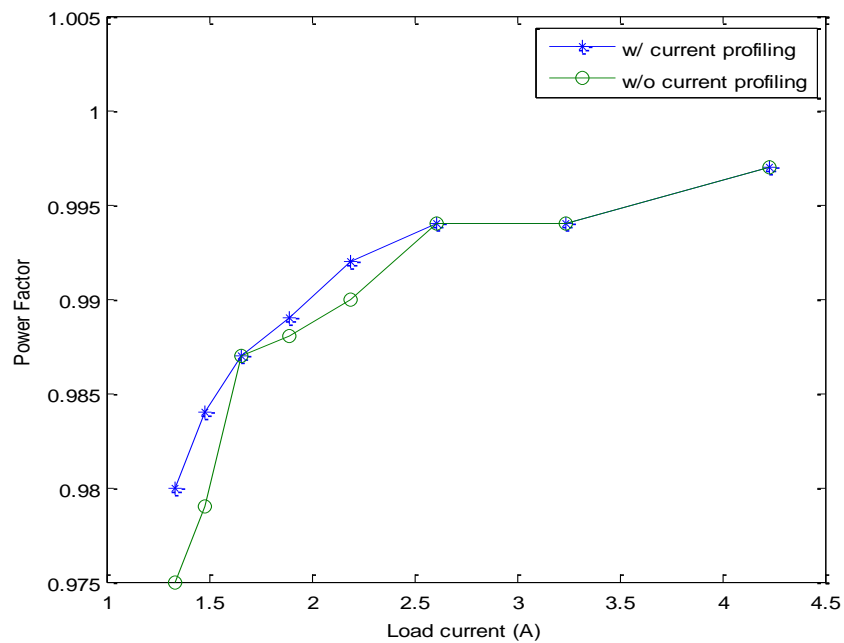


Figure 3.28 Power Factor as a function of load current with and without the current profiling

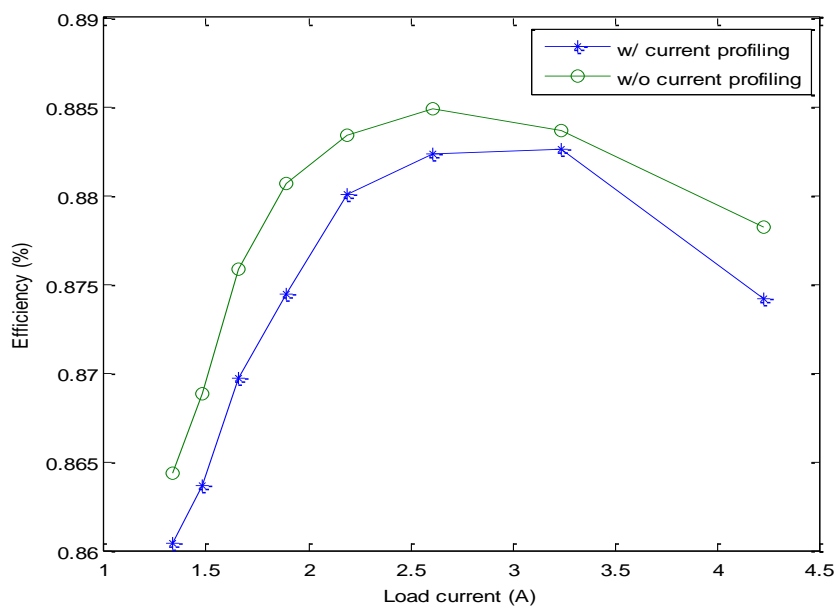
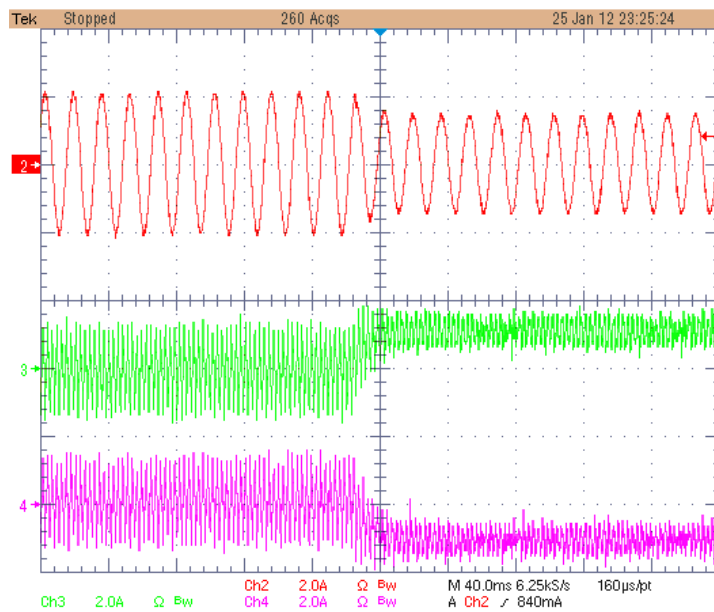


Figure 3.29 Rectifier efficiency as a function of load current with and without the current profiling



Ch2: line current (phase A), 2A/Div Ch3:  $i_{s1}$ , 2A/Div Ch4:  $i_{s2}$ , 2A/Div

Figure 3.30 Active power injection for direct current shaping approach

The active power injection function of the current source  $i_{s3}$  is also verified in experiment. A DC source is connected to the DC link of the two Buck-Boost converters to provide active power. Figure 3.30 shows the transition to active power injection. When  $i_{s3}$  injects active power,  $i_{s1}$  has a positive offset and  $i_{s2}$  has a negative offset. The input line current decreases because of this active power injection. In addition, the lower current from the rectifier results in a smaller compensation current from the filter.

### **3.6 Virtual Impedance Injection Approach to Integrate Energy**

#### **Storage and Achieve both AC and DC Side Harmonics**

##### **Elimination**

In section 3.5 the direct current shaping approach is presented to integrate energy storage and eliminate AC side harmonics for 12-pulse diode rectifier. While this approach is decent and effective in performing the promised functionality, it also has some drawbacks. The main drawback is that this method relies on optimizing the ESR of the LC filter to get better performance (lower VA rating and AC side harmonics). But the ESR can only be optimized at one load condition. At non-optimized load conditions, the performance will get worse. Another problem is that to get optimized ESR, additional resistor may need to be added in series with the LC filter, which will result in unacceptably high power loss, especially for high current applications.

### 3.6.1 Proposed Method-Virtual Impedance Injection

To solve the aforementioned problems, the concept of virtual resistances, as introduced in [62] and [63], is utilized here to change the ESR of the LC filter continuously and thus minimize the THD. Unlike the physical resistors, the virtual resistors will not cause power losses directly – it only redistributes the current. Therefore if the VA rating of the system injecting the resistance is kept low, and the RMS currents are maintained low throughout the system, overall efficiency will be improved.

The proposed method is given in Figure 3.31. Similar to the method presented in section 3.5, this method also have two independent current sources,  $i_{s1}$  and  $i_{s2}$ , and a third current source, which is the combination of  $i_{s1}$  and  $i_{s2}$  ( $i_{s3} = i_{s1} - i_{s2}$ ). The difference is that the two independent current sources are connected in parallel with the capacitors, instead of in parallel with the LC filter as shown in Figure 3.12. Moreover, the function of these two current sources is to inject virtual resistance, instead of directly shape the rectifier output current. With this configuration, the third current source,  $i_{s3}$ , is in parallel with the load. This brings two addition advantages against the method proposed in section 3.5:

(1) The DC output voltage can be compensated by  $i_{s3}$ , while in section 3.5 the inductors between  $i_{s3}$  and the DC output voltage limits the bandwidth of  $i_{s3}$ .

(2) When  $i_{s3}$  is used to inject active power, the active power is directly sent to the load, while in section 3.5 the active power needs go through the inductors, which caused additional losses.

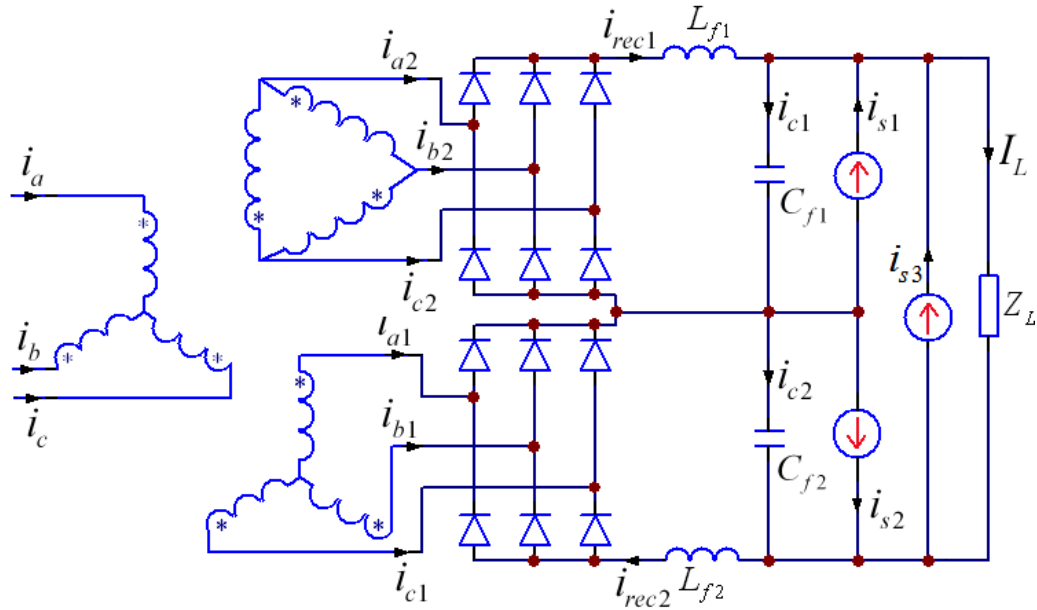


Figure 3.31 Proposed method with parallel connected current sources

As analyzed in section 3.5.2, if the LC filter is designed to be resonant at  $6\omega$ , the AC component of the rectifier output current ( $i_{rec}$ ) will only be determined by the ESR of the LC filter and the rectifier output voltage  $v_{rec}$ . By choosing proper value of the ESR of the LC filter,  $i_{rec}$  could be very close to triangular waveform. However, it is necessary to investigate the AC side harmonics level when  $i_{rec}$  is shaped to close-to-triangular waveform.

The Fourier series expansion of the rectifier output voltages has been derived in (4.5). Similarly to the analysis in section 3.5.2, only the DC and fundamental components are considered

$$\begin{aligned}
 v'_{rec1} &= v_{rec1\_dc} + v_{rec1\_ac1} = \frac{3 \cdot V_p}{\pi} - \frac{6 \cdot V_p}{35\pi} \cdot \cos(6\omega t) \\
 v'_{rec2} &= v_{rec2\_dc} + v_{rec2\_ac1} = \frac{3 \cdot V_p}{\pi} + \frac{6 \cdot V_p}{35\pi} \cdot \cos(6\omega t)
 \end{aligned} \tag{4.16}$$

Note that due to the operation of the transformer, the fundamental AC components of the rectifier voltages are out of phase, which results in the negative sign in the expression for  $v_{rec1\_ac1}$ .

Unlike the approach in section 3.5 which shapes  $i_{rec}$  to be triangular, the rectifier output current will be determined by the load current and the ESR of the LC filter:

$$\begin{aligned} i_{rec1} &= i_{rec1\_dc} + i_{rec1\_ac} = I_L - \frac{v_{rec1\_ac1}}{ESR_{LC}} \\ i_{rec2} &= i_{rec2\_dc} + i_{rec2\_ac} = I_L + \frac{v_{rec2\_ac1}}{ESR_{LC}} \end{aligned} \quad (4.17)$$

where  $I_L$  is the load current as given in (4.6).

In section 3.5.2 it has been shown that  $i_{rec1\_ac1}$  and  $i_{rec2\_ac1}$  is closest to the triangular waveform when  $I_{rec\_ac}=0.77I_L$  ( $I_{rec\_ac}$  is the peak value of  $i_{rec1\_ac1}$  and  $i_{rec2\_ac1}$ ). Under this condition, the construction of the AC side current of phase A is given in Figure 3.32. Similar analysis can be applied to other two phases. The resulting current at the output of the rectifier can be expressed as:

$$\begin{aligned} i_{rec1} &= i_{rec1\_dc} + i_{rec1\_ac} = I_L - 0.77I_L \cdot \cos(6\omega t) \\ i_{rec2} &= i_{rec2\_dc} + i_{rec2\_ac} = I_L + 0.77I_L \cdot \cos(6\omega t) \end{aligned} \quad (4.18)$$

Following the diagrams in Figure 3.32, the line current can be expressed as a function of  $i_{rec1}$  and  $i_{rec2}$ .

$$\begin{aligned} i_{a1} &= \frac{\sqrt{3}I_a}{4I_L} \cdot i_{rec1} \cdot S \angle 30^\circ \\ i_{c1} &= \frac{\sqrt{3}I_a}{4I_L} \cdot i_{rec1} \cdot S \angle 150^\circ \\ i_{a2} &= \frac{\sqrt{3}I_a}{4I_L} \cdot i_{rec2} \cdot S \angle 0^\circ \end{aligned} \quad (4.19)$$

where  $S$  is defined as:

$$S = \frac{2\sqrt{3}}{\pi} \left( \sin(\omega t) - \frac{1}{5} \sin(5\omega t) - \frac{1}{7} \sin(7\omega t) + \frac{1}{11} \sin(11\omega t) + \frac{1}{13} \sin(13\omega t) \dots \right) \quad (4.20)$$

which is the switching function shown in Figure 3.32.

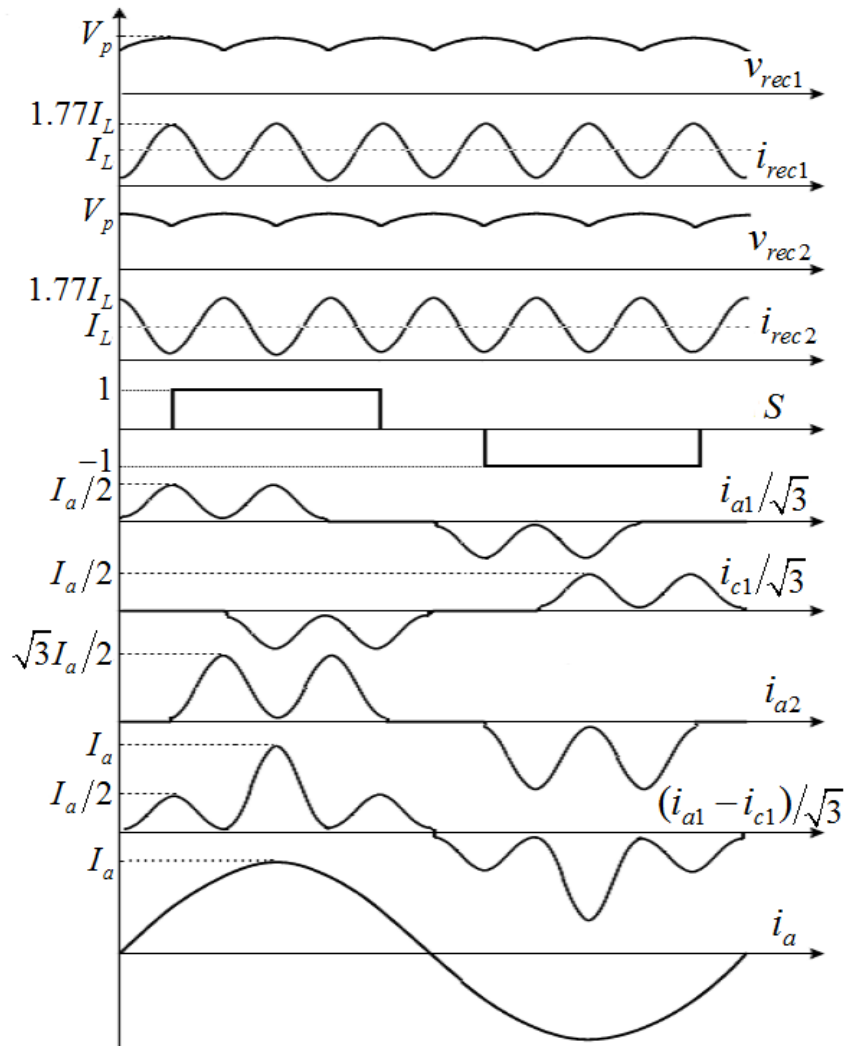


Figure 3.32 Construction of the AC input current for virtual impedance injection approach

The AC side phase A current  $i_a$  can be expressed as:

$$i_a = \frac{i_{a1} - i_{c1}}{\sqrt{3}} + i_{a2} \quad (4.21)$$

By numerically evaluating (4.18)~(4.21), the AC side line current THD can be calculated as 2.1%, which proves that shaping the rectifier current into a sinusoid rather than the triangular waveform results in an acceptable THD. Although the triangular shape gives a lower THD (1%) in theory, these results are hard to achieve in practice.

To get the desired amplitude ( $0.77I_L$ ) of  $I_{rec\_ac}$ , the required ESR has been calculated in section 3.5.2 and will be rewritten here

$$ESR_{LC\_opt} = \frac{R_L}{35 \cdot 0.77} \quad (4.22)$$

The implementation of this method is given in Figure 3.33. Two Buck-Boost converters are used to implement the current sources. The DC link of the Buck-Boost converters can be used to interface energy storage systems if active power injection is needed.

As analyzed in section 3.5.2, the two 6-pulse rectifiers in a 12-pulse rectifier can be decoupled if only the fundamental component of rectifier output voltage is considered and the LC filter is resonant at 6 times of line frequency ( $\omega' = 6\omega$ ). The equivalent circuit of the 6-pulse rectifier is given in Figure 3.34. In this diagram the voltage source represents the  $6\omega$  component of the rectifier voltage, and  $i_s$  represents the current source that will be used to inject the virtual resistance (VR). As suggested by (4.22), the purpose is optimizing the total ESR of the LC filter. Therefore, there are two possible positions for injecting virtual resistance, as given in Figure 3.34 ( $VR_1$  and  $VR_2$ ).

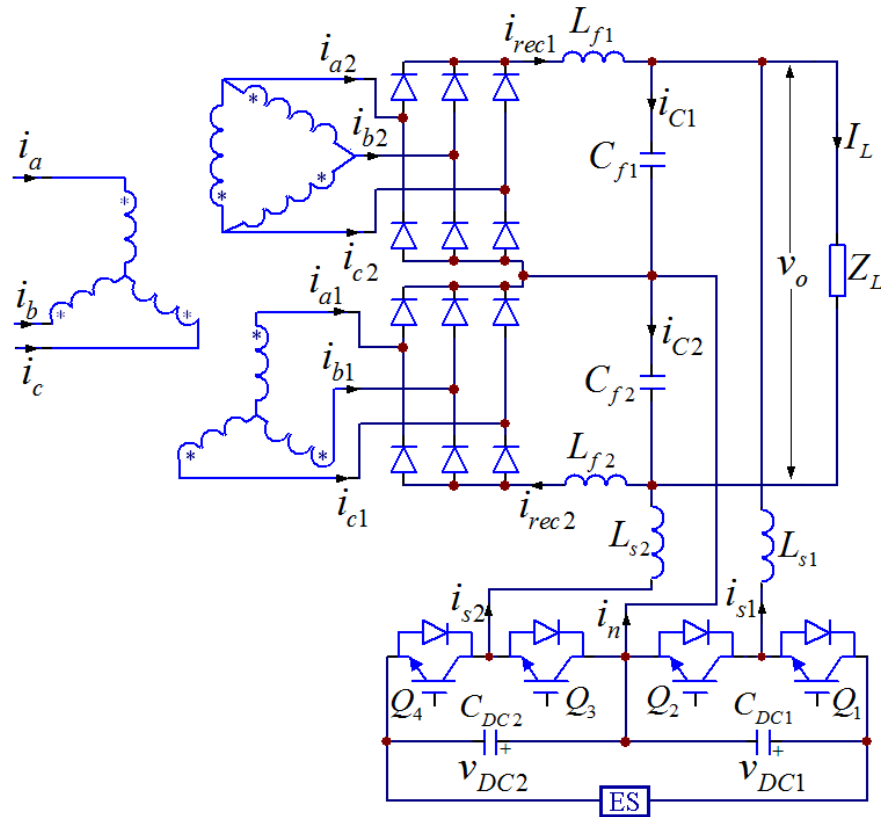


Figure 3.33 Configuration of the proposed AC/DC rectifier with current sources formed by two buck-and-boost converters

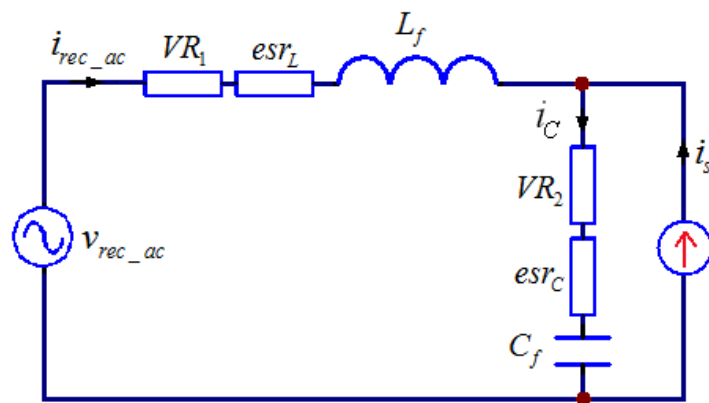
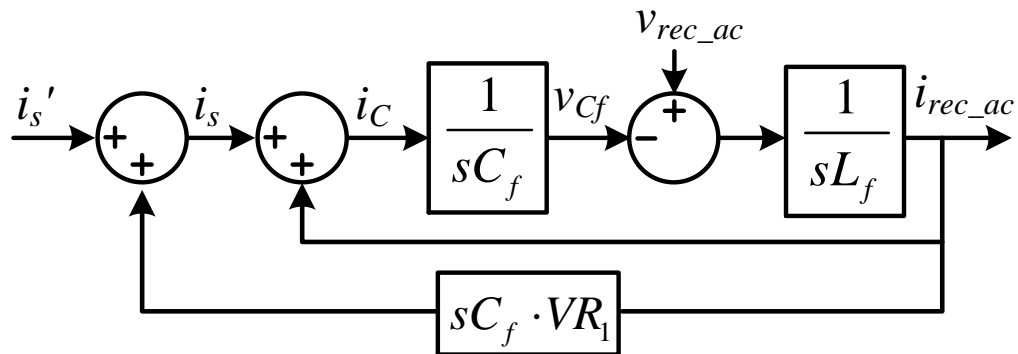
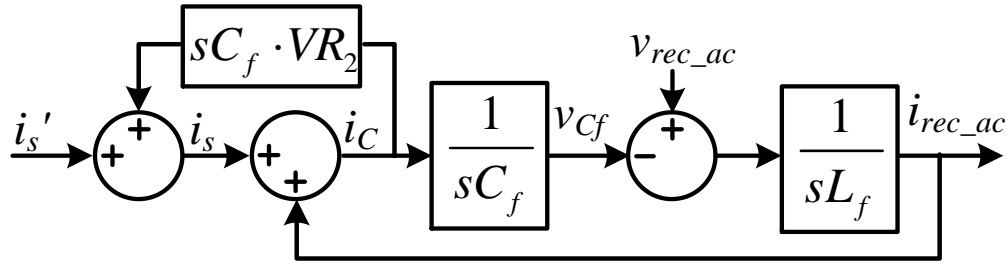


Figure 3.34 Equivalent circuit of the 6-pulse rectifier with parallel connected current source and virtual resistors



(a) Virtual resistor in series with the inductor



(b) Virtual resistor in series with the capacitor

Figure 3.35 Block diagram model of the 6-pulse rectifier equivalent circuit with virtual resistors

The implementation of the virtual resistor can be determined by looking at the transfer function derived from Figure 3.34. The resulting block diagrams are given in Figure 3.35. The detailed derivation of the block diagrams can be found in [62] and [63], which use the same equivalent circuit. From Figure 3.35 it can be observed that injecting either  $VR_1$  or  $VR_2$  requires an additional feedback to the  $i_s$  command. This additional feedback loop is added to the current command in order to emulate the effect of a physical resistor. The value of  $VR$  determines the magnitude of the injected resistance. Therefore the virtual resistor injection

can be achieved by controlling the output of the current source. To inject a virtual resistor in series with  $L_f$ , a feedback from the derivative of rectifier output current is added to the current source command. For injecting virtual resistor in series with  $C_f$ , a feedback from the derivative of capacitor current is added to the current source command. Considering that the switching harmonics presented in the capacitor current, it is preferable to take the derivative of the inductor current. Therefore, the virtual resistance will be injected in series with  $L_f$ .

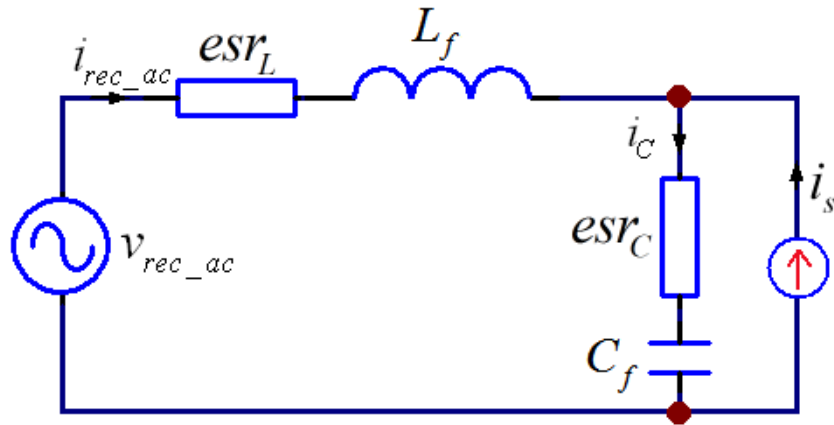


Figure 3.36 Equivalent circuit of the 6-pulse rectifier with parallel connected current source

To better understand the effect of the injected virtual resistor, the equivalent circuit, as given in Figure 3.36, will be analyzed. If the current source is only used to inject virtual resistance  $VR_1$ , (i.e.  $i_s' = 0$  in Figure 3.35(a)), we can determine  $i_s$  as:

$$i_s = j\omega' C_f \cdot VR_1 \cdot i_{rec\_ac} \quad (4.23)$$

where  $\omega' = 6\omega$  and  $\omega$  is the line frequency. Also note that the injected virtual resistance could be either positive or negative. When the physical ESR of the LC filter is too low, the current source needs to inject positive virtual resistance. When the physical ESR of the LC filter is

too high, the current source needs to inject negative virtual resistance. The total ESR,  $VR_I + esr_L + esr_C$ , should be positive to ensure that the AC components of rectifier output voltage and current are in phase.

Applying KCL to the node of the circuit in Figure 3.36, there is:

$$\vec{I}_C = \vec{I}_{rec\_ac} + \vec{I}_s = \vec{I}_{rec\_ac} + j\omega' C_f \cdot VR_1 \cdot \vec{I}_{rec\_ac} \quad (4.24)$$

Simplifying (4.24) we get:

$$\begin{aligned} I_C \angle \theta_C &= I_{rec\_ac} \angle \theta_{rec} + \omega' C_f \cdot VR_1 \cdot I_{rec\_ac} \angle (\theta_{rec} + \frac{\pi}{2}) \\ &= \sqrt{1 + (\omega' C_f \cdot VR_1)^2} \cdot I_{rec\_ac} \angle (\theta_{rec} + \alpha) \end{aligned} \quad (4.25)$$

where

$$\alpha = \tan^{-1}(\omega' C_f \cdot VR_1) \quad (4.26)$$

Applying KVL to the circuit in Figure 3.36, there is:

$$\vec{V}_{rec\_ac} = j\omega' L_f \cdot \vec{I}_{rec\_ac} + esr_L \cdot \vec{I}_{rec\_ac} + \frac{\vec{I}_C}{j\omega' C_f} + esr_C \cdot \vec{I}_C \quad (4.27)$$

Substituting (4.24) into (4.27)

$$\begin{aligned} \vec{V}_{rec\_ac} &= \left[ (esr_L + esr_C + VR_1) + j \left( esr_C \cdot \omega' L_f \cdot VR_1 + \omega' L_f - \frac{1}{\omega' C_f} \right) \right] \cdot \vec{I}_{rec\_ac} \\ &\doteq \left[ (esr_L + esr_C + VR_1) + j \left( \omega' L_f - \frac{1}{\omega' C_f} \right) \right] \cdot \vec{I}_{rec\_ac} \end{aligned} \quad (4.28)$$

Note that in the derivation of (4.28),  $esr_C \cdot \omega' L_f \cdot VR_1$  is assumed to be negligible. In (4.28), since the resonance of the LC filter is set at  $\omega'$ , the imaginary component of the impedance is zero. In this case, the rectifier voltage and current components  $v_{rec\_ac}$  and  $i_{rec\_ac}$  are in phase as desired. Also, the amplitude of the AC component of the rectifier output current  $i_{rec\_ac}$  is

controlled by the injected virtual resistance  $VR_I$ . The phasor diagram representing the virtual resistance injection is shown in Figure 3.37.

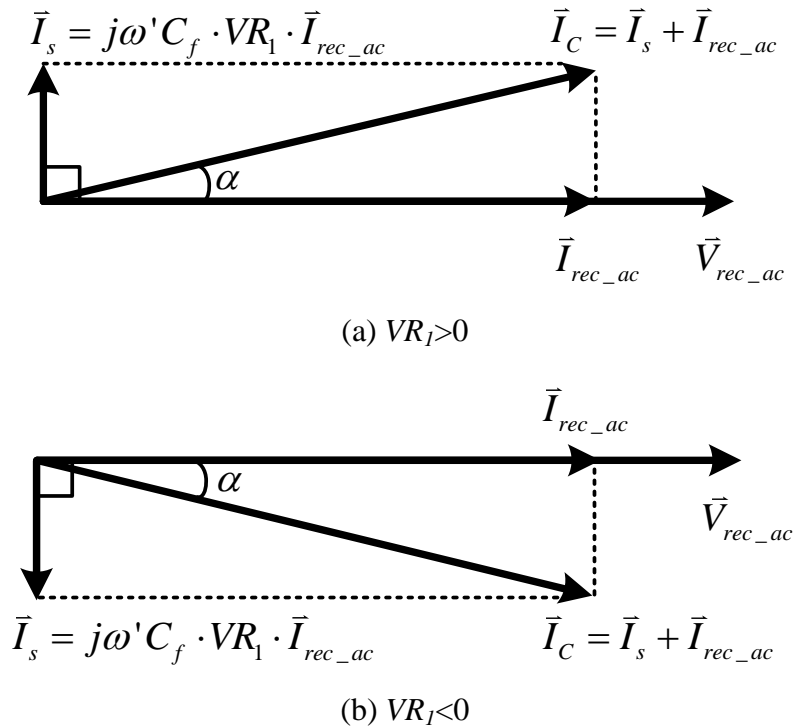


Figure 3.37 Phasor diagram of the 6-pulse rectifier with virtual resistance injection

In practice the assumption that the filter is in resonance (i.e. that  $\omega' L_f = 1 / \omega' C_f$ ) may not be satisfied due to parameter tolerance and variation [64]. This issue can be addressed by injecting a *virtual reactance* rather than virtual resistance. In this case, the current source needs to inject:

$$\vec{I}_s = j\omega' C_f \cdot VR_I \cdot \vec{I}_{rec\_ac} + \vec{I}_{comp} \quad (4.29)$$

Re-evaluating (4.24) and (4.27) while neglecting  $esr_c$  and  $esr_L$  we have:

$$\vec{V}_{rec\_ac} \doteq VR_1 \cdot \vec{I}_{rec\_ac} + j \left[ \left( \omega' L_f - \frac{1}{\omega' C_f} \right) \cdot \vec{I}_{rec\_ac} - \frac{1}{\omega' C_f} \cdot \vec{I}_{comp} \right] \quad (4.30)$$

To maintain  $v_{rec\_ac}$  and  $i_{rec\_ac}$  in phase, the imaginary component of (4.30) needs to be zero, resulting in:

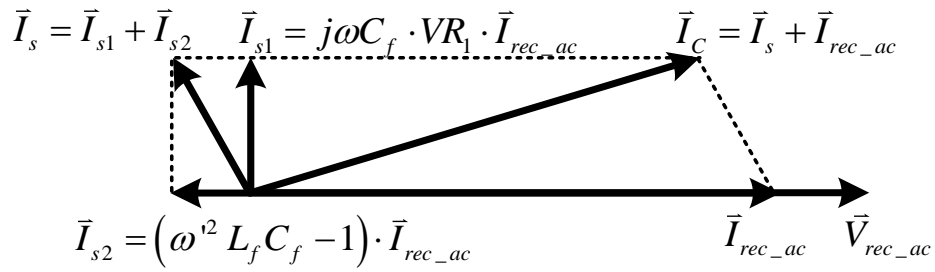
$$\vec{I}_{comp} = (\omega'^2 L_f C_f - 1) \cdot \vec{I}_{rec\_ac} \quad (4.31)$$

Therefore, from (4.29) and (4.31), the injected current becomes:

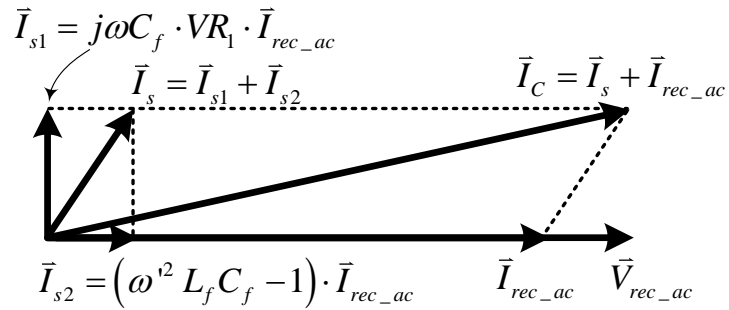
$$\vec{I}_s = j\omega' C_f \cdot VR_1 \cdot \vec{I}_{rec\_ac} + (\omega'^2 L_f C_f - 1) \cdot \vec{I}_{rec\_ac} \quad (4.32)$$

The sign of  $(\omega'^2 L_f C_f - 1)$  depends on the resonant frequency of  $L_f$  and  $C_f$ . If the resonant frequency is higher than  $\omega'$ ,  $(\omega'^2 L_f C_f - 1)$  is negative. If the resonant frequency is lower than  $\omega'$ ,  $(\omega'^2 L_f C_f - 1)$  is positive. The phasor diagram of these two situations are given in Figure 3.38 (with  $VR_1 > 0$ ).

The modified block diagram of the equivalent circuit is given in Figure 3.39. The feedback controller is now proportional and derivative (PD) with parameters given by (4.32).



(a) resonant frequency of  $L_f$  and  $C_f$  is higher than  $\omega'$



(b) resonant frequency of  $L_f$  and  $C_f$  is lower than  $\omega'$

Figure 3.38 Phasor diagram of the 6-pulse rectifier with virtual impedance injection ( $VR_1 > 0$ )

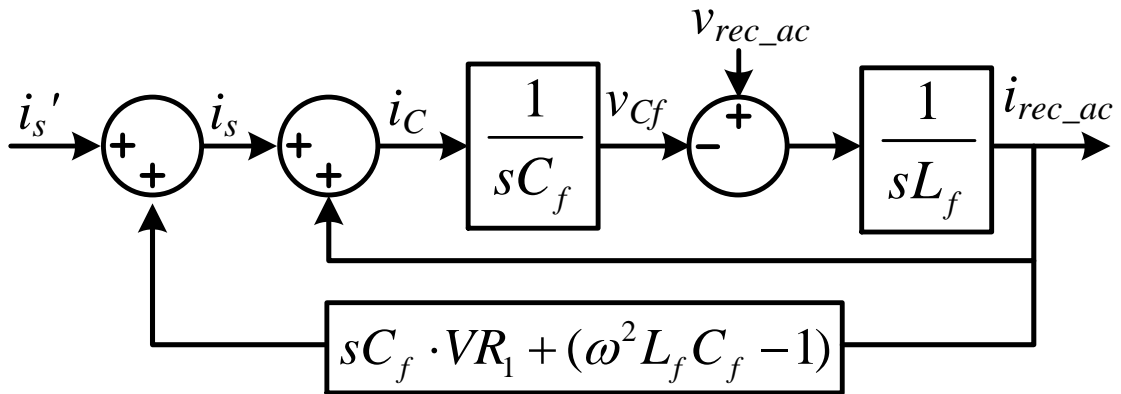


Figure 3.39 Block diagram model of the 6-pulse rectifier equivalent circuit with virtual impedance injection

The control diagram is given in Figure 3.40. Proportional and Derivative control (PD control) is used for the virtual impedance injection. The gains for PD control are given in (4.32). Note that the actual rectifier output currents ( $i_{rec1}$  and  $i_{rec2}$ ) are used instead of the AC components of them, to simplify the controller. Considering that the current component at  $\omega'$  is dominant, this simplification gives an acceptable approximation. Three control loops are included in the controller. The first one serves to compensate the DC output voltage ( $v_o$ ). The second one is for active power injection. And the third one is for maintaining a constant voltage at the Buck-Boost DC link.

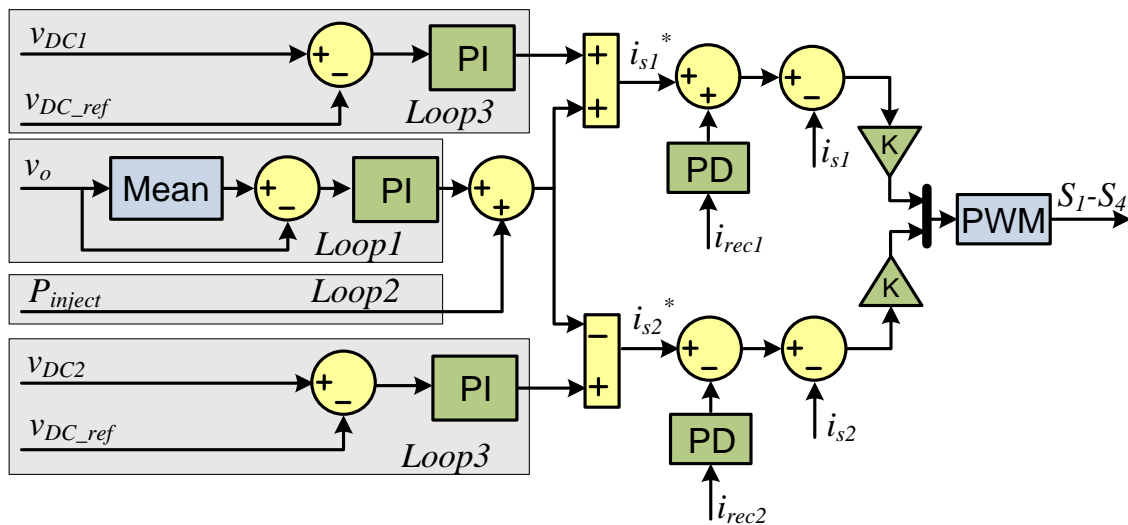


Figure 3.40 Control diagram of the 12-pulse rectifier with parallel connected current sources

Overall, the controller is very simple: the PD controller is determined from (4.32) to ensure that the AC side harmonics are minimized, and the PI controllers are manually tuned to achieve a target response. The DC ripple PI controller gain is chosen to provide an

acceptable DC bus ripple. This controller can be replaced by a proportional controller, as is often done for DC bus ripple controllers [65]. The PI controller that maintains the constant voltage at the Buck-Boost DC link can be very slow, since the dynamics that cause the DC link voltages to diverge are also slow ([66], [67]).

### 3.6.2 Simulation and Experiment Results

To confirm the effectiveness of the proposed approach, simulation and experiment models are built to validate the proposed control of the DC bus energy storage system that results in high AC and DC side power quality. First, the simulation results for the 1.1MW charging station are presented. The focus of the simulations will be the comparison between the approach proposed in this section and the approach presented in section 3.5. Next, a set of experimental results on a small scale prototype are presented to validate the operation of the virtual impedance injection approach.

#### 3.6.2.1 Simulation Results

To verify the effectiveness of the proposed virtual resistance injection method (VR method), a simulation model is built in Matlab Simulink, with switching model of the Buck-Boost converters. The method proposed in section 3.5 is also simulated for comparison. The parameters for the simulation are given in Table 3.5. Compared with the simulations in section 3.5, the only difference is that the total ESR of the LC filter is  $4\text{m}\Omega$ , instead of  $18.6\text{m}\Omega$  in section 3.5 ( $ESR_L=10\text{m}\Omega$ ,  $ESR_C=8.6\text{m}\Omega$ ).

The simulation results are given in Figure 3.41. Referring to Figure 3.41(a), the THD level is comparable at full load, but the VR method delivers better results at low load. It should be noted here that the method proposed here and in section 3.5 are unique in that they

are able to control the rectifier THD even when the original rectifier current is discontinuous. For the VR method the THD is kept close to 2% as the load is changed. This is in line with the analytical results in the previous section that predict a THD of 2.1%. The discrepancy between the simulation and the experiment is due the effect of neglected higher order harmonics in the analysis that are present in simulations. Referring to Figure 3.41(b), the DC output voltage ripple is substantially lower than the method in section 3.5 that does not compensate the DC voltage.

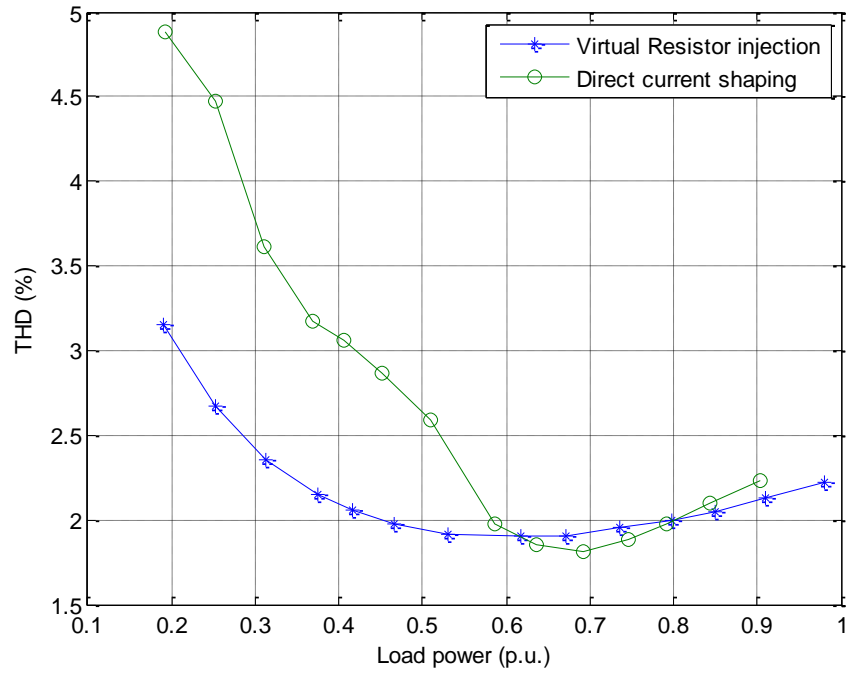
Table 3.5 Parameters of the Rectifier for Simulation

Parameter	Value
Output power	1.1 MW
Rated load resistance	0.37 $\Omega$
Transformer primary voltage (line to line RMS)	4160 V
Transformer secondary voltage (line to line RMS)	240 V (two in series)
Transformer leakage inductance (equivalent)	5 $\mu\text{H}$ (0.75% p.u.)
DC side inductor ( $L_f$ )	44.3 $\mu\text{H}$
ESR of $L_f$ and $C_f$	2 m $\Omega$ /2 m $\Omega$
Rectifier output capacitor ( $C_{f1}, C_{f2}$ )	3.6 mF
Buck-Boost switching frequency	20 kHz
Buck-Boost DC link voltage ( $V_{DC1}, V_{DC2}$ )	600 V
Buck-Boost output filtering inductor ( $L_{s1}, L_{s2}$ )	100 $\mu\text{H}$

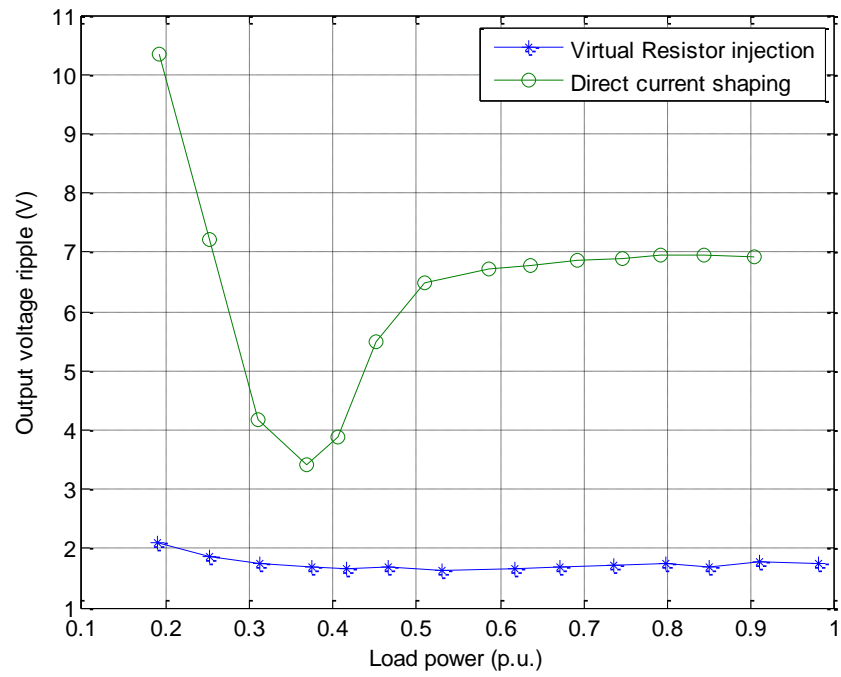
The proposed method also has much lower power losses on the ESR due to the substantially lower LC filter ESR. Referring to Figure 3.41(d), the VR method has a larger VA rating at light load due to the need to inject substantial virtual resistance into the LC filter to achieve the desired filter ESR. But at full load, the VR method has much lower VA rating

than the method proposed in section 3.5. The VA rating can be further reduced with a larger physical resistance of the LC tank at the expense of higher copper losses in the filter.

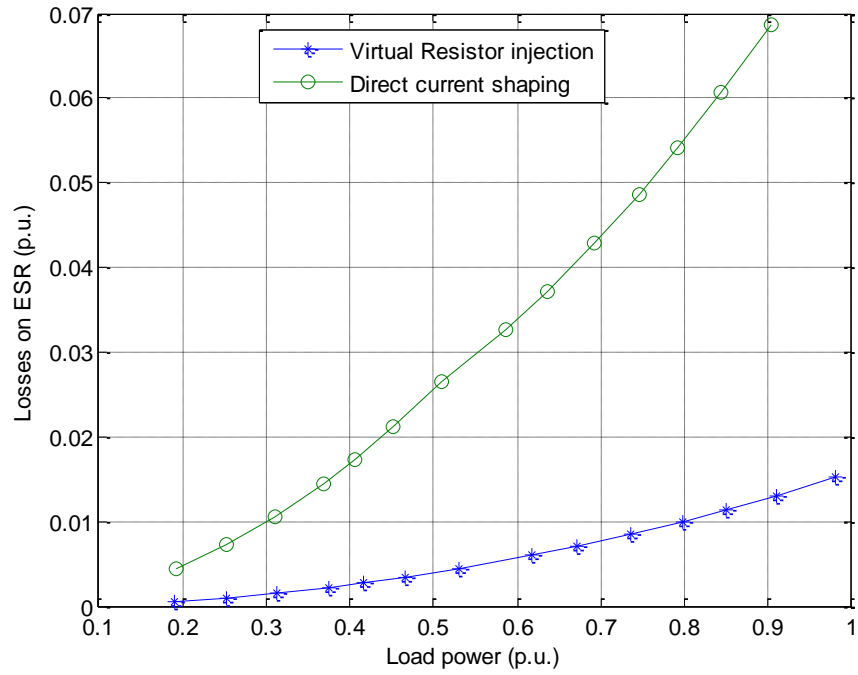
Figure 3.41 Comparison of proposed method (virtual resistor injection) and method in section 3.5 (direct current shaping)



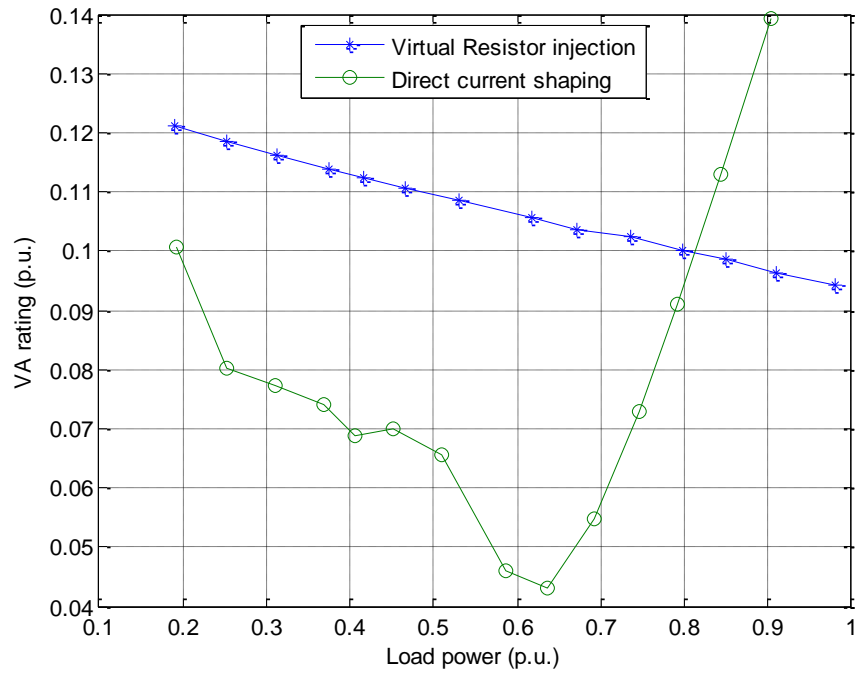
(a) THD



(b) DC output voltage ripple



(c) Power losses on ESR of LC filters



(d) VA rating of the current sources

### 3.6.2.2 Experiment Results

A small scale experimental setup (Figure 3.42) is built to verify the functionalities of the proposed system. The specifications of this setup are given in Table 3.6. The 3-phase transformer consists of three single phase transformers (VPT48-10400) and the secondary windings are rewound to get desired voltage level. The 12-pulse diode rectifier consists of two 3-phase diode bridges (SC50VB80). The inductors were hand-wound around E80 ferrite cores. The MOSFETs used for the Buck-Boost converters are IXFH40N50Q2. The TDS5034B oscilloscope from Tektronix and WT3000 precision power analyzer from YOKOGAWA are used to capture the experimental waveforms and perform power quality analysis. The controller is implemented by using OPAL-RT real time simulator.

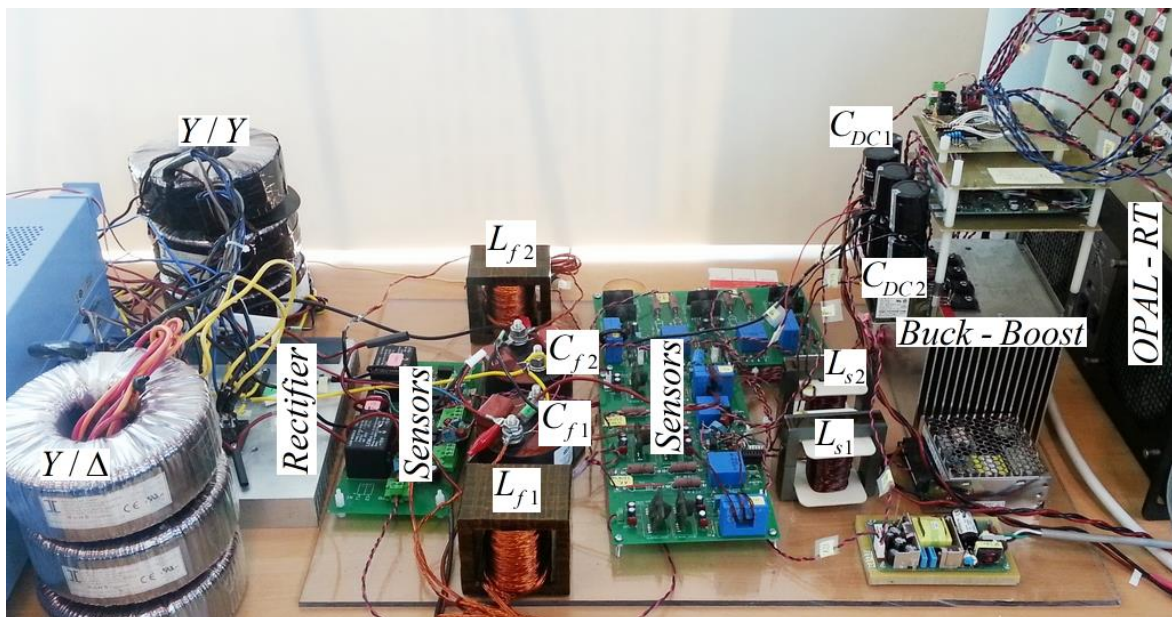


Figure 3.42 Experiment setup for virtual impedance injection approach

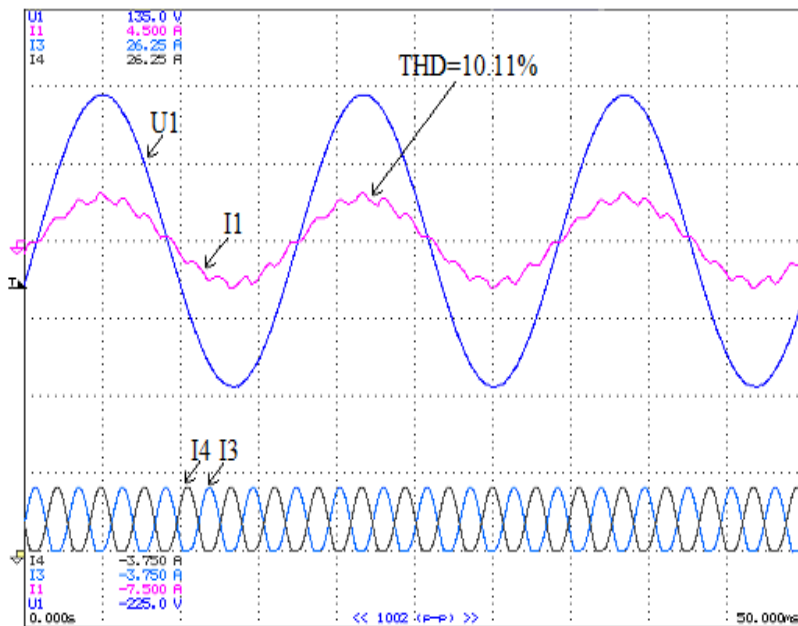
Table 3.6 Parameters of the Rectifier for Experiment

Parameter	Value
Output power	390 W
Transformer primary voltage (L-L RMS)	60 V
Transformer secondary voltage (L-L RMS)	25 V (two in series)
Transformer leakage inductance	0.3 mH
ESR of upper/lower transformer (equivalent)	(0.28/0.31) $\Omega$
DC-side inductor ( $L_{f1}, L_{f2}$ )	2.6 mH
Rectifier output capacitor ( $C_{f1}, C_{f2}$ )	66 $\mu$ F
ESR of $L_{f1}/C_{f1}/L_{f2}/C_{f2}$	(0.11/0.015/0.10/0.015) $\Omega$
Buck-Boost switching frequency	20 kHz
Buck-Boost DC link voltage	65 V
Buck-Boost output filtering inductor	2 mH

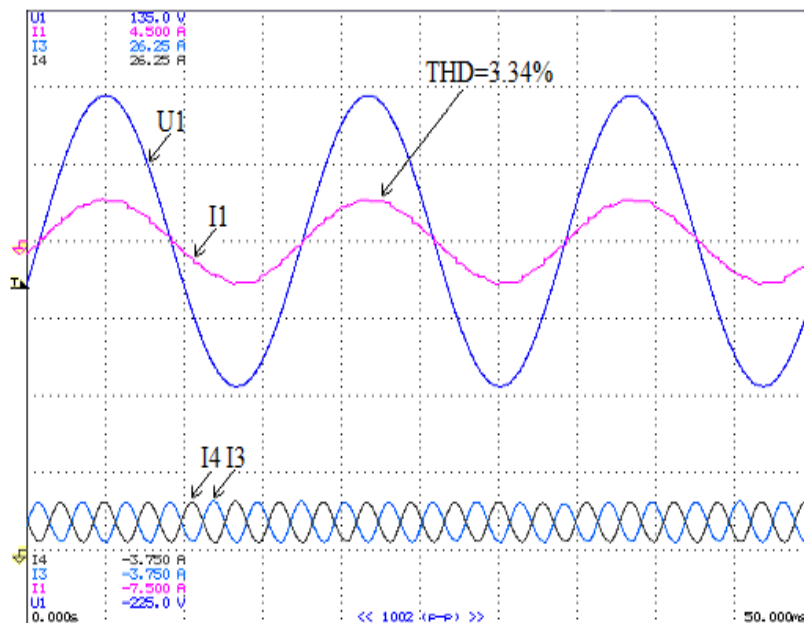
The experimentally obtained waveforms of the line current and voltage and the rectifier output currents are given in Figure 3.43 and Figure 3.44. Figure 3.43 shows the light load results. In this condition, the rectifier current is discontinuous without the virtual resistance injection, as shown in Figure 3.43(a). With the virtual resistance injection, the total ESR is increased to the desired value and the current becomes continuous, as shown in Figure 3.43(b). The line current waveform is substantially improved with the THD decreasing from 10.11% to 3.34%.

At heavy load, shown in Figure 3.44, the target ESR of the LC filter is lower than the physical ESR. This condition is shown in Figure 3.44(a). With the virtual resistance injection, which now has a negative value, the total ESR is decreased to the desired value, and the line current THD is reduced to 2.18% as shown in Figure 3.44(b). The harmonic distribution in the line current corresponding to the operating conditions shown in Figure

3.44 is given in Figure 3.45. The 11<sup>th</sup> and 13<sup>th</sup> harmonics, which are the main harmonic components for the 12-pulse diode rectifier, are substantially reduced.



(a) Without virtual resistor injection

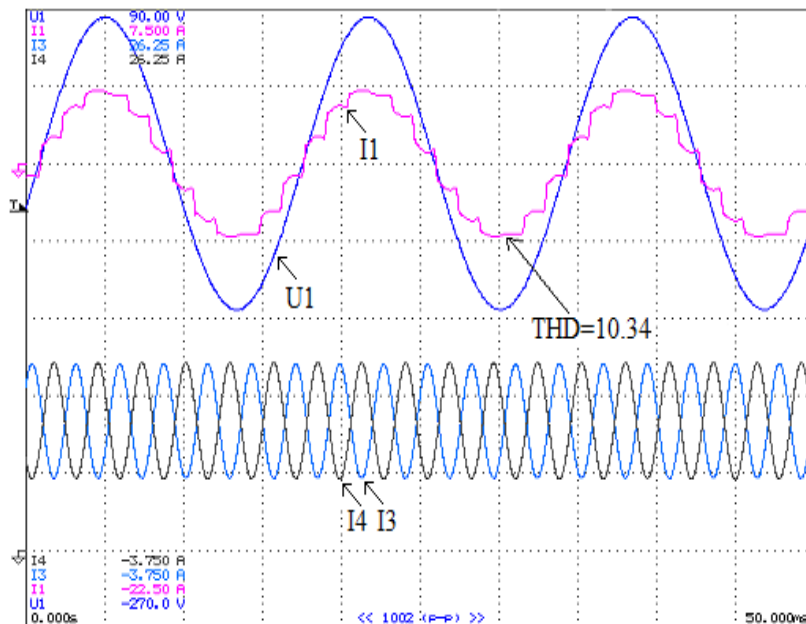


(b) With virtual resistor injection

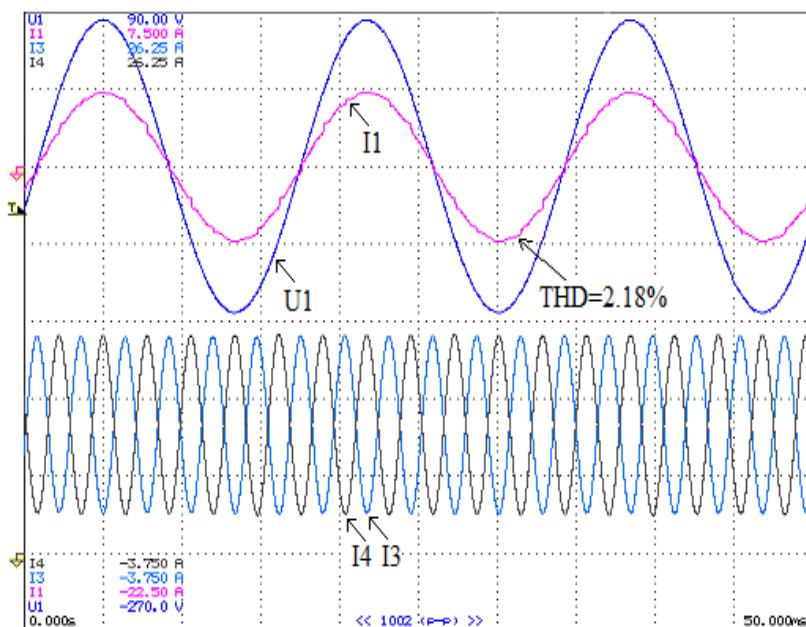
U1: line voltage (Phase A), 45V/div I1: line current (Phase A), 1.5A/div

I3:  $i_{rec2}$ , 3.75A/div I4:  $i_{rec1}$ , 3.75A/div time: 5ms/div

Figure 3.43 Comparison of line current and rectifier output current for light load (load current is 1.4A)



(a) Without virtual resistor injection



(b) With virtual resistor injection

U1: line voltage (Phase A), 45V/div I1: line current (Phase A), 3.75A/div

I3:  $i_{rec2}$ , 3.75A/div I4:  $i_{rec1}$ , 3.75A/div time: 5ms/div

Figure 3.44 Comparison of line current and rectifier output current for heavy load (load current is 6.2A)

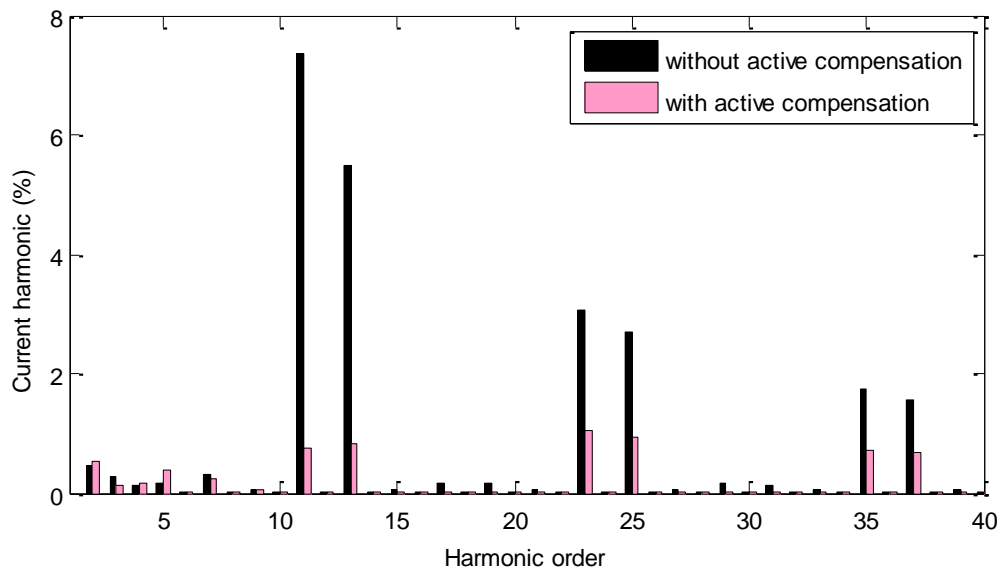


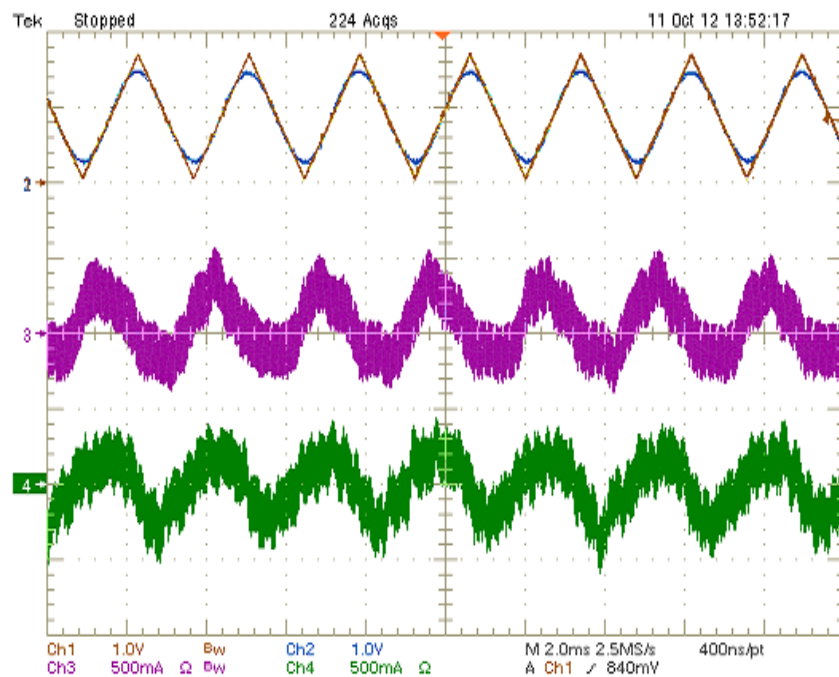
Figure 3.45 Harmonics distribution of line current with and without virtual resistance injection (load current is 6.2A)

Figure 3.46 displays the waveforms of the injected currents  $i_{s1}$  and  $i_{s2}$ . The waveforms are fairly smooth which suggests that no high frequency component is presented in the injected currents. Thus the bandwidth of the controller does not need to be high. The figure also shows the rectifier output current and the triangular waveform (generated by the digital controller and displayed through the digital-to-analog converter) that was used as the reference signal in the approach in section 3.5. The experimental results show that the desired ESR was successfully actuated resulting in a close match between the two waveforms.

Figure 3.47 compares the line current THD with and without the VR injection for different load conditions. It is clear that with the virtual resistance injection, the improvement of the line current and output voltage are significant. The line current THD is reasonably close to theoretical value (2.1% as calculated in section 3.6.1) for most load conditions. The

discrepancy comes from the fact that higher order harmonics were ignored in the theoretical analysis.

The load side output voltage ripple, shown in Figure 3.48, is substantially reduced when the active compensation is actuated. Therefore, the PI controller is behaving as expected. It is interesting to note that the voltage ripple is relatively low even without active compensation. This is the result of the dominant ripple-producing component at  $6\omega$  being canceled out at the capacitor terminals when the two LC filters are in resonance.



Ch1: desired  $i_{rec1}$ , 3.5A/div Ch2: actual  $i_{rec1}$  (from current sensor), 3.5A/div

Ch3:  $i_{s1}$ , 0.5A/div Ch4:  $i_{s2}$ , 0.5A/div

Figure 3.46 Injected current  $i_{s1}$  and  $i_{s2}$  (load current is 2.2A)

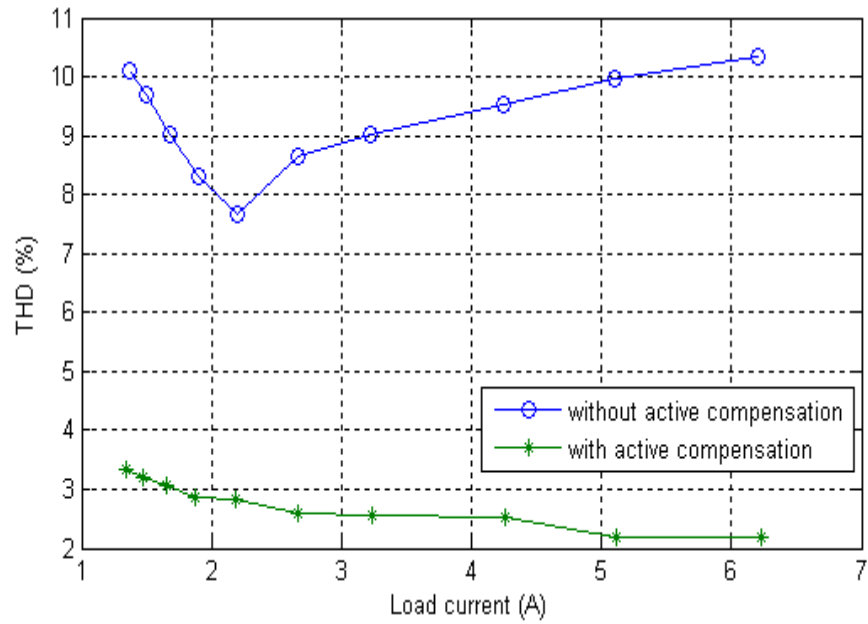


Figure 3.47 Comparison of line current THD with and without virtual resistance injection

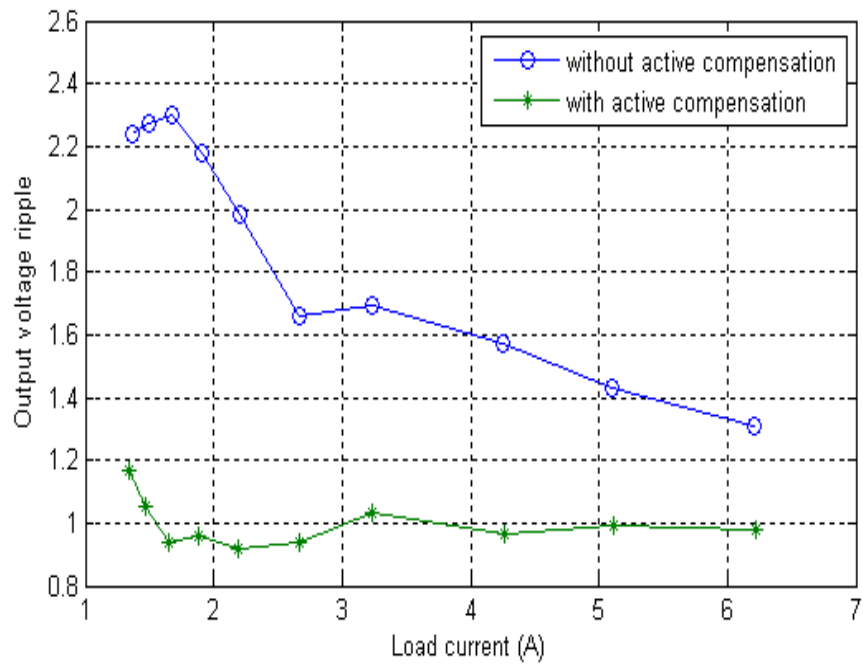


Figure 3.48 Comparison of load side output voltage ripple with and without active compensation

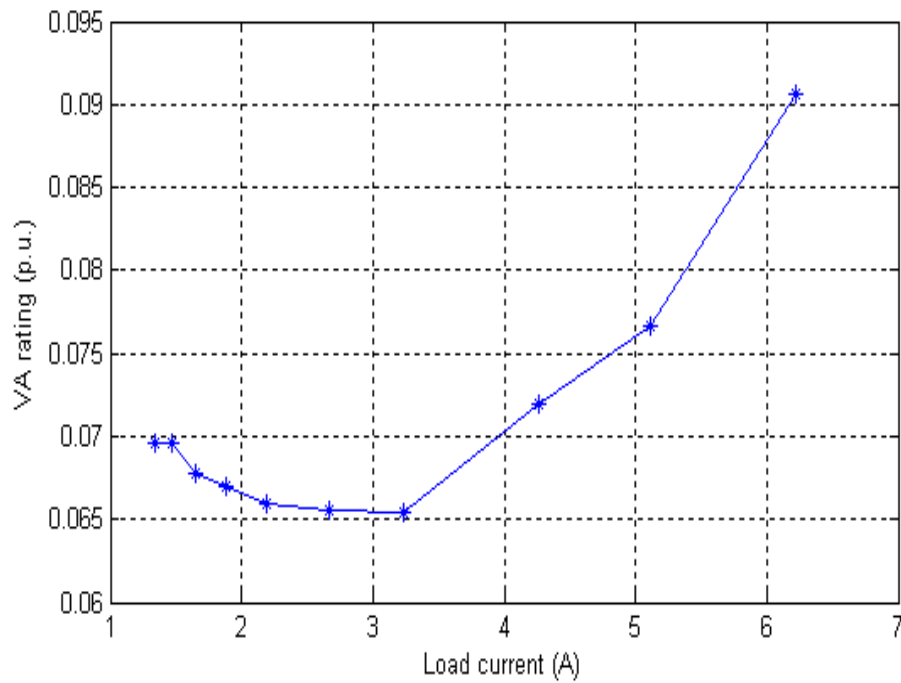
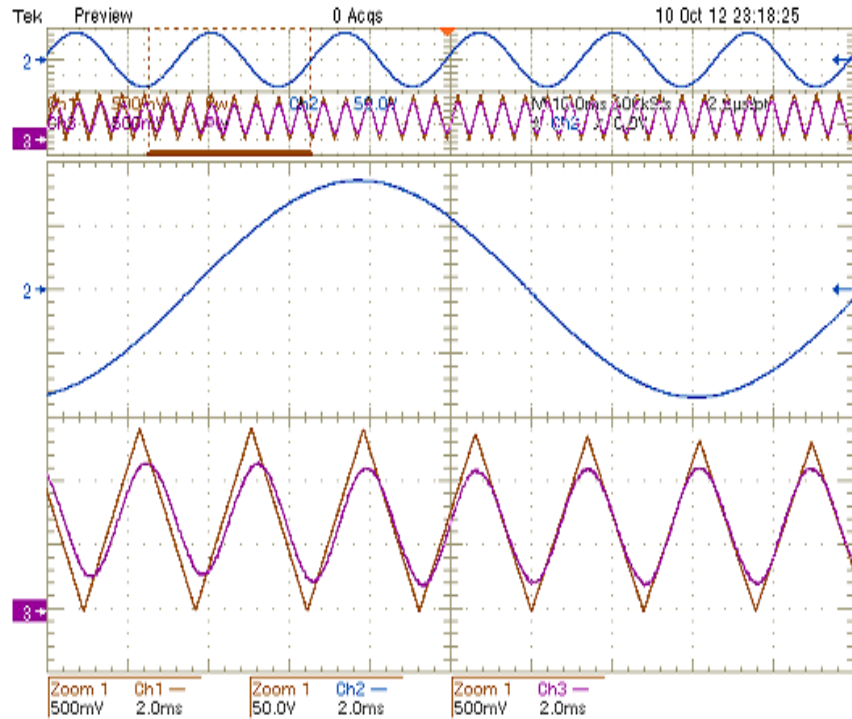


Figure 3.49 VA rating of the current sources

Figure 3.49 gives the VA rating of the currents sources in per unit (with the base as the rated load power). Throughout the load range, the VA rating is kept below 10%. Note that the minimum VA rating can be controlled by choosing an appropriate value of the LC filter ESR. In this case, the full load VA rating could be reduced by reducing the LC filter ESR.



Ch1: desired rectifier output current, 3.5A/div Ch2: line voltage, 50V/div

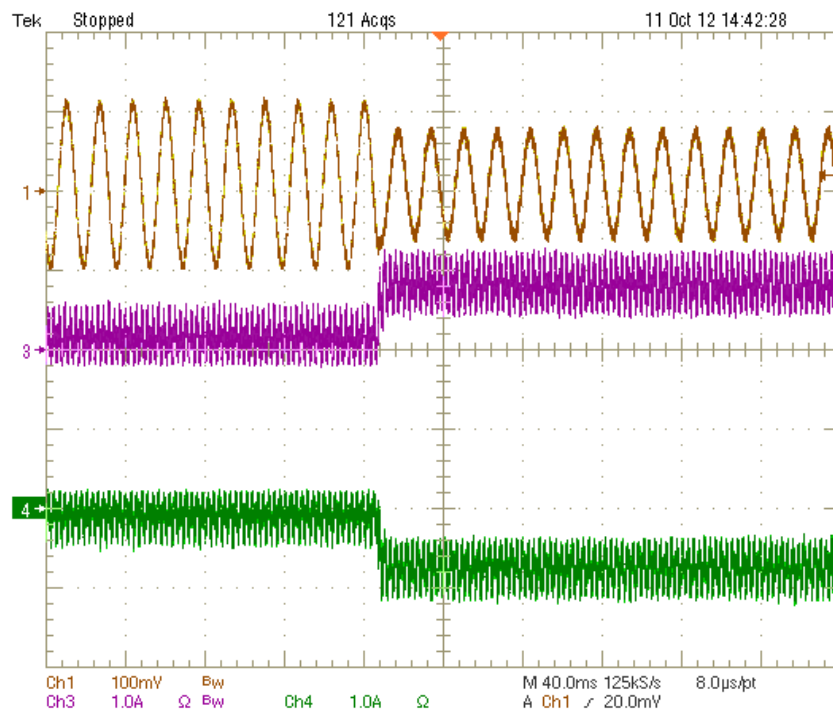
Ch3: actual rectifier output current (from current sensor), 3.5A/div

Figure 3.50 LC filter detuning compensation

To verify that the virtual reactance injection is capable of compensating any detuning in the LC filters, the inductance of the LC filters is changed from 2.6mH to 3.1mH, such that the resonant frequency is lower than  $6\omega$ . To compensate this detuning, the current sources inject additional current defined in (4.31). Figure 3.50 shows the rectifier output current before and after enabling this detuning compensation. The triangular waveform, synchronized with the line voltage, is shown as a reference. It can be seen that before enabling the detuning compensation, the actual rectifier output current is lagging the

triangular reference. After enabling the detuning compensation, the phase shift between the actual and desired rectifier output current is quickly compensated.

The active power injection function of the current source  $i_{s3}$  is also verified in experiment, and the results are displayed in Figure 3.51. When  $i_{s3}$  injects active power,  $i_{s1}$  has a positive offset and  $i_{s2}$  has a negative offset. With the DC load constant, the input line current decreases due to this active power injection.



Ch1: lien current (from current sensor), 1A/div

Ch3:  $i_{s1}$ , 1A/div Ch4:  $i_{s2}$ , 1A/div

Figure 3.51 Active power injection for virtual impedance injection approach

### 3.7 Conclusions

In this chapter two novel ways are presented to minimize the harmonics of a 12-pulse rectifier to meet the IEEE standard [40]. The approach is based on profiling the DC side rectifier current so that the AC side harmonics are minimized. Two alternative approaches are proposed to implement the control as described in Sections 3.5 and 3.6. In section 3.5 a new topology is introduced that will eliminate the AC side harmonics. The chosen topology acts as a current source in parallel with the input rectifier, and is therefore able to directly shape the rectifier output current. In addition, the current source is constructed from a voltage fed Buck-Boost converter, allowing for seamless integration of DC storage into the system. Moreover, the current source is not in the path of the load current, resulting in low VA rating. The VA ratings of the current profiling circuitry is further minimized by exploiting the large ripple component produced by the operation of the rectifier to shape the rectifier output current through the appropriate choice of LC filter parameters.

A modified version of the direct current shaping method is presented in section 3.6, by utilizing the concept of virtual resistance injection to profile the rectifier output current. This concept is further extended to inject virtual reactance, such that the detuning of the LC filters can be compensated. In comparison with the direct current shaping method, the virtual impedance injection method inserts the current sources on the load side, and thus allows for load voltage compensation. The virtual impedance injection method also has lower power loss and better performance for harmonic elimination. The result of the proposed approach is that a set of cascaded bi-directional Buck-Boost converters rated at 10% of the grid tie can provide (a) line current THD of about 2% (b) high quality DC bus voltage and (c) energy

storage integration on the DC bus. Therefore, the system structure remains simple which is desirable for improved reliability and for minimizing the construction and maintenance costs.

In comparison with similar approaches, both proposed methods have the apparent advantages of eliminating the use of low frequency transformers for shaping the rectifier output current, providing energy storage interface to the system, and functioning regardless of the continuity of the initial rectifier output current.

In comparison with traditional active or passive or hybrid power filters as presented in [57]–[59], the proposed active filter has the obvious advantage that it is located in the DC side and thus can be used to integrate the energy storage and compensate DC side voltage ripple as well.

Simulation of a high power industrial AC/DC rectifier verified the parameter optimization of the system, while experimental results show significant reduction of harmonics in the line current. The DC energy storage integration functionality is also verified experimentally.

## **Chapter 4. Modular Design of Cascaded H-Bridge for Energy Storage Integration in AC Distribution System – Dissimilar Batteries Utilization in Community Energy Storage Systems**

Energy storage devices have found many applications such as electrically propelled vehicles, renewable energy systems, uninterruptible power supplies (UPS), etc. Among all kinds of energy storage devices, batteries are among the most important and widely used energy storage devices. As the power level of the battery system keep increasing, it becomes more and more challenging to design the battery management system [68]–[71]. Other than designing more complicated and costly battery management systems, an alternative approach is separating high power high capacity energy storage system into small units and controls them as a fleet to have the same functionalities as a large system. Moreover, inside the small energy storage unit, the battery pack can be further separated into smaller packs and use power converters to interface with each of the small battery packs. It is also possible to modularize the system by designing a module with a small battery pack and a power converter. By assembling a number of this module, an energy storage system is formed. Since the small battery packs are not directly connected together, dissimilar or different batteries can be used in different modules. This not only simplifies the battery management system, but also creates an opportunity to find a secondary use for reclaimed batteries so that their useful life is extended and costly recycling can be deferred [31].

Community energy storage (CES) is one of the distributed energy storage devices (DESD) that has gained more and more interests [72]–[75]. Community energy storage system is located with the distribution transformer that supplies several residential homes, as shown in Figure 4.1. It can provide multiple supports to the power system such as buffering the distribution feeder from the impact of renewable sources (e.g. solar/wind power) and high power loads (EV/PHEV), serving as backup power during power outage, improve power quality, etc. Unlike utility scale energy storage, community energy storage can be located near the point of use, thereby easing local distribution issues, as shown in Figure 4.1. Combining many CES systems and controlling them together can produce energy capacity comparable to utility scale storage [74].

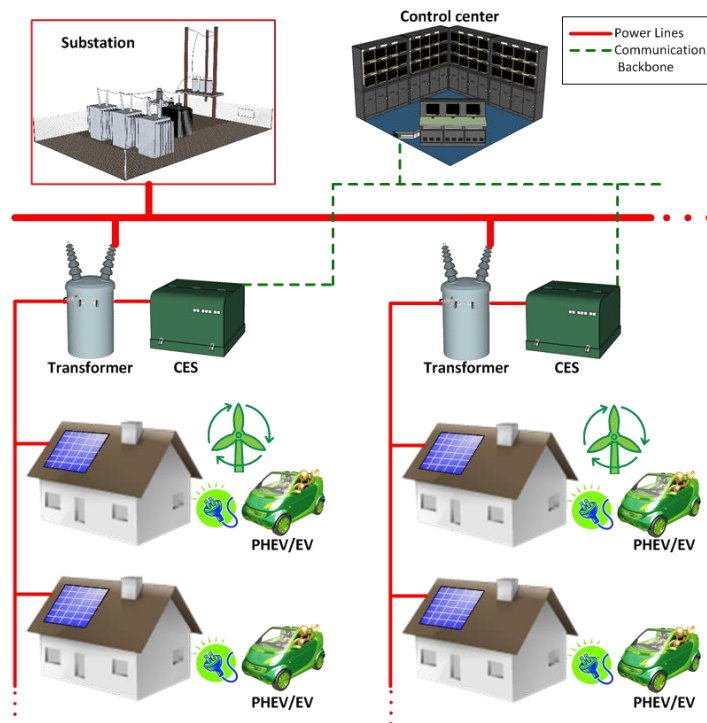


Figure 4.1 Overview of CES fleet layout

While it is worthwhile to study the system as a whole, the focus of this dissertation is the design of a single CES unit. Figure 4.2 gives the simplified block diagram of a CES unit. The goal is to design a bi-directional DC/AC converter that can be used to interface a bunch of dissimilar batteries with the grid. The design challenges and requirements are summarized here:

- (a) Dissimilar batteries come from different sources. They may have different chemistry, different terminal voltages (12V~48V for this project), different capacities, etc.
- (b) The grid voltage is 120V/240V (RMS) which is much higher than the battery voltage.
- (c) Since the batteries are different, the power flow from each battery needs to be independently controllable.
- (d) Modular design is preferable considering that there will be a number of batteries integrated in the system.

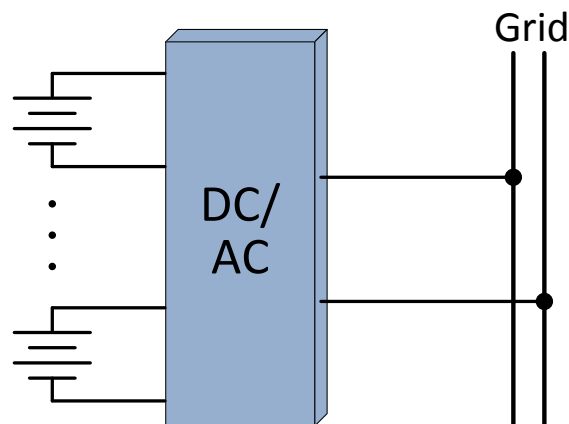


Figure 4.2 Simplified block diagram of a CES unit

Based on these identified challenges and requirements, the following sections will review all optional design solutions and determine the best one for this application. In section 4.1.1, the centralized design of energy storage integration and its drawbacks are discussed. To avoid these drawbacks, the modular design concept is introduced in section 4.1.2, and existing approaches and their limitations are reviewed. Section 4.2 reviewed the independent control strategies for cascaded H-Bridges. In section 4.3, the proposed modular design of cascaded H-Bridge is presented. Experiment results and conclusions are given in section 4.4, and section 4.5, respectively.

## **4.1 Approaches to Integrate Energy Storage into the Grid**

Although there are many ways to integrate energy storage into the grid, they can be categorized into two approaches, the centralized approach and the modular approach. The features of each approach are summarized in this section and the suitable approach for the proposed CES is determined.

### **4.1.1 Centralized Design of Energy Storage Integration and Its Drawbacks**

A simple way to integrate DC energy Storage (ES) is to have centralized energy storage and power conversion system, as given in Figure 4.3. The power conversion could be two-stage or one-stage, depending on the application. While centralized approach is straightforward, its disadvantages are also quite obvious.

On the energy storage side, to get sufficient voltage and capacity, a large number of energy storage cells need to be connected in series and/or in parallel. This is problematic because in practice it is not possible to manufacture two cells that are entirely identical. Any

small dispersion at the beginning could grow during operation. For example, the weakest cell (with lowest capacity) in a series-connected battery string will be depleted first during discharging. Further discharging the battery string will cause irreversible damage to the electrodes of the weakest cell and further reduce its capacity. As this cycle goes on, the weakest cell will eventually fail and cause the whole battery string to fail. To mitigate this problem, battery management system (BMS) is usually integrated with the battery pack [68]–[71]. Two types of functionalities can be provided by the BMS: protection and charge equalizing. A typical BMS will monitor the battery status including cell voltage, cell charge/discharge current and cell temperature. Based on the gathered battery information, the BMS should provide protections against over voltage, under voltage, over current, short circuit and over temperature. With these protections, cell failure is prevented. But the usable capacity of a battery string will be limited by the weakest cell. To solve this problem, charge equalizer can be integrated into the BMS to provide balancing of the cells [68]–[71]. Two types of balancing technology are available: passive balancing and active balancing. The passive balancing method uses passive components such as resistors to dissipate power and prevent the weak cells from being over charged. The obvious problem is the power loss on the passive components. Active balancing methods do not have this problem, but the system could be too complicated and costly.

On the power conversion side, centralized approach also has some issues. One is the lack of flexibility to expand system capacity which is pre-determined by the voltage and power ratings of the power converter. Another issue is that the single point of failure on either the centralized converter or the energy storage system renders the entire system un-operable.

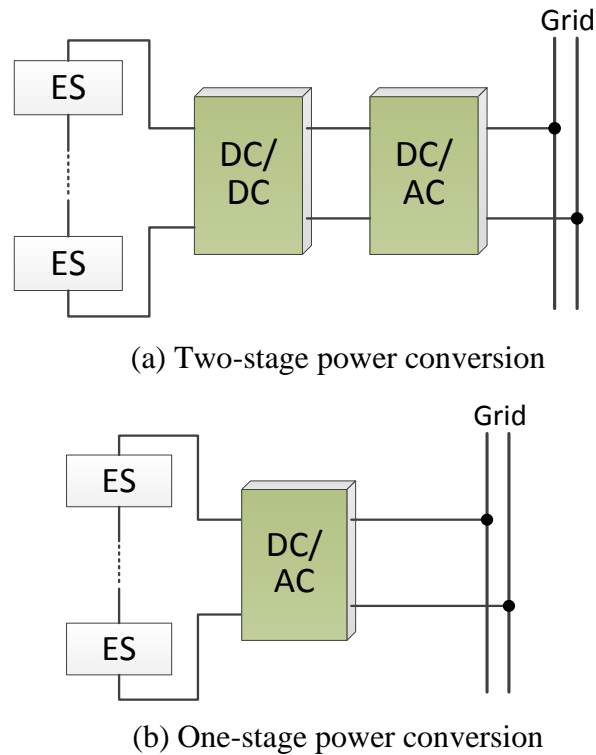


Figure 4.3 Grid integration of centralized energy storage system

In the case of the proposed community energy storage system, it is absolutely not acceptable to directly connect the batteries in series or in parallel because these batteries could be very different. So this centralized design approach is not suitable for the proposed CES unit.

#### 4.1.2 Modular Design of Energy Storage Integration

To solve aforementioned problems, the concept of modular design is introduced. Modular design is a design approach that separates a system into smaller modules that can be independently designed but function together as a whole [76], [77]. In terms of the energy storage system, the approach is to design a module that consists of energy storage device,

power convert and its controller. By assembling a number of the modules together, an energy storage system is formed and should function when connected to the grid.

In summary, the energy storage system with modular design requires that

- (1) Each module is self-contained;
- (2) Each module has its own controller that capable of autonomous operation;
- (3) Each module can be easily added or removed from the system (ideally be capable of Plug-and-Play operation);
- (4) The system should have fault tolerance so that the failed module can be isolated without jeopardizing the whole system.

There are two possible approaches to achieve modular design of the energy storage system, depending on the connection of the modules. One approach connects all modules in parallel, the other in series.

The system structures of the parallel-connected energy storage modules are given in Figure 4.4. Usually the voltage of each energy storage module is much lower than the grid voltage, so the power conversion needs to have high step-up voltage ratio. It is challenging to efficiently convert a low DC voltage directly to a high AC voltage, so two power stages are typically utilized. There are two configurations for this approach, as shown in Figure 4.4. With a DC bus, the modularization is achieved on the DC side [12], [15], [78]–[80]. The DC bus can also be used as an interface to integrate renewable energy sources. However, for this approach to integrate with the grid, a single DC/AC converter unit is needed, as shown in Figure 4.4(a). Therefore, the system as whole is not modular. Alternatively, each module

could have two-stage power conversion, as given in Figure 4.4(b), but it will result in a lower efficiency. The hardware cost is also increased due to doubled power conversion stages.

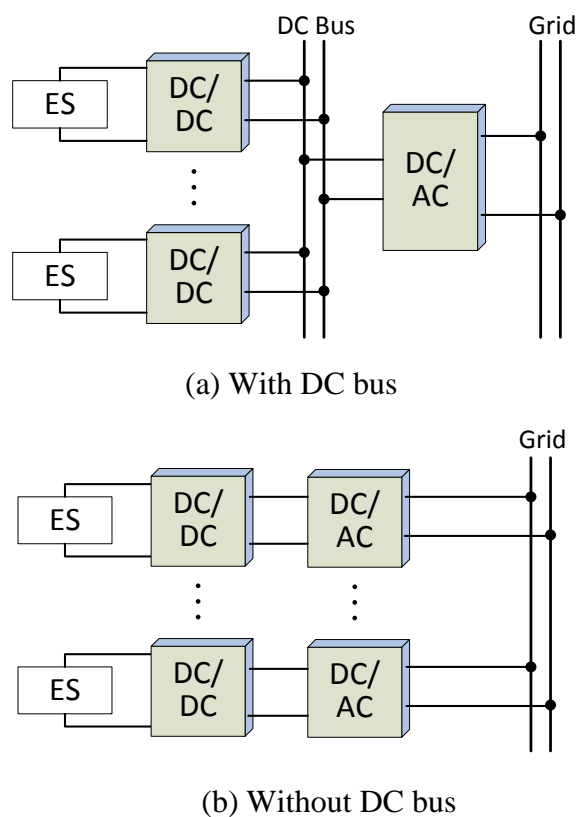
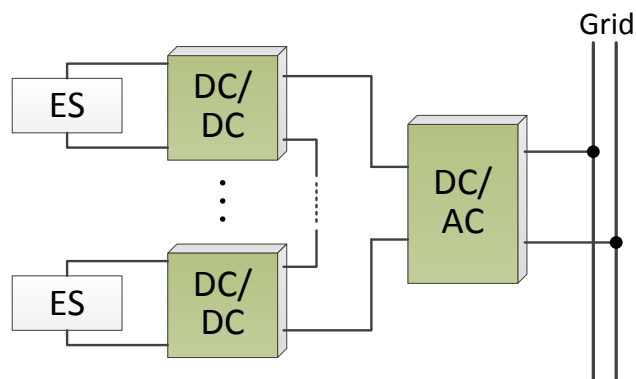
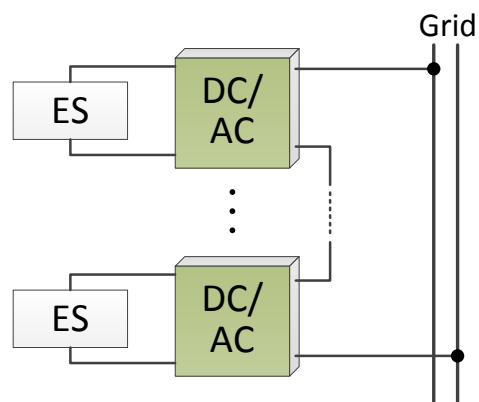


Figure 4.4 Grid integration of parallel connected energy storage modules

Another issue with this approach is that it is difficult to design a DC/DC converter that has high voltage boost ratio and wide range of input voltage [80], [81], which is required for the proposed CES unit. As identified in the beginning of this chapter, the battery voltage could vary from 12V to 48V. And the peak voltage on the grid side could be 339V (for 240 V grid).



(a) Two stage power conversion



(b) One stage power conversion

Figure 4.5 Grid integration of series connected energy storage modules

The system structures of the serial connected energy storage modules are given in Figure 4.5. In comparison with the parallel connection, the series connection has accumulated voltage so two stage power conversion as given in Figure 4.5(a) is not necessary. With one stage power conversion, as shown in Figure 4.5(b), this approach eliminates the centralized DC/AC converter and thus is totally modular and could have higher efficiency owing to the one stage power conversion. The cascaded DC/AC converters can also utilize some specially designed PWM techniques to cancel harmonics and increase equivalent switching frequency.

This approach has been widely used for rectifiers and integrating PV modules by using cascaded H-Bridge [82]–[84]. Other topologies other than the H-Bridge for the DC/AC converter may be used but they are rarely seen in literature. The challenge here is how to control each module independently, considering that they are serially linked together. This issue will be the focus of this chapter.

## 4.2 Control of Cascaded H-Bridge Converters-A Review

For cascaded H-Bridges, usually either the DC side or AC side voltage of each H-Bridge needs to be controlled independently [83]–[86]. However, as mentioned in section 4.1.2, the cascaded H-Bridges are physically linked together and it could be difficult to independently control each of them. This task has proven to be strictly related to stability problems [86] and will be investigated in this section.

A generic cascaded H-Bridge topology is given in Figure 4.6. Define the continuous switching function of the  $k^{th}$  H-Bridge to be  $M_k$ , there is:

$$v_{Hk} = M_k \cdot v_k, k = 1..n \quad (4.33)$$

where  $v_k$  is the DC link voltage and  $v_{Hk}$  is the AC output voltage of the  $k^{th}$  H-Bridge module.

On the AC side, there is

$$v_g = v_L + \sum_{k=1..n} v_{Hk} = L \cdot \frac{di_g}{dt} + \sum_{k=1..n} v_{Hk} \quad (4.34)$$

Combining (4.33) and (4.34), there are  $n$  switching functions to be solved, but there are  $n+1$  equations.

To understand this problem in a different way, we can see that the AC side current through each H-Bridge is the same, which is  $i_g$  as in Figure 4.6. And  $i_g$  needs to be controlled

(directly or indirectly) such that the sum of the H-Bridge output voltages can be determined, as shown in (4.34). However, if every H-Bridge is trying to control this current, they will fight with each other and cause stability issue.

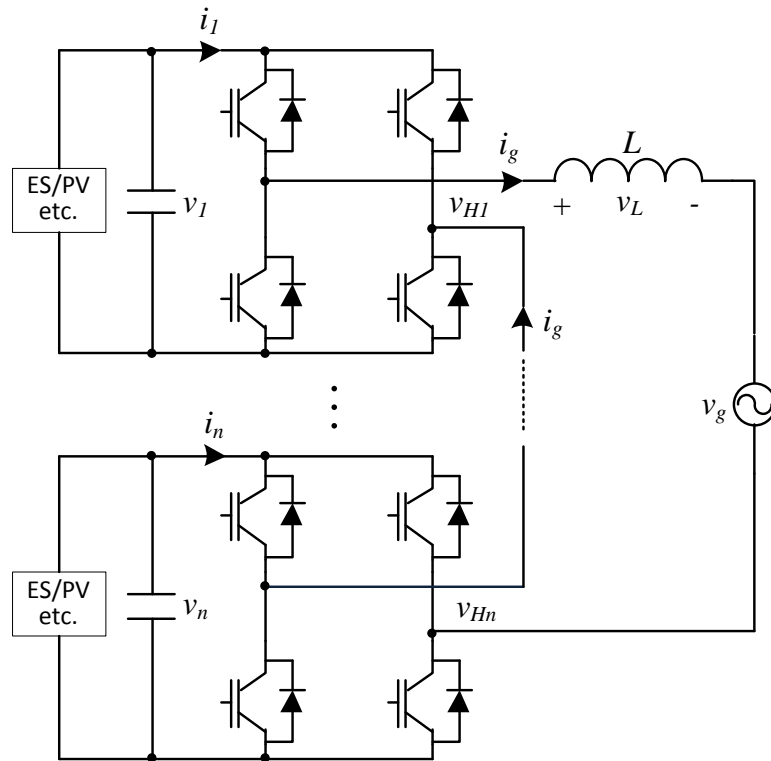


Figure 4.6 Generic Cascaded H-Bridge converter

To address this issue, several control strategies have been proposed [83]–[86]. In [83], a simple and straightforward method is proposed to have individual control of each H-Bridge, as given in Figure 4.7. The reference of grid current,  $i_g$ , could come from different sources (power command, DC side voltage command, etc.), depending on the application. By feeding back the grid current, the controller outputs the overall switching function,  $M_{total}$ . This

switching function is then distributed to each H-Bridge, with different gains. By assigning different gains, these H-Bridges will have different outputs. This control strategy is essentially considering the cascaded H-Bridges as one converter. There is a closed-loop control for the H-Bridges as a whole, but for each of them there is no closed-loop control. Therefore, it does not have the aforementioned stability issue. However, since there is no close loop control for each of the H-Bridges, the control accuracy is questionable. And obviously this control method has no modularity at all.

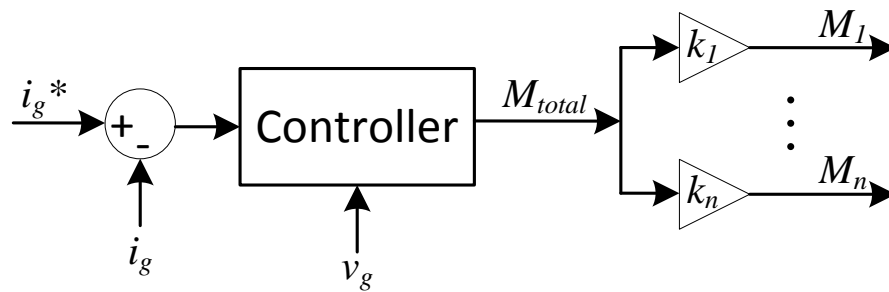


Figure 4.7 Control strategy for cascaded H-Bridge: method I

In [84] and [86], another control strategy is proposed, as given in Figure 4.8. The control target is the DC side voltages. For  $n$  H-Bridges, there are  $n$  closed control loops. But the first loop is still considering all the H-Bridges as a whole, by controlling the total DC side voltage of all H-Bridges. Moreover, the first controller needs the outputs of all the other controllers to get the switching function of the first H-Bridge. So all the controllers are tightly coupled together and this control method still lacks the sense of modularity. Additionally, this control method is not applicable to all cascaded H-Bridge applications. For example, if batteries are

used on the DC side of each H-Bridge, the DC side voltages cannot be the control target because they are determined by the batteries.

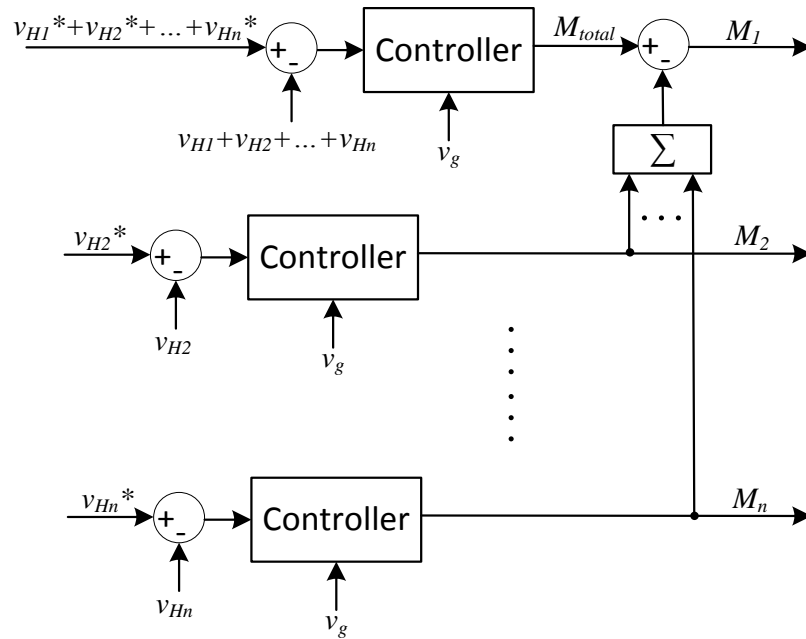


Figure 4.8 Control strategy for cascaded H-Bridge: method II

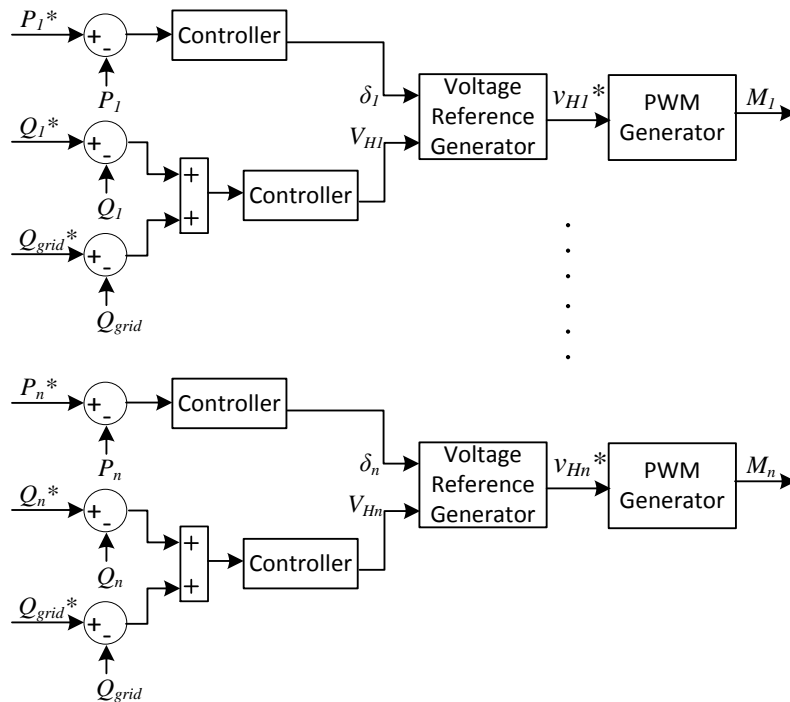


Figure 4.9 Control strategy for cascaded H-Bridge: method III

In [87], the authors presented a control strategy that has independent control of each H-Bridge and there is no communication between them. The diagram of the control strategy is given in Figure 4.9. The authors made an analogy between droop control for parallel and series connected inverters, and derived that for series connected inverters, the active power is determined by voltage phase angle and reactive power is determined by voltage amplitude. Based on this, the control strategy utilizes active and reactive power as feedback to get the voltage reference for each inverter. Note that the total reactive power command ( $Q_{grid}^*$  in Figure 4.9) is used to get the voltage reference, which means each of the inverters will try to control this variable. This is problematic and could cause stability issue, as analyzed in the beginning of this section. No theoretical analysis was given to prove the stability of this

control strategy, and the simulation results show severe oscillation during transition. Therefore, this control strategy is not considered as an option.

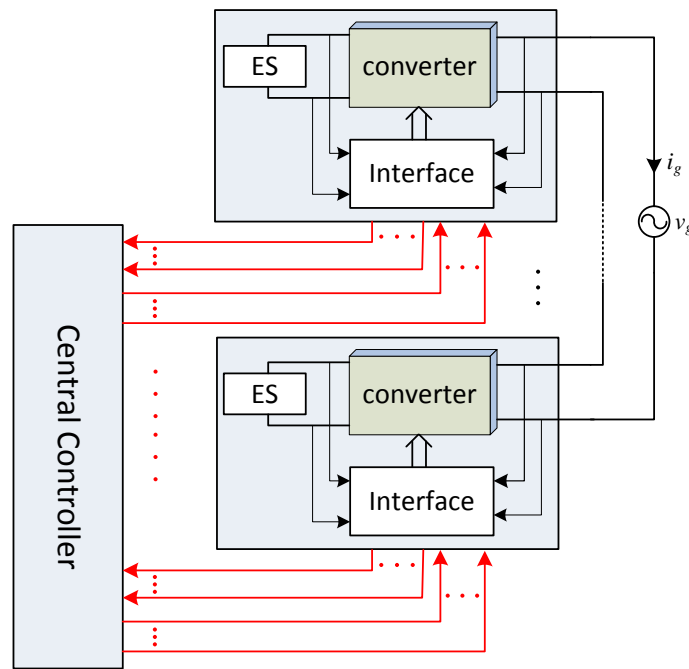


Figure 4.10 System block diagram with centralized control strategy

In summary, the existing control strategies (method I and II) can have individual control of each H-Bridge, but they all need a central controller to control all the H-Bridges. Figure 4.10 gives the block diagram of the system with centralized control strategy. By visually check this diagram, it is clear that there are too many communication lines between the central controller and all the modules. And the length of the lines could increase dramatically as the number of the modules is increasing. What makes it worse is that these lines are carrying some of the most critical signals to the converters, such as the PWM signal (digital) and the current/voltage feedbacks (analog). Anything goes wrong with these signals could

cause immediate failure of the converter. So the communication needs to be very reliable and very fast. Usually people just use one line for each signal because it is almost impossible to get high enough reliability and bandwidth to send all signals through communication protocols such as CAN bus. Even with one line for each signal, it is challenging to improve the noise immunity of the lines to reject the cross interference between these lines and the electromagnetic interference (EMI) from the power stages. Another issue is that all the converter modules are floating without sharing a common ground, which means the central controller needs to be isolated from each of the converters. This obviously will result in higher hardware cost and design complicity. Lastly, this centralized approach lacks the flexibility to easily expand the system with more modules.

In [88], a distributed control system with a central controller and multiple local controllers is proposed for the cascaded H-Bridge topology. The double loop control is implemented in the central controller to have overall control of the cascaded H-Bridges. The calculated modulation indices from the central controller are sent to each of the local controllers and are translated to PWM signal. The local controller also has a control strategy to do DC side voltage balancing. The analog signals are sent out through CAN bus. The modulation indices are sent out through serial peripheral interface (SPI) and the synchronization signal for PWM is sent out through dedicated line. By using the communication protocols (CAN and SPI), the number of communication lines is reduced. But the communication lines are still carrying critical signals like the modulation index and voltage feedback. The central controller may not directly control the switches (by generating

PWM signals), but it still heavily involved in the control of the H-Bridge. Overall, this is still a centralized control strategy.

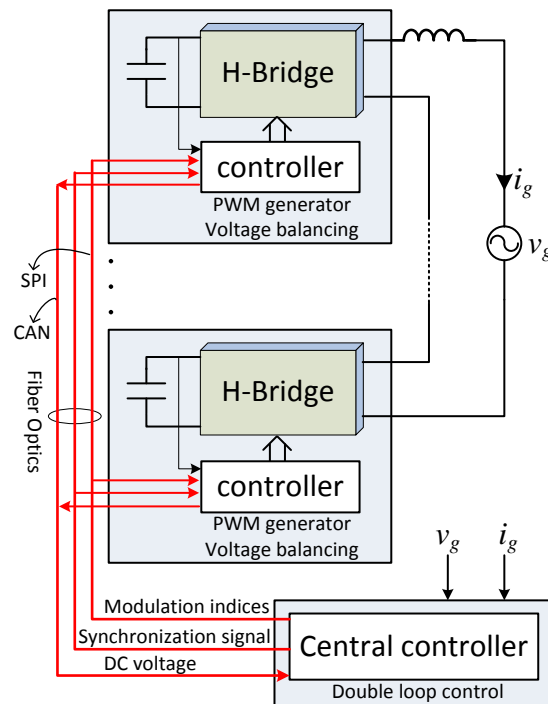


Figure 4.11 Distributed control system with central controller and local controllers

### 4.3 Modular Design of a Cascaded H-Bridge Converter for Energy Storage Integration

As reviewed in section 4.2, the centralized control has many drawbacks. The distributed control system proposed in [88] only mitigates some of the drawbacks and cannot really count as distributed control because of the presence of a central controller.

The goal is to completely eliminate the central controller. Figure 4.12 gives the diagram of this approach. It can be clearly seen that the structure of the system becomes much clearer and more modular. There are only two or three external input signals for each module, and among them only one signal ( $v_g$ ) is critical and time sensitive to the operation of the converter. The other input signals (power commands) belong to higher level (system level) control which means they are not the signals that directly control the switches of the converter. And thus they can be sent through slow communications by using different protocols such as CAN (for wired communication), Zigbee (for wireless communication), etc. Alternatively, these power commands can be generated locally by using proper control algorithms such as droop control. Moreover, because the local controller and the converter share the same ground, it is not necessary to isolate most of these signals. The grid voltage ( $v_g$ ) feedback does need isolation because it is fed to all modules which do not share a common ground. Another benefit is that this modular design makes it easier to add or remove modules from the system.

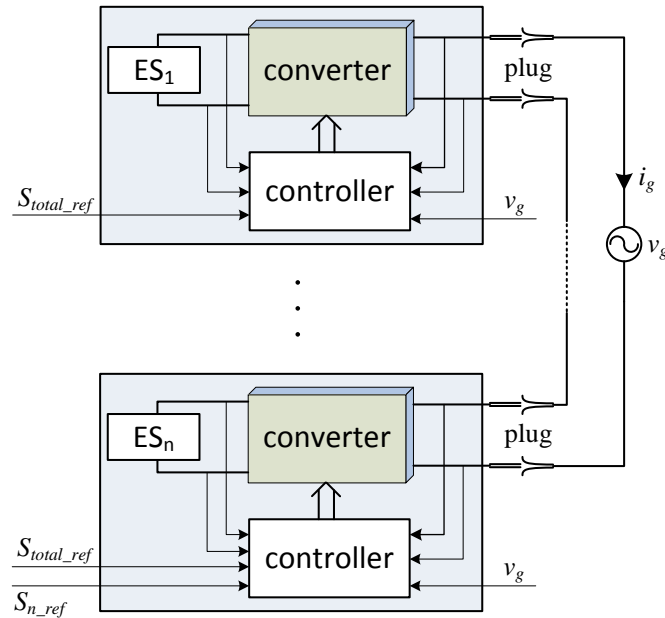


Figure 4.12 Proposed modular design approach with distributed controllers

Despite all the benefits of the proposed modular design, it is challenging to design the controllers since there is no direct communication between them and yet they need to work together to form a stable system. As reviewed in section 4.2 the existing control strategies (method I and method II) are all centralized control and thus cannot be used here. To solve this problem, a new control strategy is proposed, which will be presented in the following sections.

### 4.3.1 Proposed Control Strategy to Have Independent Control of Each Module

As discussed in previous sections, one requirement for the control strategy is that the power flow from each module can be independently controlled. The power flow from each module is determined by its output voltage and current, as given in (4.35). The variables in (4.35) are defined in Figure 4.13 ( $P_k(t)$  is the instantaneous power and  $M_k(t)$  is the switching

function of the  $k^{\text{th}}$  H-Bridge). Note that the output current for all modules are the same, which is also the output current of the system.

$$P_k(t) = v_{Hk}(t) \cdot i_{L_f}(t) = (M_k(t) \cdot V_{dck}) \cdot i_{L_f}(t), k = 1 \dots n \quad (4.35)$$

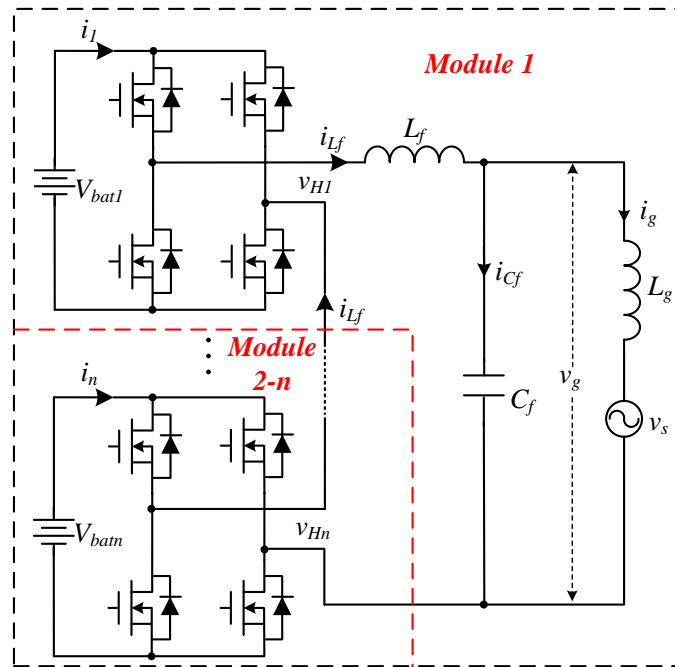


Figure 4.13 Power stage of the proposed system and its partitioning for controller design

It can be observed from this equation that there are  $n+1$  variables ( $v_{H1} \sim v_{Hn}$  and  $i_{L_f}$ ) to be controlled. However, one of the voltages is redundant variable that does not need to be controlled. As shown in (4.36), if we assume  $v_g$  and  $v_{L_f}$  are constant, we only need to control  $n-1$  voltages. The last voltage will be automatically determined by (4.36).

$$v_g + v_{L_f} = \sum_{k=1}^n v_{Hk} \quad (4.36)$$

Therefore, there are  $n$  variables (output voltages of  $n-1$  modules and  $i_{Lf}$ ) left to be controlled by  $n$  modules. It is then natural to use one module controls each of the variables. Figure 4.13 gives the partitioning of the system in terms of controller design. The first module will control the output current and the 2<sup>nd</sup> to  $n^{\text{th}}$  module will control their output voltages. Based on this partitioning, a control strategy is proposed, as given in Figure 4.14. Note that the first controller controls  $i_g$  instead of  $i_{Lf}$  because  $i_g$  is the current flowing to the grid. Considering that the capacitor current  $i_{Cf}$  is very small, the difference between controlling  $i_g$  and  $i_{Lf}$  is negligible. All controllers need grid voltage  $v_g$  to synchronize with the grid. The first controller needs total power command since it controls  $i_g$  which determines the total power (assuming  $v_g$  is constant). All the other controllers need their own power command and the total power command as well. The reason for these controllers to have total power command will be explained in section 4.3.3. Comparing with the existing control strategies as reviewed in section 4.2, the proposed control strategy eliminates interconnections between different modules and makes it possible to have modular design.

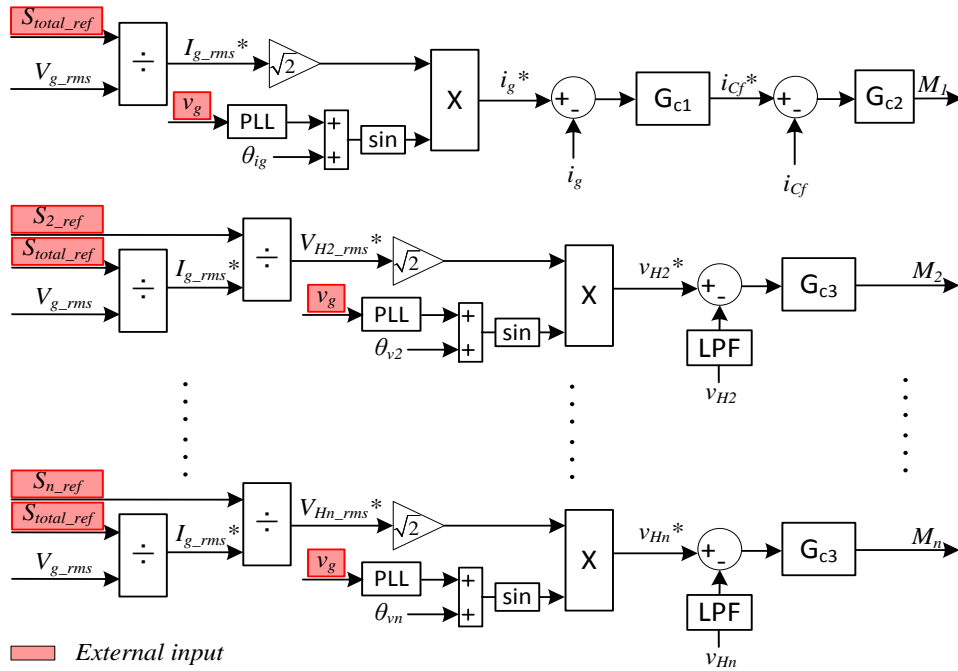


Figure 4.14 Proposed control strategy to have independent control of each module

There should not be any concerns regarding the control of the 2<sup>nd</sup> to the  $n^{\text{th}}$  modules because each of them is a standard H-Bridge which controls its own output voltage. However, the validity of using the first module to control  $i_g$  is not intuitively justified, considering that  $i_g$  is determined by the sum of the output voltages of all modules (with given  $L_f$  and assuming that  $v_g$  has constant amplitude). It is obvious that module 1 alone is not capable of controlling  $i_g$ . However, if the output voltages of the 2<sup>nd</sup> to the  $n^{\text{th}}$  modules are stable, they can be treated as constant voltage sources for a given operating condition. Then  $i_g$  is determined by the output voltage of the first module, as shown in (4.37).

$$L_f \cdot \frac{di_g(t)}{dt} = \sum_{k=1}^n v_{Hk}(t) - v_g(t) = v_{H1}(t) + \left( \sum_{k=2}^n v_{Hk} - v_g(t) \right) \quad (4.37)$$

Each module is able to output different power, but the power differences between different modules are not unlimited. To investigate this limit, first we need to derive the output power from each module. If we assume the capacitor current  $i_{Cf}$  is negligible, there is

$$S_k \doteq V_{Hk\_rms} \cdot I_{g\_rms}, k = 1..n \quad (4.38)$$

where  $S$  denotes the apparent power and the subscription  $rms$  denotes the RMS value of corresponding variable.

The total power is defined as

$$S_{total} = V_{g\_rms} \cdot I_{g\_rms} \quad (4.39)$$

Combining (4.38) and (4.39), there is

$$V_{Hk\_rms} = \frac{S_k}{S_{total}} \cdot V_{g\_rms}, k = 1..n \quad (4.40)$$

The peak value of  $v_{Hk}$  should not exceed the battery voltage

$$V_{Hk} = \frac{S_k}{S_{total}} \cdot V_g \leq V_{bat\_k}, k = 1..n \quad (4.41)$$

where  $V_{Hk}$  and  $V_g$  are the peak values of the module output voltage and grid voltage, respectively.

Then there is

$$\frac{S_k}{S_{total}} \leq \frac{V_{bat\_k}}{V_g}, k = 1..n \quad (4.42)$$

When the system level controller (e.g. SCADA system) gives power commands, this limitation needs to be taken into account to avoid saturating the H-Bridges.

### 4.3.2 Strategies for Active and Reactive Power Distribution

In Figure 4.14 the phase information comes from the grid voltage and a calculated angle ( $\theta_{ig}$  for the 1<sup>st</sup> module and  $\theta_{v2} \sim \theta_{vn}$  for the 2<sup>nd</sup> to  $n^{\text{th}}$  module). These angles determine how much active and reactive power the H-Bridge modules generate. Therefore, it is necessary to discuss how to determine these angles.

For the 1<sup>st</sup> module, the phase angle for  $i_g$  can be directly calculated from the active and reactive power commands

$$\theta_{ig} = \tan^{-1} \left( \frac{Q_{total\_ref}}{P_{total\_ref}} \right) \quad (4.43)$$

For the 2<sup>nd</sup> to  $n^{\text{th}}$  module, it is more complicated to determine the phase angles for their output voltages. First, the phasor diagram of the system quantities needs to be derived.

By analyzing the system in Figure 4.13, the relationships of the electric quantities in the system can be derived

$$\vec{I}_{Cf} = j\omega C_f \cdot \vec{V}_g \quad (4.44)$$

$$\vec{I}_{Lf} = \vec{I}_{Cf} + \vec{I}_g \quad (4.45)$$

$$\vec{V}_{Lf} = j\omega L_f \cdot \vec{I}_{Lf} \quad (4.46)$$

$$\vec{V}_{H\_total} = \vec{V}_{Lf} + \vec{V}_g \quad (4.47)$$

where  $V_{H\_total}$  is the sum of the output voltages of all H-Bridge modules.

Based on the derived equations, the phasor diagrams of the system at different operating conditions are given in Figure 4.15. All the vectors can be calculated based on known system parameters (phase angle of  $\vec{V}_g$  is assumed to be zero):

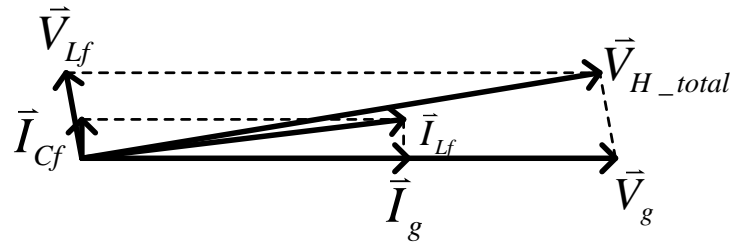
$$\vec{I}_g = I_g \angle \theta_{ig} = \sqrt{2} \cdot \frac{S_{total\_ref}}{V_{g\_rms}} \angle \tan^{-1} \left( \frac{Q_{total\_ref}}{P_{total\_ref}} \right) \quad (4.48)$$

$$\vec{I}_{Cf} = I_{Cf} \angle \theta_{ic} = j\omega C_f \cdot \vec{V}_g = \omega C_f \angle \frac{\pi}{2} \cdot V_g \angle 0 = \omega C_f V_g \angle \frac{\pi}{2} \quad (4.49)$$

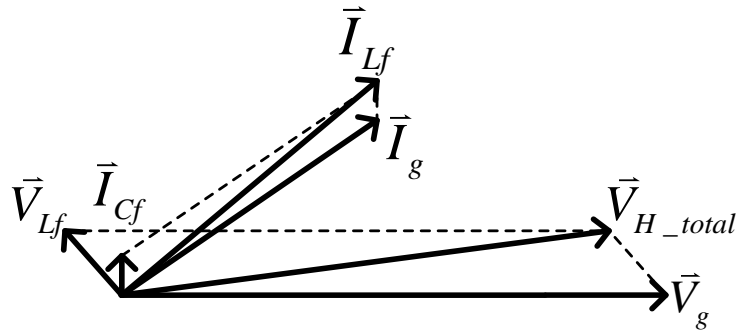
$$\begin{aligned} \vec{I}_{L_f} &= I_{L_f} \angle \theta_{iL} = \vec{I}_{Cf} + \vec{I}_g \\ &= \sqrt{(I_g + I_{Cf} \cdot \cos(\theta_{ic} - \theta_{ig}))^2 + (I_{Cf} \cdot \sin(\theta_{ic} - \theta_{ig}))^2} \angle \left( \theta_{ig} + \tan^{-1} \frac{I_{Cf} \cdot \sin(\theta_{ic} - \theta_{ig})}{I_g + I_{Cf} \cdot \cos(\theta_{ic} - \theta_{ig})} \right) \end{aligned} \quad (4.50)$$

$$\vec{V}_{L_f} = V_{L_f} \angle \theta_{vL} = j\omega L_f \cdot \vec{I}_{L_f} = \omega L_f \angle \frac{\pi}{2} \cdot I_{L_f} \angle \theta_{iL} = \omega L_f I_{L_f} \angle \left( \theta_{iL} + \frac{\pi}{2} \right) \quad (4.51)$$

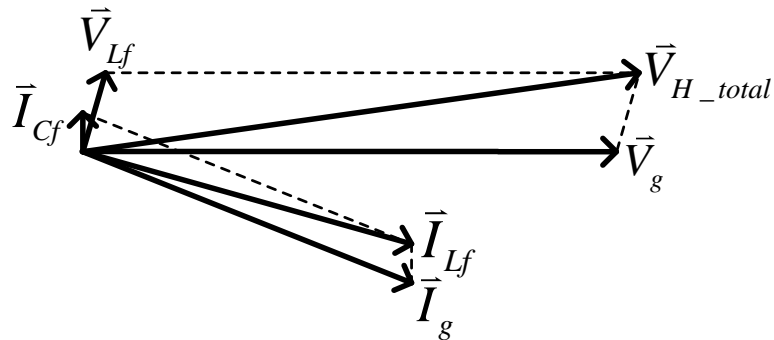
$$\begin{aligned} \vec{V}_{H\_total} &= V_{H\_total} \angle \theta_{vH} = \vec{V}_{L_f} + \vec{V}_g \\ &= \sqrt{(V_g + V_{L_f} \cdot \cos \theta_{vL})^2 + (V_{L_f} \cdot \sin \theta_{vL})^2} \angle \tan^{-1} \frac{V_{L_f} \cdot \sin \theta_{vL}}{V_g + V_{L_f} \cdot \cos \theta_{vL}} \end{aligned} \quad (4.52)$$



(a) No reactive power to the grid

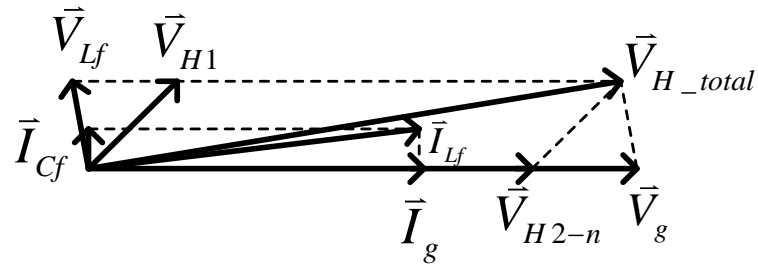


(b) Positive reactive power to the grid

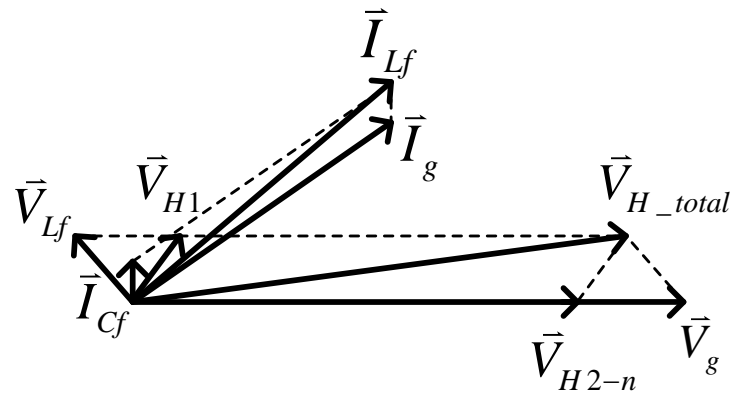


(c) Negative reactive power to the grid

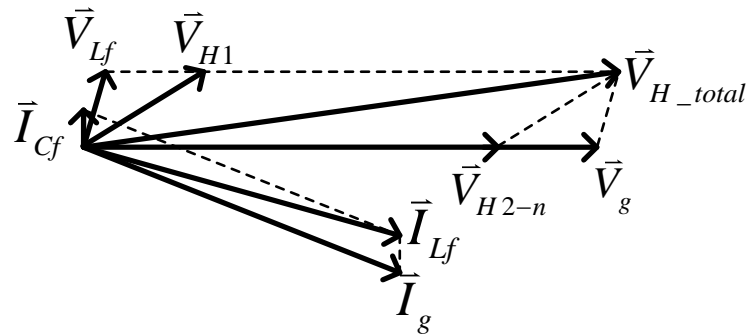
Figure 4.15 Phasor diagram of the system quantities



(a) No reactive power to the grid



(b) Positive reactive power to the grid



(c) Negative reactive power to the grid

Figure 4.16 Phasor diagram of the system with  $v_{H2} \sim v_{Hn}$  in phase with  $v_g$ 

Now we have the phase angle of the total voltage of all H-Bridge modules ( $v_{H\_total}$ ), the next question is how to determine the phase angles of the 2<sup>nd</sup> to  $n^{\text{th}}$  modules ( $\theta_{v2} \sim \theta_{vn}$  in Figure 4.14). The first option is to have all these angles equal to  $\theta_{vH}$  as calculated in (4.52).

With this, the amplitude of the output voltage from each H-Bridge is minimized for a certain  $V_{H\_total}$ . However, to implement this each controller needs to calculate  $\theta_{vH}$  in real time, which could substantially increase the computational burden of the digital controllers. Another option is to simply neglect  $\theta_{vH}$  by letting  $v_{H2} \sim v_{Hn}$  to be in phase with  $v_g$ . Considering that  $V_{Lf}$  is much smaller than  $V_g$ ,  $\theta_{vH}$  is very small and thus this simplification will not make substantial difference. With this simplification, the reactive power consumed by the LC filter will be provided by the first module. The phasor diagram of the system is given in Figure 4.16, where

$$\vec{V}_{H2-n} = \sum_{k=2}^n \vec{V}_{Hk} \quad (4.53)$$

It is worthwhile to mention that with the previously discussed configuration, the percentage of active and reactive power from each module with respect to the total active and reactive power will be the same. For example, if one module outputs 20% of total active power, it will also output 20% of the total reactive power. However, there could be a need to distribute active and reactive power differently between modules. From (4.40) we know that the percentage of the output power from each module is determined by its output voltage. One scenario is that one module has a high capacity battery so it can output higher active power. But the battery voltage is low which limits the power it can output. On the other hand, the other module has a low capacity battery with higher voltage. Note that the output power from each module is the apparent power and battery capacity is account for how much active power it can provide. Therefore, we can keep the percentage of apparent power to be the same for each module but let the strong battery provide more active power and the weak battery provide more reactive power. Figure 4.17 gives an example of these two different

ways to distribute active and reactive power among the modules. The upper diagram shows the situation when both the active and reactive power are evenly distributed between the 2<sup>nd</sup> and 3<sup>rd</sup> module. For the lower diagram, the amplitude of the output voltage of the 2<sup>nd</sup> module remains the same but this voltage is in phase with the grid current. Therefore, the 2<sup>nd</sup> module will output more active power and zero reactive power to the grid. To maintain the same total output voltage ( $\vec{V}_{H2-3}$  in Figure 4.17) of these two modules, the 3<sup>rd</sup> module needs to output a higher voltage with a larger phase shift with respect to grid current. Therefore, the 3<sup>rd</sup> module will output higher reactive power but lower active power to the grid. One disadvantage of this approach is that the VA ratings of all the modules will be higher, as clearly illustrated in Figure 4.17 ( $v_{H1}$  remains the same,  $v_{H2}$  becomes higher).

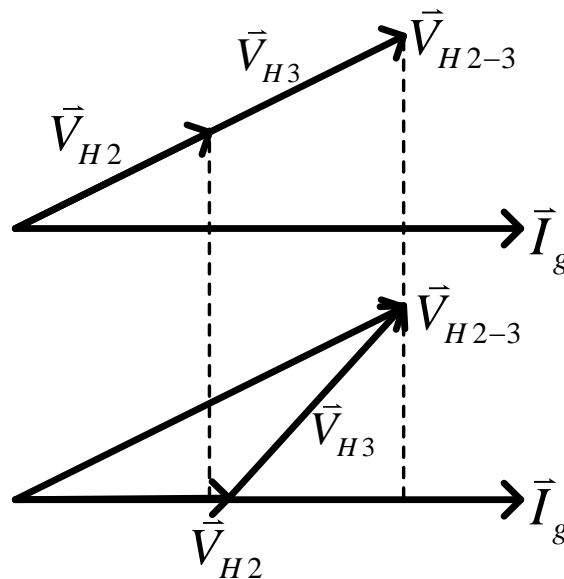


Figure 4.17 Example of two different ways to distribute active and reactive power among modules

With this strategy, the phase angle of the voltage references for the 2<sup>nd</sup> to  $n^{\text{th}}$  modules will be

$$\theta_{vk} = \theta_{ig} - \tan^{-1} \left( \frac{Q_{k\_ref}}{P_{k\_ref}} \right) = \tan^{-1} \left( \frac{Q_{total\_ref}}{P_{total\_ref}} \right) - \tan^{-1} \left( \frac{Q_{k\_ref}}{P_{k\_ref}} \right), k = 2..n \quad (4.54)$$

To verify the effectiveness of these two power distribution strategies, a system with 3 modules is simulated with the power commands given in Table 4.1. Initially, power distribution strategy I is applied, with the ratio of active to reactive power remains the same for all the modules. At a certain time, the power distribution strategy II is applied with module 2 outputs more active power but no reactive power, while module 3 outputs less active power but more reactive power. The total active and reactive power remains the same. The simulation result is given in Figure 4.18. Before 0.2 second, strategy I is applied. It can be seen that the output voltages of module 2 and 3 ( $v_{H2}$  and  $v_{H3}$ ) are in phase with the grid voltage ( $v_g$ ). The first module needs to provide reactive power for the LC filter so its output voltage has a small phase shift with respect to the grid voltage, but it is hard to observe. After 0.2 second, module 2 will only output active power so its output voltage ( $v_{H2}$ ) is in phase with grid current ( $i_g$ ). The amplitude of  $v_{H2}$  remains the same because the apparent power for module 2 does not change. Module 3 needs to output more reactive power, so its output voltage ( $v_{H3}$ ) has a larger phase shift with respect to the grid current. The amplitude of  $v_{H3}$  is higher because module 3 generates more apparent power.

Table 4.1 Power commands for the simulation

	Strategy I		Strategy II	
	$P_{ref}$ (W)	$Q_{ref}$ (var)	$P_{ref}$ (W)	$Q_{ref}$ (var)
Module 1	240	180	240	180
Module 2	400	300	500	0
Module 3	500	375	400	675
Total Power	1140	855	1140	855

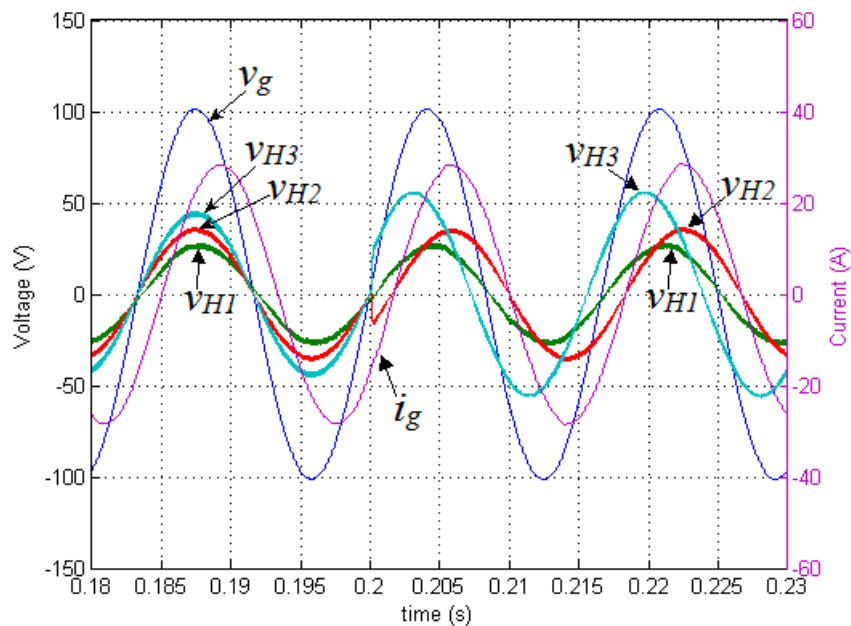


Figure 4.18 Simulation result for two different power distribution strategies

In the next two sections the modeling and analysis of the proposed controllers (current controller for the first module and voltage controller for the other modules) will be presented. Since the proper operation of the first module (with current controller) relies on stable output voltages of the 2<sup>nd</sup> to n<sup>th</sup> modules (with voltage controller), the voltage controller will be discussed first.

### 4.3.3 Modeling and Analysis of the Voltage Controller

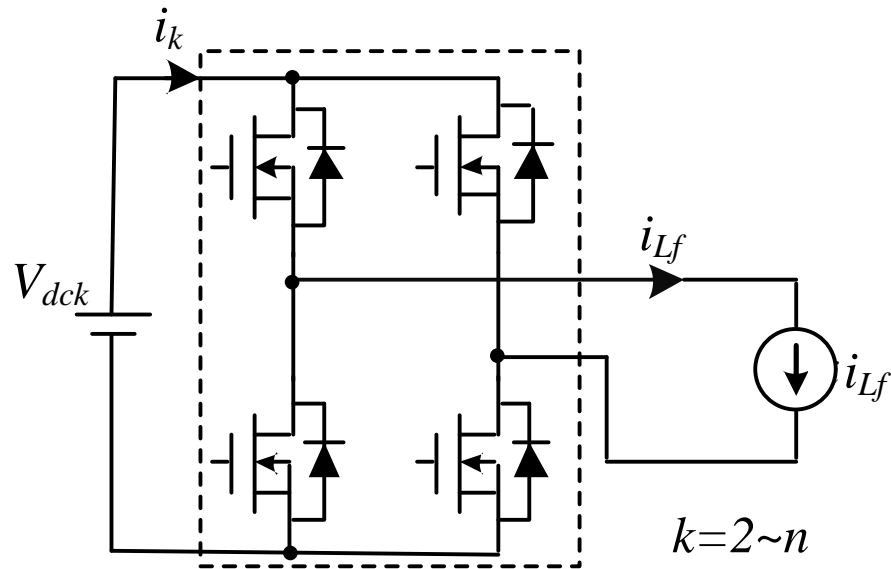


Figure 4.19 Equivalent circuit of the 2<sup>nd</sup> to n<sup>th</sup> modules

As discussed earlier, the output voltage of the 2<sup>nd</sup> to n<sup>th</sup> modules need to be stable both in steady state and during transient operation, so that the interference between these modules and the first module will be minimized and the first module will be able to control the output current of the system. From the partitioning of the system as given in Figure 4.13 it can be seen that the 2<sup>nd</sup> to n<sup>th</sup> modules have the same simple topology which consists of a battery pack and an H-Bridge. The equivalent circuit of these modules is given in Figure 4.19. The battery is modeled as a constant voltage source for simplicity. The output current is the current going through all the modules and is controlled by the first module, so it can be modeled as a current source. The only dis-continuity in this circuit comes from the H-Bridge. By averaging the switches, this dis-continuity can be eliminated. The average model of the

H-Bridge is given in Figure 4.20, where  $d$  is the duty ratio of the PWM that controls the H-Bridge.

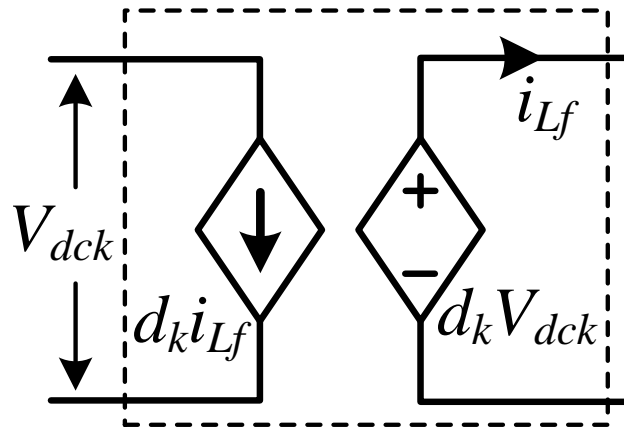


Figure 4.20 Average model of the H-Bridge

With the switches being averaged, the model of the whole module can be easily derived, as given in Figure 4.21. We are only interested in the right part of the circuit. Since the battery is considered as a constant voltage source ( $V_{dck}$ ), the right part of this circuit is linear. Therefore, the small signal model can be directly derived, as given in Figure 4.22. It is obvious that this is a very simple circuit and the output voltage of the module, which is what we are interested in, is simply a controlled voltage source. With this circuit we can assume that it will output whatever voltage that is within the output voltage limitation as commanded. Therefore, the challenge becomes how to get the desired voltage reference for the module.

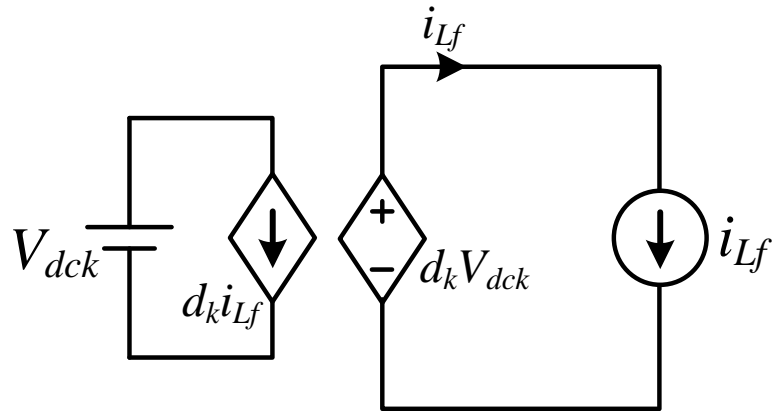


Figure 4.21 Average model of the 2<sup>nd</sup> to n<sup>th</sup> module

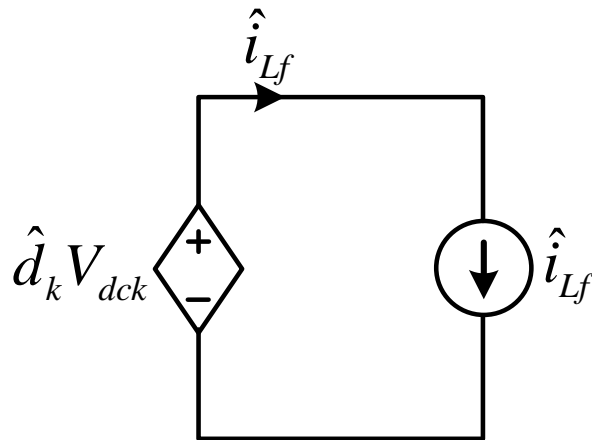


Figure 4.22 Small signal model of the circuit that is of interest for 2<sup>nd</sup> to n<sup>th</sup> module

For each module, the input reference signal is the power reference ( $S_{k\_ref}$ ) and it can be easily translated into voltage reference ( $V_{Hk\_rms}^*$ )

$$V_{Hk\_rms}^* = \frac{S_{k\_ref}}{I_{Lf\_rms}} \doteq \frac{S_{k\_ref}}{I_{g\_rms}} \quad (4.55)$$

where  $I_{L_f\_rms}$  and  $I_{g\_rms}$  stand for the RMS value of the inductor current  $i_{L_f}$  and the grid current  $i_g$ , respectively. Note that in (4.55)  $I_{g\_rms}$  is used as an approximation of  $I_{L_f\_rms}$ , considering that the capacitor current is low. The error caused by this approximation can be easily compensated given the amplitude and frequency of grid voltage and the capacitor value. The question now becomes how to get  $I_{g\_rms}$ . The grid current  $i_g$  is the current that goes through every H-Bridge. This is the variable that couples all the H-Bridges and makes it difficult to modularize the controller. If the actual real-time grid current, which is controlled by the first module, is used to get the voltage reference, then any fluctuations or oscillations on the grid current during transitions will be directly reflected in the voltage reference as shown in (4.55). As a result, the output voltages of the 2<sup>nd</sup> to  $n^{\text{th}}$  modules will also have fluctuations and oscillations, which in return affect the grid current. This interaction could potentially cause stability issue. To solve this problem, the proposed control strategy uses the calculated grid current to get voltage reference, as shown in Figure 4.23 and (4.56), where  $S_{total\_ref}$  is total power command.

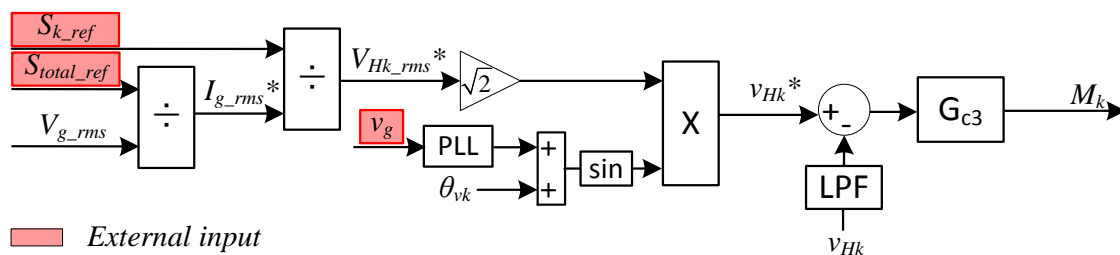


Figure 4.23 Proposed controller for the 2<sup>nd</sup> to  $n^{\text{th}}$  module

$$V_{Hk\_rms}^* \doteq \frac{S_{k\_ref}}{I_{g\_rms}^*} = \frac{S_{k\_ref}}{S_{total\_ref} / V_{g\_rms}} = \frac{S_{k\_ref}}{S_{total\_ref}} \cdot V_{g\_rms} \quad (4.56)$$

It is clear that now the voltage reference is not directly affected by the grid current. Also, the grid voltage can be seen as a constant voltage, so the voltage references for the 2<sup>nd</sup> to  $n^{\text{th}}$  modules are linear functions of the power commands. This means that when the power commands change, the voltage references change immediately without any transition. This ensures that the 2<sup>nd</sup> to  $n^{\text{th}}$  modules are always output the “correct” voltage without interacting with the first module. By doing this, the coupling between all the modules is minimized to ensure a stable system with independent controls.

Since the power stage is a zero order system as shown in Figure 4.22, it is very easy to design the voltage control loop. The compensator ( $G_{c3}$  in Figure 4.23) can simply be a proportional gain. Proportional-resonant control can also be used to improve the steady state error at fundamental frequency [89], [90]. It is also worth to mention that since there is no filter for the output voltage, a digital low pass filter (LPF) is implemented in the controller to filter the voltage feedback, as shown in Figure 4.23.

#### 4.3.4 Modeling and Analysis of the Current Controller

The current controller is for the first module, which consists of a battery pack, an H-Bridge and the LC filter, according to the system partitioning as given in Figure 4.13. The equivalent circuit of this module is given in Figure 4.24. As presented in the previous section, all the other modules behave like controlled voltage source, therefore, they are lumped together and modeled as a voltage source ( $v_H$  in Figure 4.24).

The average model of the H-Bridge has been given in Figure 4.20. With the H-Bridge being averaged, the average model of this module can be easily derived, as given in Figure 4.25, where  $R_{L_f}$  and  $R_{C_f}$  are the ESR of the inductor ( $L_f$ ) and capacitor ( $C_f$ ) and  $R_{L_g}$  is the resistive impedance of the grid. We are only interested in the right part of the circuit, which is linear considering that the battery voltage is assumed to be constant. Therefore, the small signal model can be directly derived, as given in Figure 4.26.

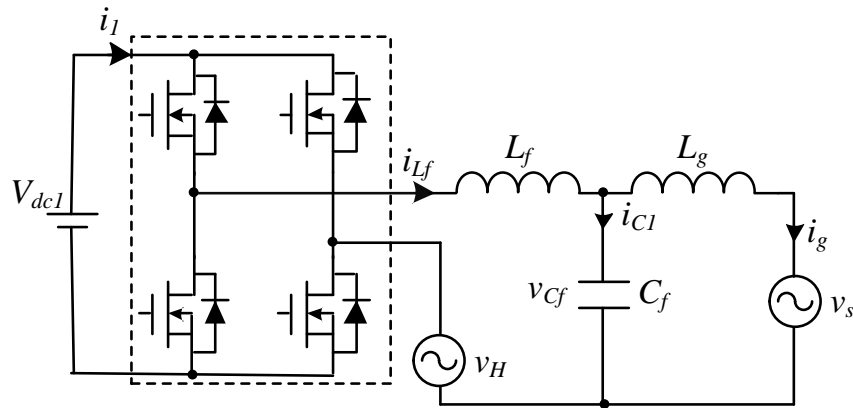


Figure 4.24 Equivalent circuit of the first module

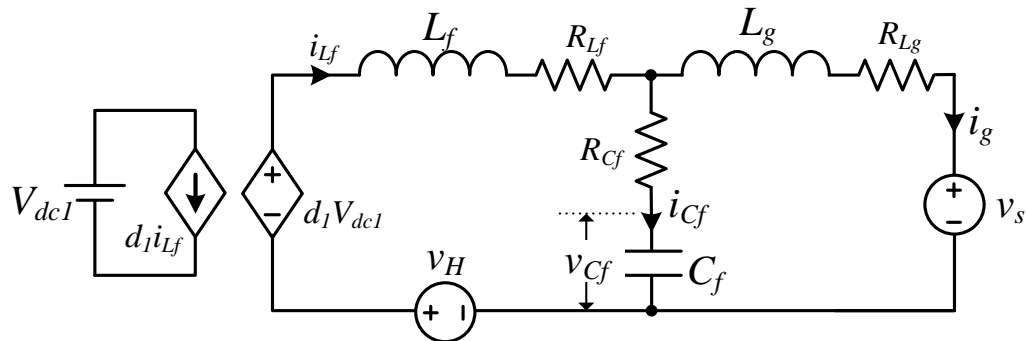


Figure 4.25 Average model of the first module

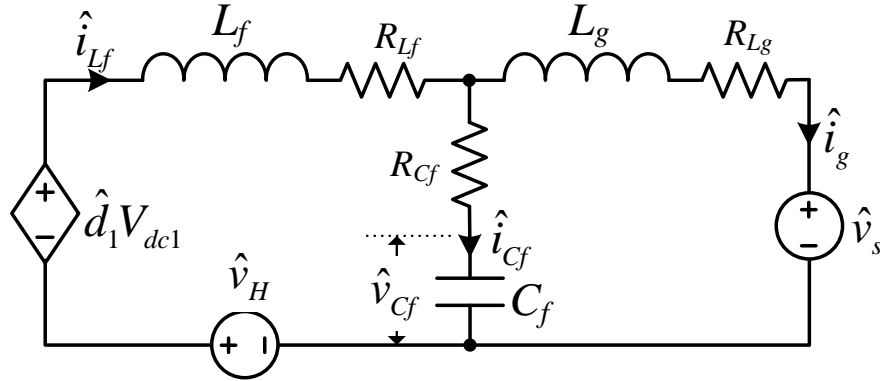


Figure 4.26 Small signal model of the circuit that is of interest for the first module

The circuit in Figure 4.26 can be described by the derivative equations as followed

$$L_f \cdot \frac{d\hat{i}_{L_f}(t)}{dt} = V_{dc} \cdot \hat{d}_1(t) - \hat{v}_{C_f}(t) + \hat{v}_H(t) - R_{L_f} \cdot \hat{i}_{L_f}(t) - R_{C_f} \cdot \hat{i}_{C_f}(t) \quad (4.57)$$

$$C_f \cdot \frac{d\hat{v}_{C_f}(t)}{dt} = \hat{i}_{C_f}(t) \quad (4.58)$$

$$L_g \cdot \frac{d\hat{i}_g(t)}{dt} = \hat{v}_{C_f}(t) - \hat{v}_s(t) + R_{C_f} \cdot \hat{i}_{C_f}(t) - R_{L_g} \cdot \hat{i}_g(t) \quad (4.59)$$

$$\hat{i}_{L_f}(t) = \hat{i}_{C_f}(t) + \hat{i}_g(t) \quad (4.60)$$

Write the equations in  $s$ -domain, there is

$$sL_f \cdot \hat{i}_{L_f}(s) = V_{dc} \cdot \hat{d}_1(s) - \hat{v}_{C_f}(s) + \hat{v}_H(s) - R_{L_f} \cdot \hat{i}_{L_f}(s) - R_{C_f} \cdot \hat{i}_{C_f}(s) \quad (4.61)$$

$$sC_f \cdot \hat{v}_{C_f}(s) = \hat{i}_{C_f}(s) \quad (4.62)$$

$$sL_g \cdot \hat{i}_g(s) = \hat{v}_{C_f}(s) - \hat{v}_s(s) + R_{C_f} \cdot \hat{i}_{C_f}(s) - R_{L_g} \cdot \hat{i}_g(s) \quad (4.63)$$

$$\hat{i}_{L_f}(s) = \hat{i}_{C_f}(s) + \hat{i}_g(s) \quad (4.64)$$

By evaluating equations (4.61)~(4.64), multiple transfer functions can be derived:

(a) Control to capacitor current transfer function

$$G_{id}(s) = \left. \frac{\hat{i}_{C_f}(s)}{\hat{d}_1(s)} \right|_{\hat{v}_S(s)=\hat{v}_H(s)=0} = V_{dc1} \cdot \frac{s^2 L_g C_f + s C_f R_{L_g}}{DEN} \quad (4.65)$$

where

$$\begin{aligned} DEN = & s^3 L_f L_g C_f + s^2 (L_f C_f R_{C_f} + L_f C_f R_{L_g} + L_g C_f R_{L_f} + L_g C_f R_{C_f}) + \\ & s (L_f + L_g + C_f R_{C_f} R_{L_g} + C_f R_{C_f} R_{L_f} + C_f R_{L_f} R_{L_g}) + R_{L_f} + R_{L_g} \end{aligned} \quad (4.66)$$

(b) Capacitor current to grid current transfer function

$$G_{ii}(s) = \left. \frac{\hat{i}_g(s)}{\hat{i}_{C_f}(s)} \right|_{\hat{v}_S(s)=\hat{v}_H(s)=0} = \frac{s C_f R_{C_f} + 1}{s^2 L_g C_f + s C_f R_{L_g}} \quad (4.67)$$

(c) Control to output (grid current  $i_g$ ) transfer function

$$G_{od}(s) = \left. \frac{\hat{i}_g(s)}{\hat{d}_1(s)} \right|_{\hat{v}_S(s)=\hat{v}_H(s)=0} = G_{id}(s) \cdot G_{ii}(s) = V_{dc1} \cdot \frac{s C_f R_{C_f} + 1}{DEN} \quad (4.68)$$

where  $DEN$  is defined in (4.66).

(d) Output admittance ( $v_H$  and  $v_S$  to grid current  $i_g$ ) transfer function

$$Y_1(s) = \left. \frac{\hat{i}_g(s)}{\hat{v}_H(s)} \right|_{\hat{v}_S(s)=\hat{d}_1(s)=0} = \frac{s C_f R_{C_f} + 1}{DEN} \quad (4.69)$$

$$-Y_2(s) = \left. \frac{\hat{i}_g(s)}{\hat{v}_S(s)} \right|_{\hat{v}_H(s)=\hat{d}_1(s)=0} = -\frac{s^2 L_f C_f + s(C_f R_{C_f} + C_f R_{L_f}) + 1}{DEN} \quad (4.70)$$

where  $DEN$  is defined in (4.66).

Table 4.2 Parameters of the system for controller design

Parameter	Value
Battery voltage ( $V_{dc1}$ )	12~48 V
Inductor ( $L_f$ )	745 $\mu$ H
Capacitor ( $C_f$ )	60 $\mu$ F
ESR of $L_f$ ( $R_{Lf}$ )	28 m $\Omega$
ESR of $C_f$ ( $R_{Cf}$ )	1.6 m $\Omega$
Grid inductance ( $L_g$ )	0.2~2 mH
Grid resistance ( $R_{Lg}$ )	0.5 $\omega L_g$ ( $\omega=120\pi$ is grid frequency)
H-Bridge switching frequency ( $f_{sw}$ )	20 kHz

Among these transfer functions, the control to output transfer function ( $G_{od}$ ) is of great interest because it reveals the open loop response of the system. It is worthwhile to examine the bode plot of this transfer function. To get the bode plot, some parameters of the system need to be determined, as given in Table 4.2. The procedure to determine these parameters will be given in later section. Note that the equivalent inductance of the distribution line is assumed to vary between 0.2 mH and 2 mH, which represent the values for stiff and weak grid, respectively. The equivalent resistance of the distribution line is assumed to be 50% of its inductive impedance. The battery voltage could vary from 12V to 48V. Since the battery voltage is simply a gain in the transfer functions, the controller design can be done based on one battery voltage and the control parameters can be easily adjusted for different battery voltages. The battery voltage will be set to 24V for the following analysis.

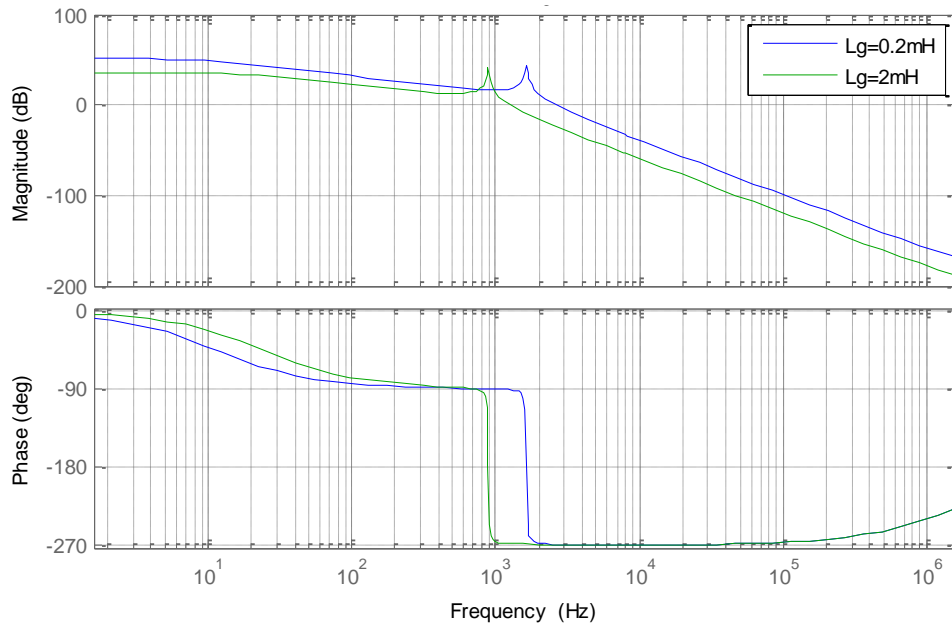


Figure 4.27 Bode plot of the control to output transfer function of the system

With the given parameters, the bode plot of the control to output transfer function is given in Figure 4.27. Two conditions with highest and lowest grid impedances are plotted in the same figure. The resonant peak is caused by the resonance between the LC filter ( $L_f$  and  $C_f$ ) of the system and the grid inductance ( $L_g$ ). At resonant frequency, the gain is high and the phase rolls off very quickly. This could cause stability issue if the controller is not carefully designed to take care of this effect. Usually, the controller is designed to have a bandwidth that is higher than the resonant frequency such that this resonant peak is damped and the phase roll-off is compensated to get enough gain and phase margin. However, the traditional single loop control usually needs to have low loop gain to ensure enough phase margin and thus system stability, as analyzed in [91]. As a result, it is almost impossible to design the controller to have a bandwidth higher than the filter resonant frequency. If the controller

bandwidth is lower than the filter resonant frequency, the resonant peak could cause the loop gain to come back above 0dB again with the phase rolling off below  $-180^\circ$ , which results in an unstable system.

To solve the problems of the single loop control, the double loop control is introduced. The additional inner loop can provide damping of the inverter output filter resonance and thus improve system stability and speed up the dynamic response [91], [92]. For a typical H-Bridge with output LC or LCL filter as shown in Figure 4.24, there are two options for the feedback signal of the inner loop, the inductor current  $i_{Lf}$  or the capacitor current  $i_{Cf}$ . However, it has been analyzed in [92] that with capacitor current feedback the system is less sensitive to load current distortion. On the other hand, with inductor current feedback the system stability could get worse (for voltage source inverter with LCL filter).

Another factor that needs to be taken into account when designing the controller is the time delay caused by the digital controller (conversion time of the ADC, computation time, etc.). This delay is modeled as a first order transfer function, as given in (4.71), where  $T_s$  is the switching period.

$$G_d(s) = \frac{1}{2T_s \cdot s + 1} \quad (4.71)$$

To understand the effect of this delay on controller design, the bode plot is given in Figure 4.28. The magnitude is unity for most of the low frequency range, so there is almost no effect on the controller design in terms of loop gain. However, the phase roll-off will reduce the system phase margin and make an otherwise stable system become unstable. Therefore, this time delay must be included when designing the controller.

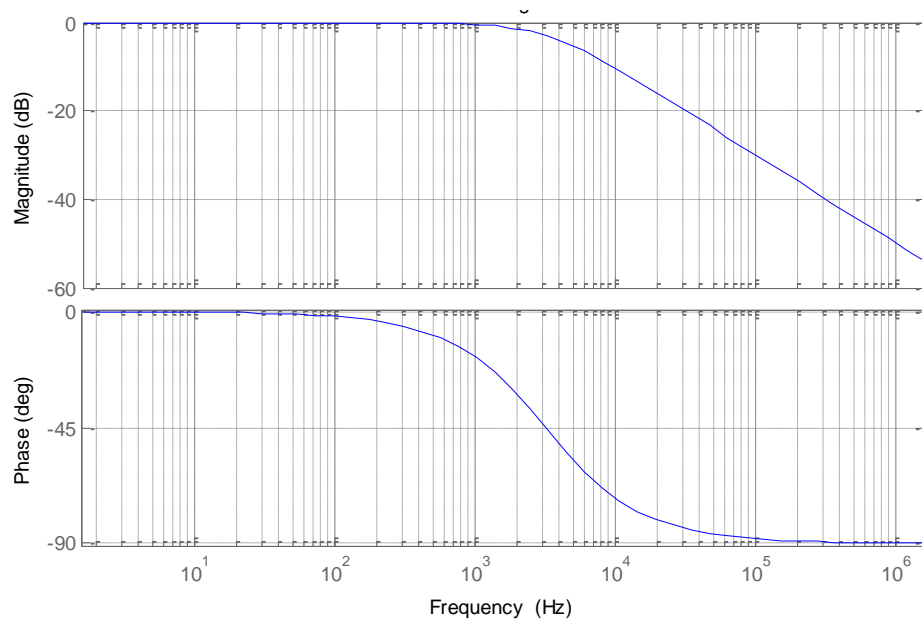


Figure 4.28 Bode plot of the delay caused by the digital controller

With the previous analysis, a double loop controller is proposed for the first module, as given in Figure 4.29. The inner loop feedback is capacitor current  $i_{cf}$ , and the outer loop feedback is the grid current  $i_g$ . To design the compensators for the outer and inner loop ( $G_{c1}$  and  $G_{c2}$ ), the system block diagram is derived, as shown in Figure 4.30. The transfer functions in the block diagram are derived previously.

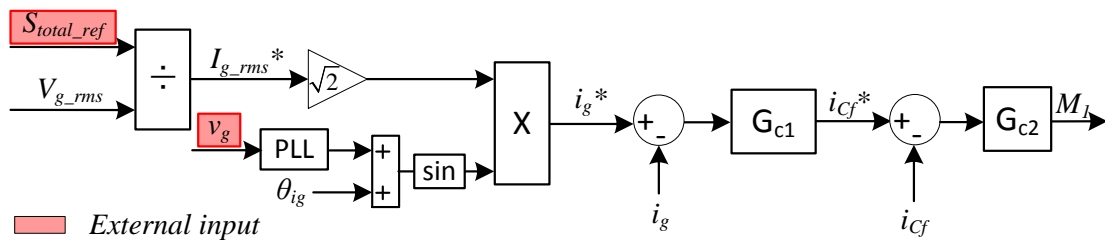


Figure 4.29 Proposed controller for the first module

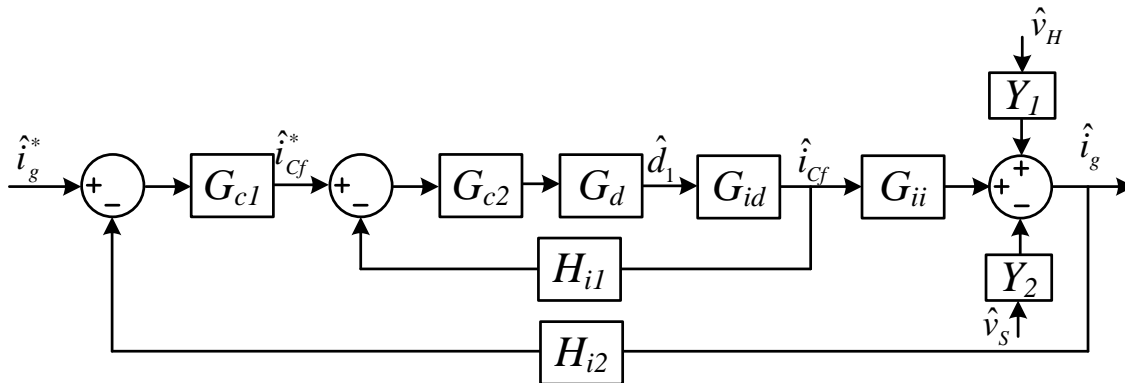


Figure 4.30 Block diagram of the first module with double loop control

For AC output application, the proportional-resonant (PR) controller provides some advantages in comparison with the traditional proportional-integral (PI) controller [89], [90]. In summary, the PR controller can provide high gain at selected resonant frequency to eliminate steady state error at that frequency, and unlike the PI controller, no axis transformation is needed for the PR controller to achieve this. Moreover, multiple resonant frequencies can be easily implemented in PR controller to not only compensate the fundamental component but also compensated the harmonics. Therefore, the PR controller will be used here for the double loop control.

The transfer function a PR controller is given in (4.72), where  $\omega$  is the resonant frequency,  $\omega_c$  is the cutoff frequency,  $K_P$  and  $K_I$  are the gains for proportional and resonant controller, respectively. This transfer function can be written in another form, as given in (4.73) where  $p_1$  and  $p_2$  are a pair of complex poles at resonant frequency  $\omega$  (considering that  $\omega_c \ll \omega$ ),  $z_1$  and  $z_2$  are a pair of complex zeros or two real zeros, depending on the parameters.

$$G_{PR}(s) = K_P + \frac{2K_I \omega_c s}{s^2 + 2\omega_c s + \omega^2} \quad (4.72)$$

$$G_{PR}(s) = K \cdot \frac{(s - z_1)(s - z_2)}{(s - p_1)(s - p_2)} \quad (4.73)$$

The open loop control to output transfer function of the inner loop ( $G_{id}$ ) is given in Figure 4.31. It can be seen that the resonant peak as seen in the system control to output transfer function (Figure 4.27) is mainly caused by the inner loop control to output transfer function. So the inner loop controller needs to take care of this resonant peak. This is also the purpose to add an inner loop. Therefore, the design goal of the inner loop is to have a bandwidth that is higher than the resonant frequency. The gain of the inner loop controller does not need to be high because the system steady state error is taking care of by the outer loop controller.

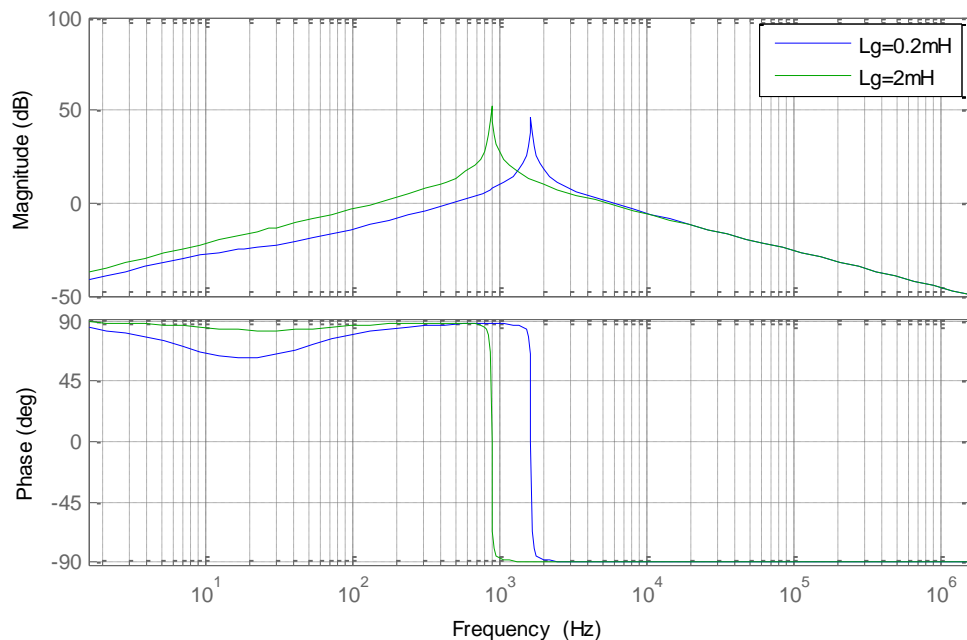


Figure 4.31 Bode plot of the control to output transfer function of the inner loop

A compensator is designed for the inner loop, as given in (4.74), where  $\omega=120\pi$  is the grid frequency (for 60 Hz grid) and  $\omega_c=10$  rad/s.

$$G_{c2}(s) = 1.1 + \frac{20\omega_c s}{s^2 + 20s + \omega^2} \quad (4.74)$$

With the designed compensator, the loop gain of the inner loop is given in Figure 4.32. The designed PR controller places a pair of complex poles and a pair of complex zeros at 60 Hz. It can be seen that for both stiff and weak grid, the controller bandwidth is higher than the system resonant frequency and the phase margin is sufficiently high. To verify the effectiveness of the inner loop controller for eliminating the system resonant peak, the close loop transfer function of the inner loop is plotted in Figure 4.33. It is clear that the resonant peak is completely eliminated. This makes the outer loop design much easier.

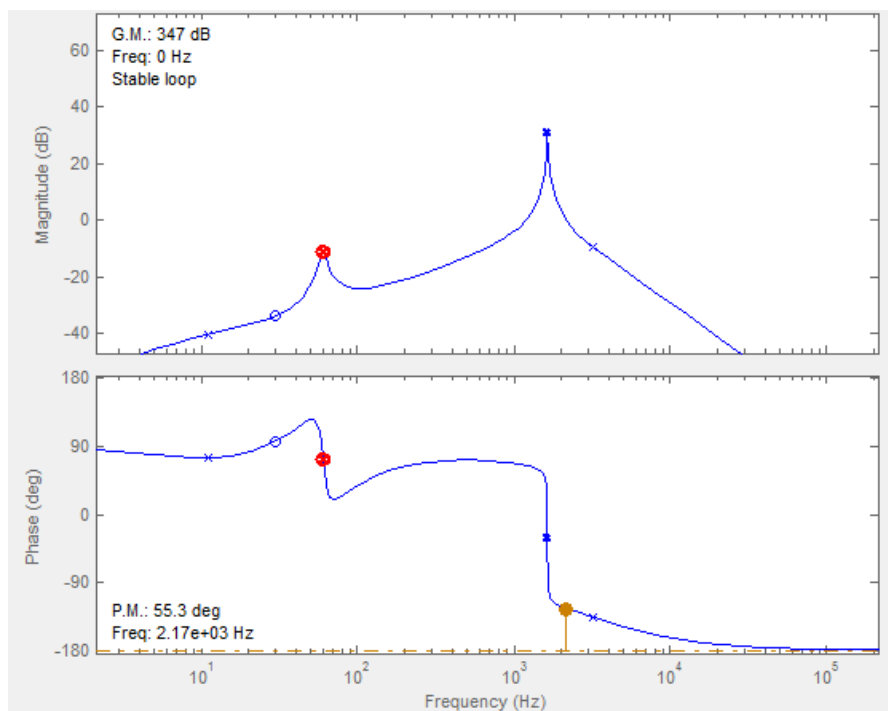
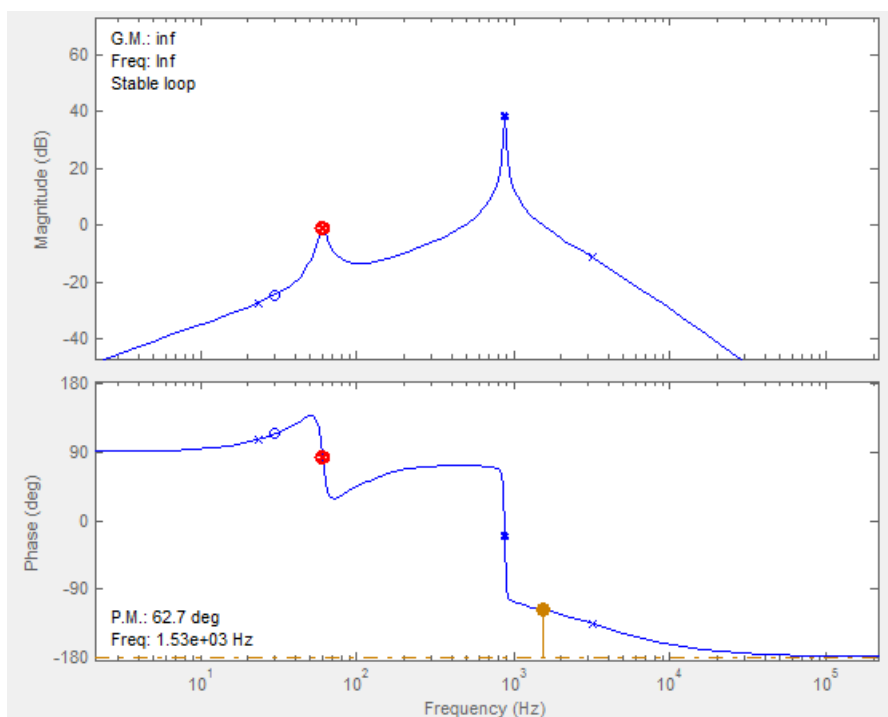
(a)  $L_g=0.2$  mH(b)  $L_g=2$  mH

Figure 4.32 Loop gain of the inner loop for stiff and weak grid

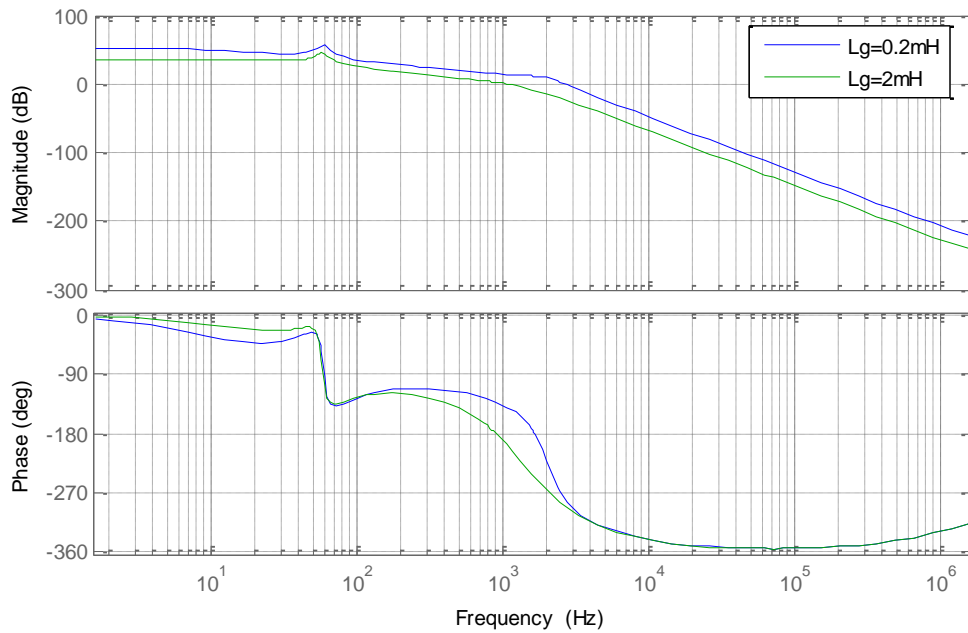


Figure 4.33 Bode plot of the close loop transfer function of the inner loop

The outer loop compensator design is also based on the PR controller. However, PR controller alone cannot provide enough phase and gain margin without compromising the controller bandwidth. To solve this problem, an additional zero is added to compensate the phase margin. An additional pole is also added to balance the system and compensate the gain margin. The resulted compensator is given in (4.75).

$$G_{cl}(s) = 2.266 \cdot \frac{s^3 + 907s^2 + 2.932 \times 10^5 s + 9.758 \times 10^7}{s^3 + 1056s^2 + 1.628 \times 10^5 s + 1.472 \times 10^8} \quad (4.75)$$

With this compensator, the loop gain of the outer loop is given in Figure 4.34. It can be seen that for both cases with stiff and weak grid, the controller gives sufficient phase and gain margin, and relatively high bandwidth for 60 Hz grid.

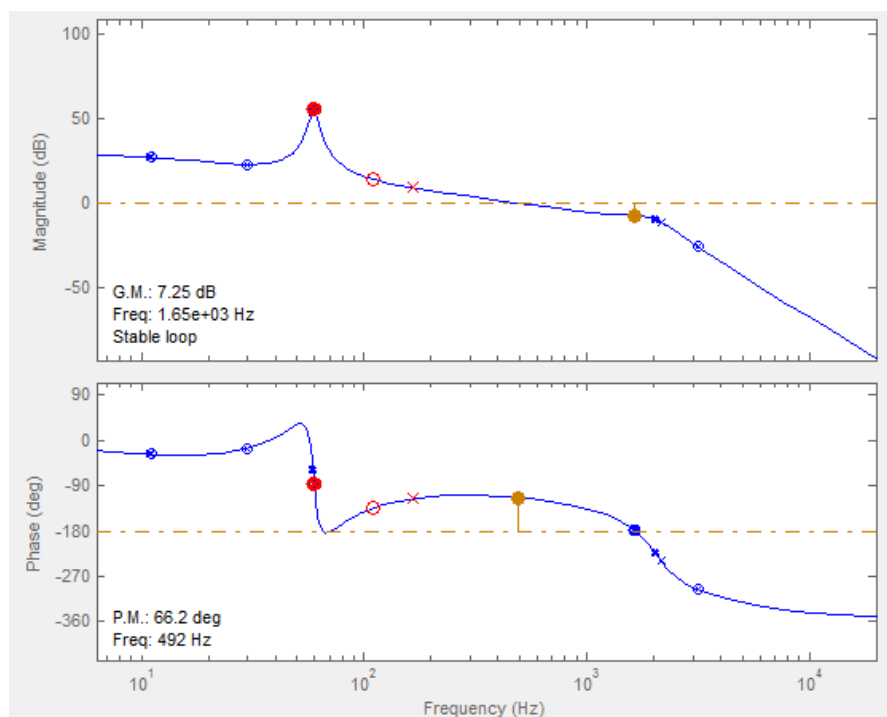
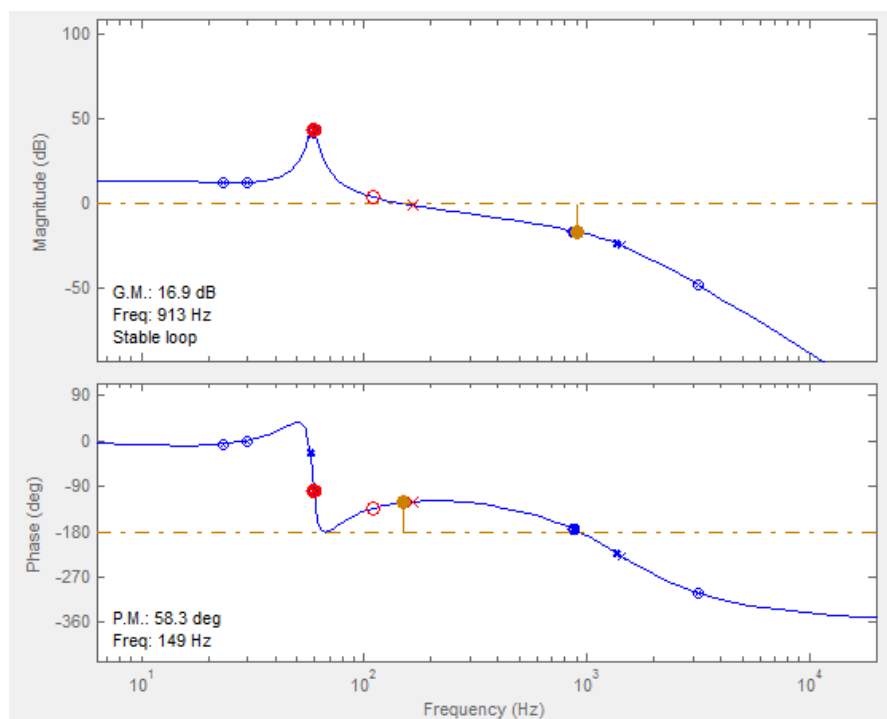
(a)  $L_g=0.2$  mH(b)  $L_g=2$  mH

Figure 4.34 Loop gain of the outer loop for stiff and weak grid

## 4.4 Experiment Verification

To verify the proposed energy storage system, two experiment setups are built. The first setup is used to verify the concept and tune the parameters. For this purpose, a single real time digital simulator (OPAL-RT) is used to control all modules. This simulator has high computation power, very fast and accurate ADC and DAC, and it is very convenient to monitor any interested point in the controller. After the proposed concept is verified, a more practical system is built with each module having its own DSP based controller. Wireless communications between the energy storage system and high level system controller are also implemented.

The same H-Bridge module is used for both setups. The switch used in the H-Bridge module is IRFP4310ZPbF, which is a 100V/120A MOSFET. With this switch, the H-Bridge module can deliver 1 kW with 48V DC side voltage and 500 W with 24V DC side voltage.

The output filter (L or LC or LCL) of the grid connected inverter is very important to the performance of the inverter and has been extensively studied [93]–[96]. A simplified procedure to design the LC filter is summarized here.

(1) The VA rating of the capacitor should be less than 5% of the rated power of the system, which gives

$$C \leq \frac{5\% \cdot P_o}{\omega \cdot V_{g\_rms}^2} \quad (4.76)$$

where  $P_o$  is the rated output power of the system,  $V_{g\_rms}$  is the RMS value of the grid voltage and  $\omega$  is the angular grid frequency.

(2) The VA rating of the inductor should be less than 10% of the rated power of the system, which gives

$$L \leq \frac{10\% \cdot V_{g\_rms}^2}{\omega \cdot P_o} \quad (4.77)$$

(3) The resonant frequency of the LC filter should be higher than 10 times of the grid frequency, which gives

$$LC \leq \frac{1}{100\omega^2} \quad (4.78)$$

For simplicity, the same LC filter is used for both setups. The value of this LC filter is designed based on the second setup (with  $P_o=800W$  and  $V_{g\_rms}=48V$ ).

#### 4.4.1 Setup 1: Concept Verification

The first setup consists of three H-Bridge modules and two types of batteries, as shown in Figure 4.35 and Figure 4.36. Since the modules do not have enough voltage to directly interface with the grid, a transformer is used to match the voltage. The detailed parameters of this setup are given in Table 4.3.

Table 4.3 Parameters of setup 1

Parameter	Value
Lead acid battery voltage ( $V_{bat1}, V_{bat2}$ )	24 V
Li-ion battery voltage ( $V_{bat3}$ )	28 V
Inductor ( $L_f$ )	745 $\mu$ H
Capacitor ( $C_f$ )	60 $\mu$ F
ESR of $L_f$ ( $R_{L_f}$ )	28 m $\Omega$
ESR of $C_f$ ( $R_{C_f}$ )	1.6 m $\Omega$
Grid voltage ( $v_s$ )	120 V (RMS)
System interface voltage ( $v_g$ )	28 V (RMS)
H-Bridge switching frequency ( $f_{sw}$ )	20 kHz

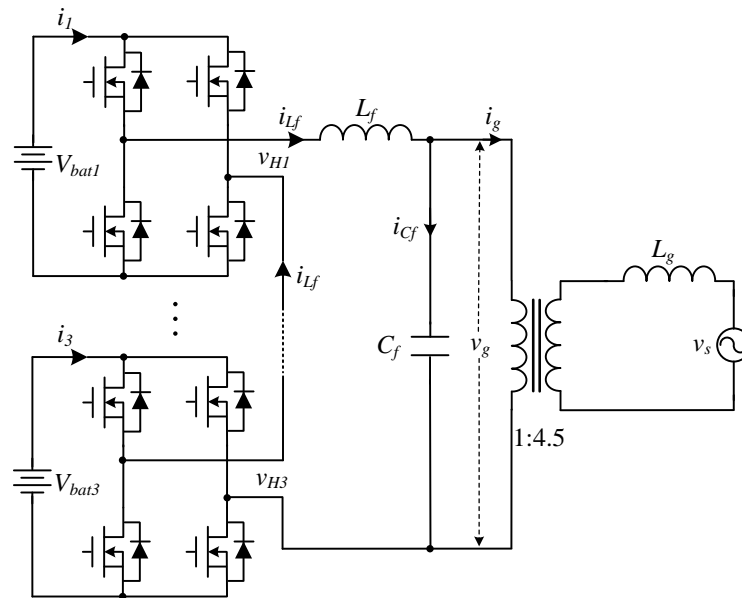


Figure 4.35 System configuration of experimental setup 1

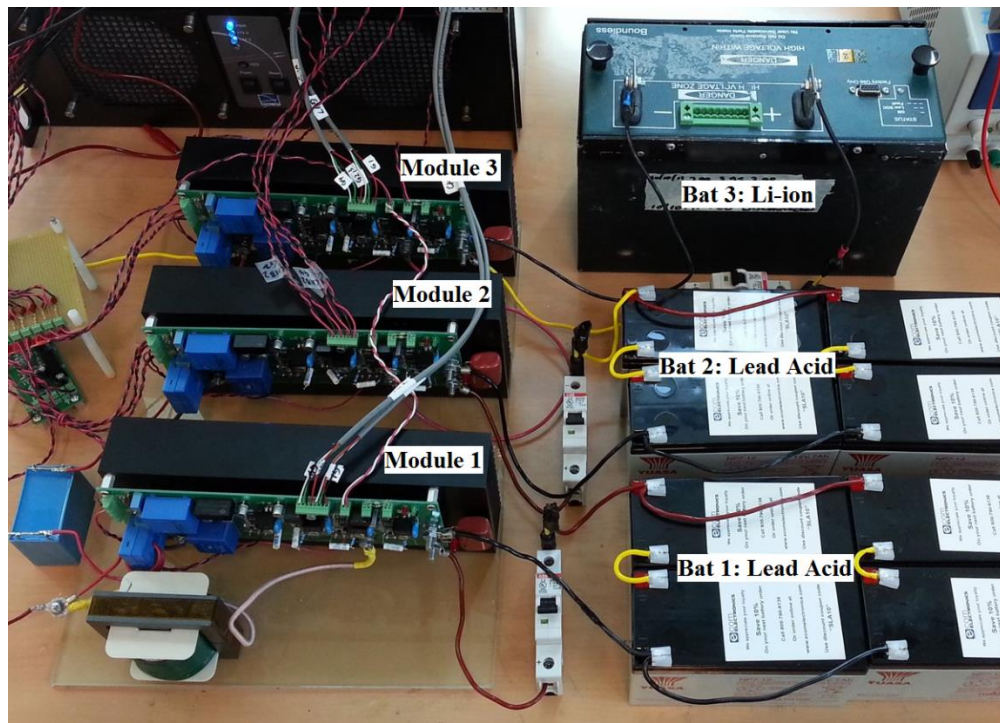


Figure 4.36 Picture of experimental setup 1 with three H-Bridge modules and single controller

Figure 4.37 and Figure 4.38 give the transient response of the system output voltage and current, with the power command having a step change (from 100W to 200W or from 200W to 100W). It can be seen that the output current changes almost immediately and the waveform does not have distortion during the transition.

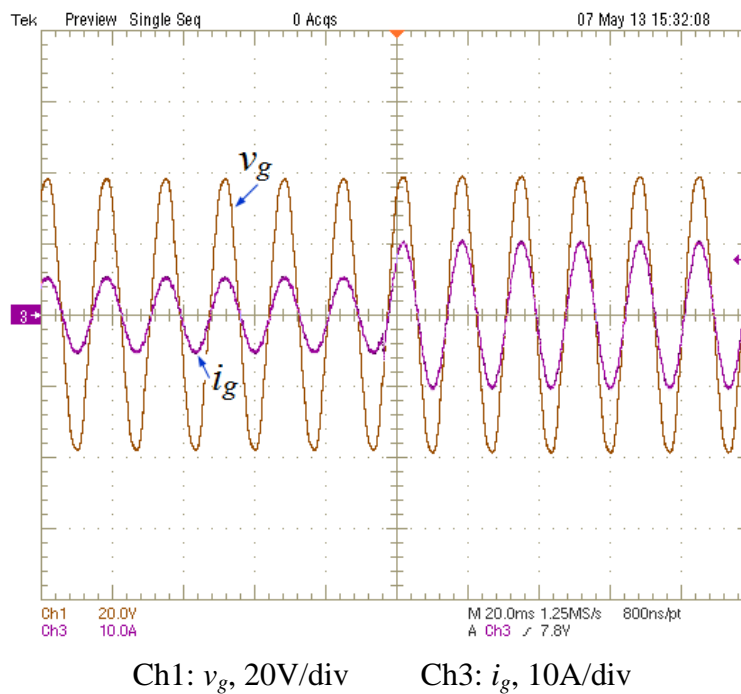


Figure 4.37 Output power step change: low to high

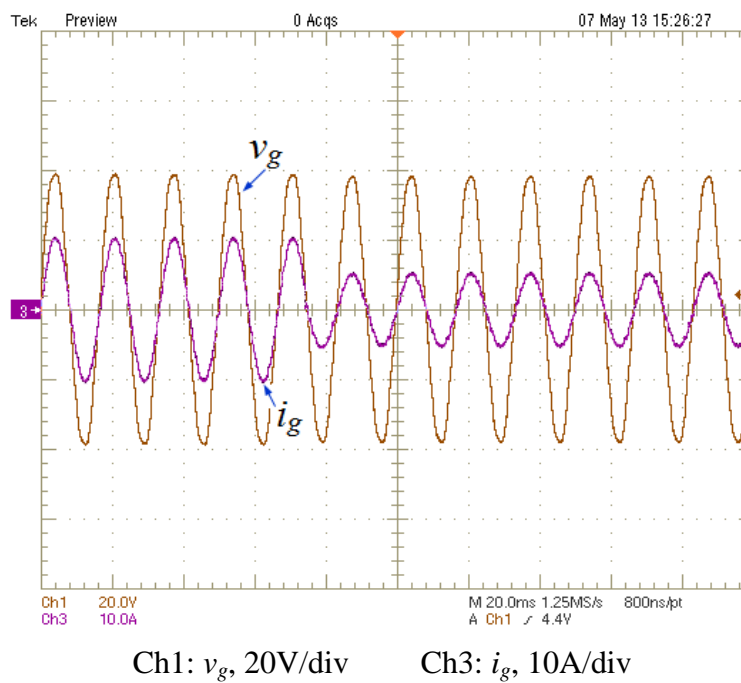


Figure 4.38 Output power step change: high to low

Figure 4.39 shows the filtered output voltage of each module, which determines the output power from each module (for a given output current which is the same for all modules). Obviously, each module is outputting different power and the transient response of power command step change is fast and smooth. It is also clear that the output voltage of the first module contains relatively high level of harmonics. This is because the output voltages of the 2<sup>nd</sup> and 3<sup>rd</sup> modules are almost purely sinusoidal, so all the harmonics of the grid voltage are contained in the output voltage of the first module.

Figure 4.40 and Figure 4.41 demonstrate the change of operating mode between charging and discharging mode. When the voltage and current are in phase, the batteries are discharging and sending power to the grid. When the voltage and current are out of phase, the batteries are being charged and consuming power from the grid. From both figures it can be seen that the transitions are fast and there is no obvious distortion on the waveforms during the transitions.

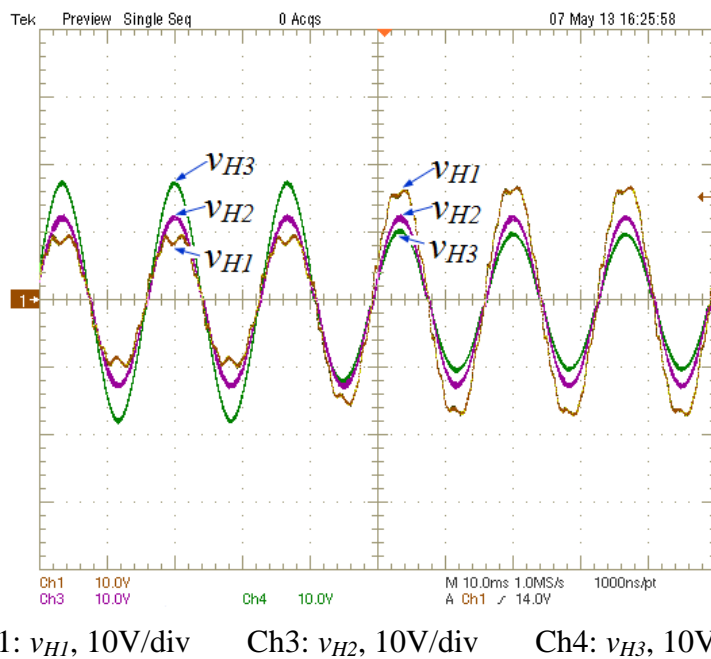


Figure 4.39 Change of power distribution between modules (power commands for the three modules change from 30W, 50W and 70W to 60W, 50W and 40W, respectively)

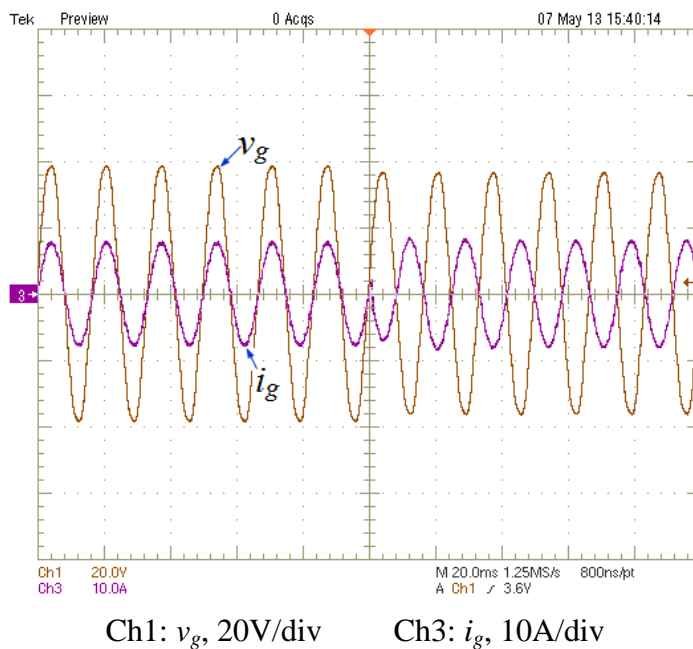


Figure 4.40 Change of operating mode: discharging to charging

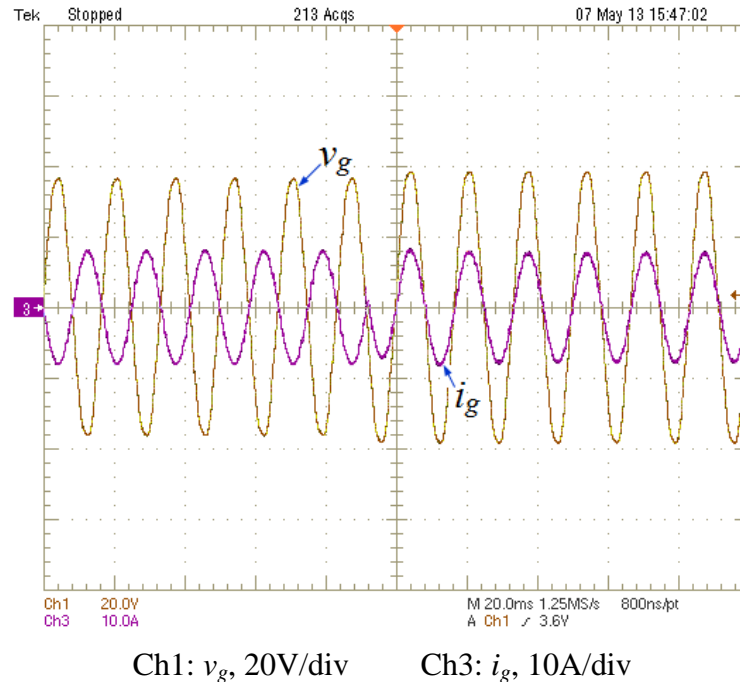


Figure 4.41 Change of operating mode: charging to discharging

#### 4.4.2 Setup 2: Practical system implementation

This setup is built to demonstrate the integration of Distributed Energy Storage Device (DESD) into the Future Renewable Electric Energy Distribution and Management (FREEDM) systems [97]. Figure 4.42 gives an overview of the demonstration setup. The CES unit consists of four H-Bridge modules, each of which has its own controller and Zigbee module. The ARM board is the interface between the CES unit and the central SCADA server. It communicates with each of the H-Bridge modules through Zigbee and forwards the communicating information to the SCADA server through internet. A webpage is designed

and hosted in the SCADA server as shown in Figure 4.43. Authorized users can access this webpage from any computer and have full control of the CES unit.

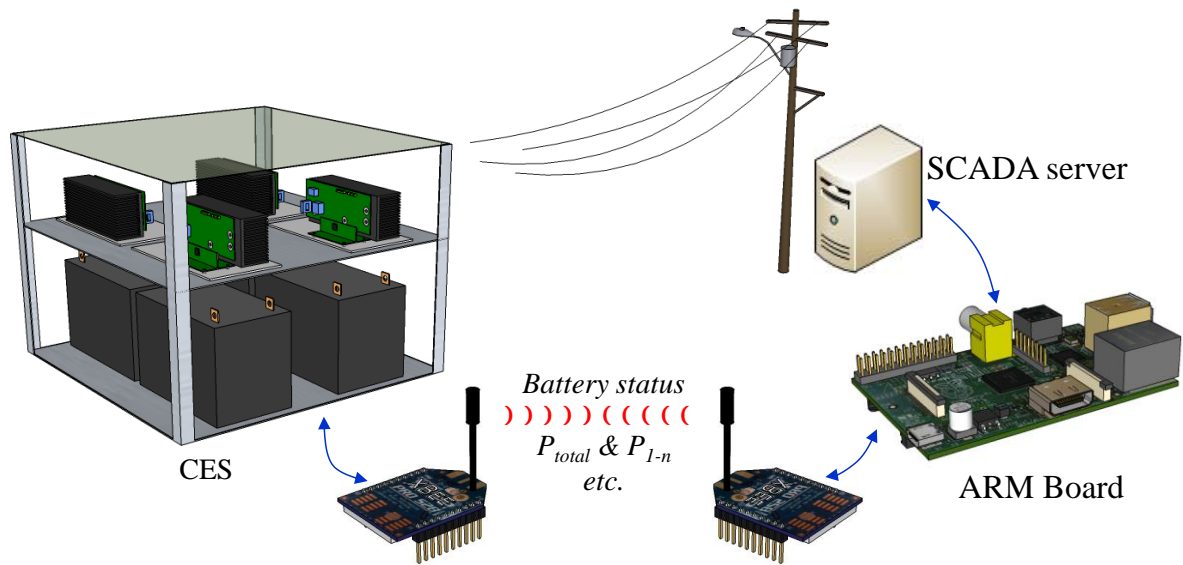


Figure 4.42 System overview of the demonstration setup

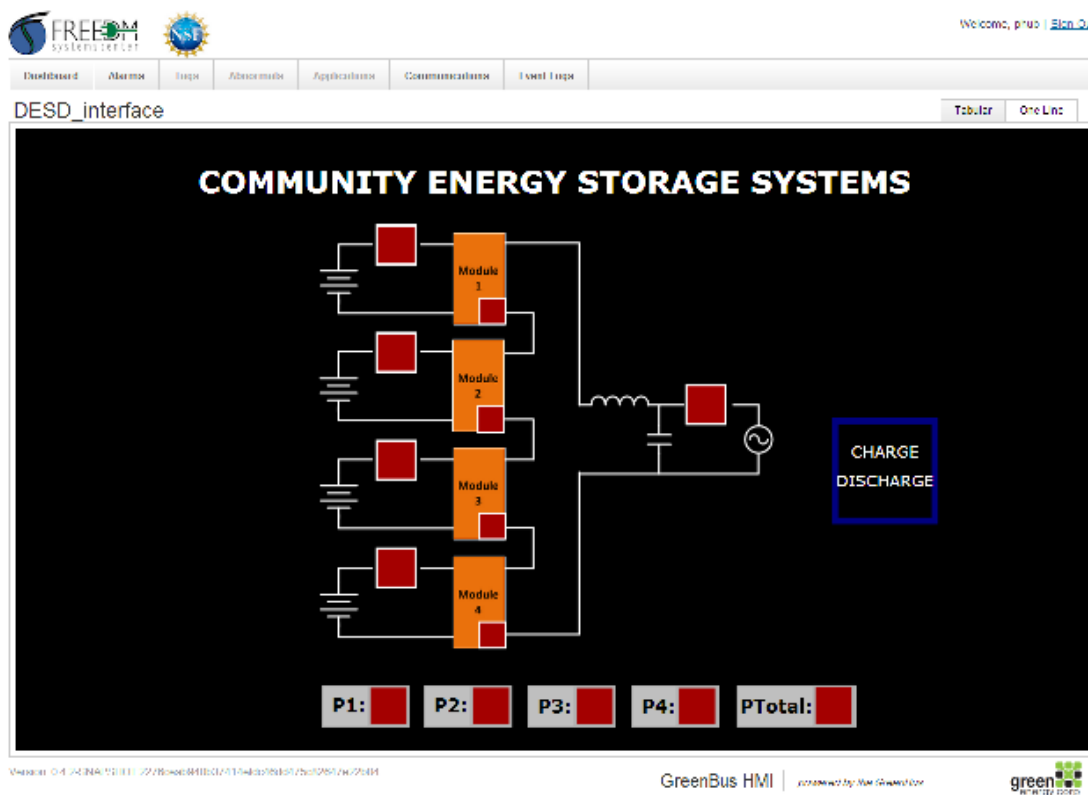


Figure 4.43 Webpage hosted in SCADA server for controlling of the CES unit

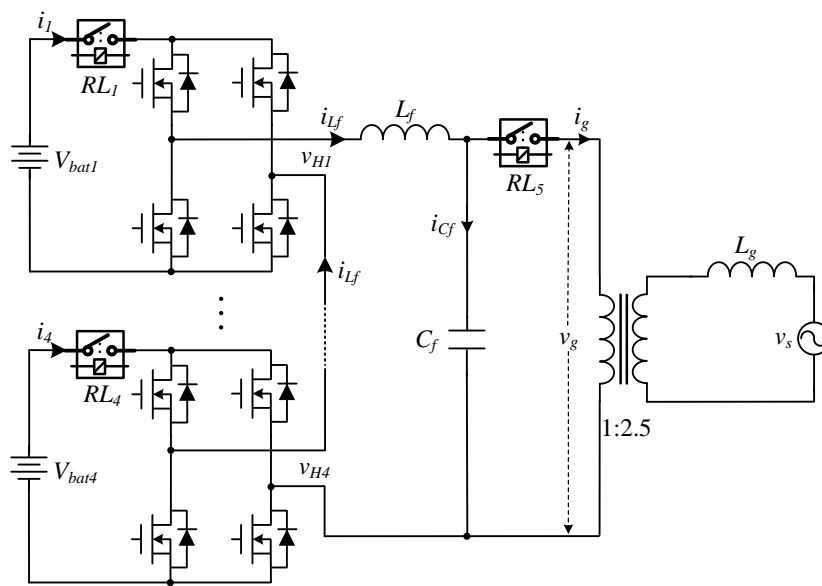


Figure 4.44 System configuration of experimental setup 2

The power stage configuration of the CES unit is given in Figure 4.44. Note that some relays are added to automate the system operation. Detailed parameters of the system are given in Table 4.4. Two types of Li-ion batteries are used in this setup. Type 1 battery packs are salvaged from a Hymotion L5 conversion module for Toyota Prius hybrid electric vehicle. Each battery pack has 8 groups of cells in series. Each group has 6 cells in parallel. The cells are manufactured by A123 with the model number as ANR26650MI which has a nominal voltage of 3.3V and nominal capacity of 2.3 Ah. Therefore, each battery pack has a nominal voltage of 26.4V and nominal capacity of 13.8 Ah. Type 2 battery modules are donated by National Renewable Energy Laboratory (NREL). Each battery pack has 7 groups of cells in series. The number of cells in each group is unknown. The cell nominal voltage is 3.6V which gives the whole battery module a nominal voltage of 25.2V. The capacity of the battery module is around 30 Ah, according to our test. Some pictures of the CES unit are given in Figure 4.45 and Figure 4.46.

Table 4.4 Parameters of setup 2

Parameter	Value
Li-ion battery voltage - type 1 ( $V_{bat1}, V_{bat2}$ )	26.4 V
Li-ion battery voltage - type 2 ( $V_{bat3}, V_{bat4}$ )	25.2 V
Inductor ( $L_f$ )	745 $\mu$ H
Capacitor ( $C_f$ )	60 $\mu$ F
ESR of $L_f$ ( $R_{L_f}$ )	28 m $\Omega$
ESR of $C_f$ ( $R_{C_f}$ )	1.6 m $\Omega$
Grid voltage ( $v_s$ )	120 V (RMS)
System interface voltage ( $v_g$ )	48 V (RMS)
H-Bridge switching frequency ( $f_{sw}$ )	20 kHz



Figure 4.45 Pictures of experimental setup 2 with four H-Bridge modules and distributed controllers

Since now all the modules have their own controllers and there is no communication between them, the SCADA server needs to coordinate with all the modules to make sure the system is operating properly, especially during start-up and shut-down operation. As analyzed in section 4.3.1, the first module alone cannot control the output current. Before the first module works, all the other module need to have a stable output. The detailed procedure of the system start-up is given as followed:

(1) Plug in the CES unit into grid. All the controllers will get power and start to work, but the PWM outputs are blocked so the H-Bridges are not working.

(2) Turn on battery side relays ( $RL_1$ ,  $RL_2$ ,  $RL_3$ ,  $RL_4$ ) first and then the grid side relay ( $RL_5$ ). Now the grid voltage is evenly distributed to the output of each module.

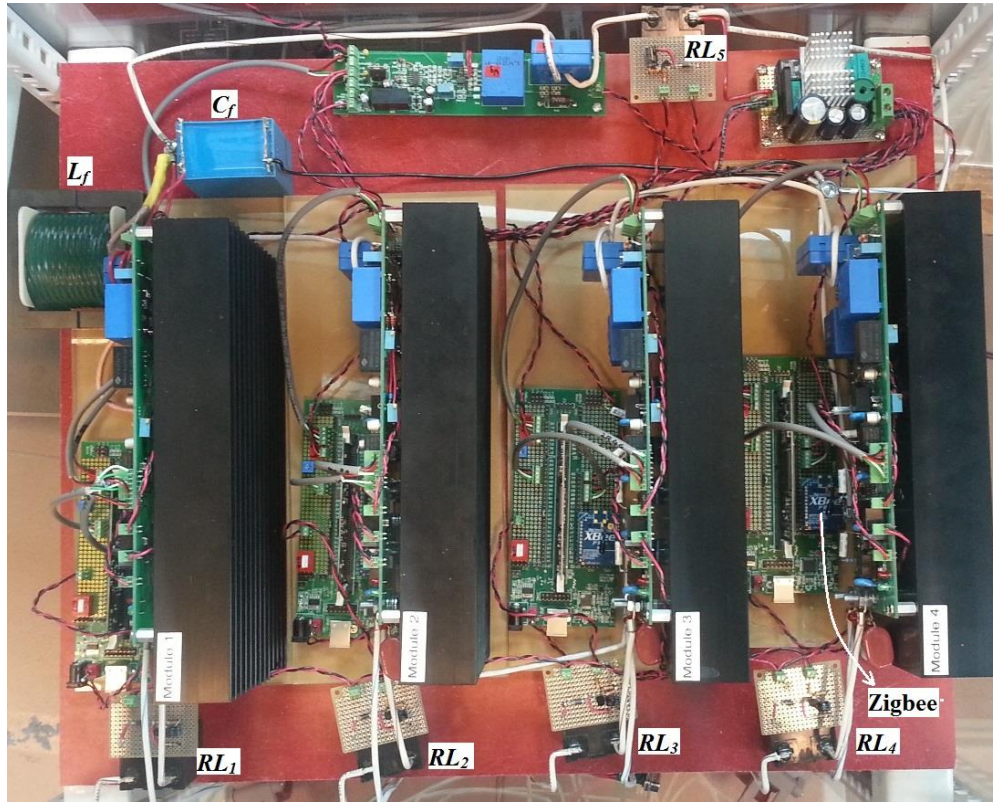


Figure 4.46 Detailed view of the four H-Bridge modules in setup 2

(3) Enable the PWM outputs of the 2<sup>nd</sup> to n<sup>th</sup> module. By default, total power command is zero and all these modules will output a voltage of  $v_g/n$ .

(4) Enable the PWM output of the first module. Since the total power command is zero, the first module will maintain  $i_g$  to be zero.

(5) Send power commands to all the modules. The system begins normal operation.

The shut-down procedure is exactly in the reverse sequence of the start-up procedure.

All the functionalities of this system have been tested with great success. Figure 4.47 gives the transient response of the output current when there is a step change of the power command. Like in setup 1, the response is fast and smooth. Figure 4.48 gives the response of

output current when the operating mode changes. Again, the response is very fast with a little overshoot on the current amplitude during the first cycle after the mode change. Figure 4.49 gives the transient response when injecting reactive power. The grid current is leading grid voltage by  $45^\circ$ , so the CES unit is providing reactive power to the grid. The grid current response is fast and smooth, similar to the response when there is no reactive power injection.

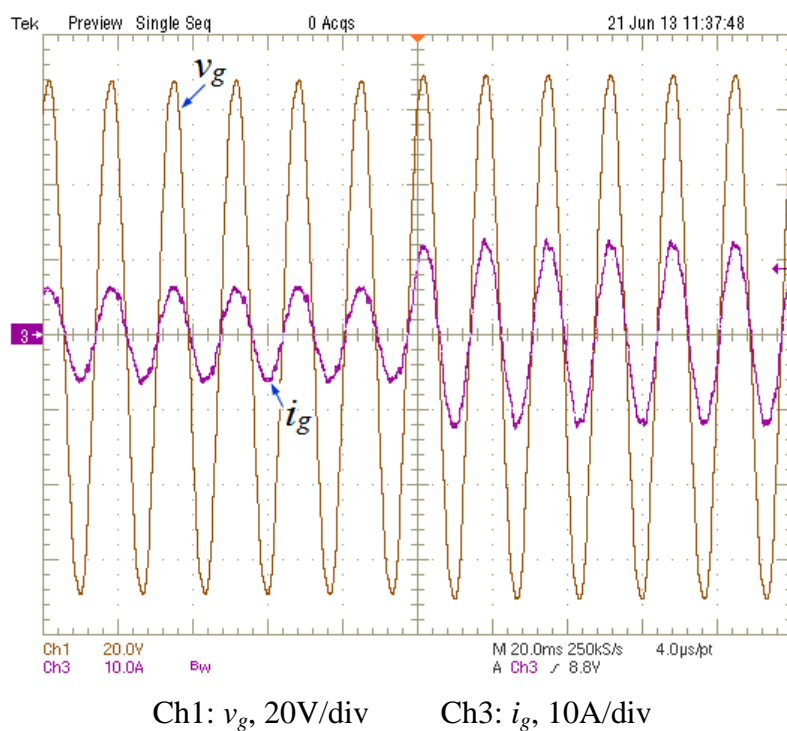


Figure 4.47 Step change of output power from 200W to 400W

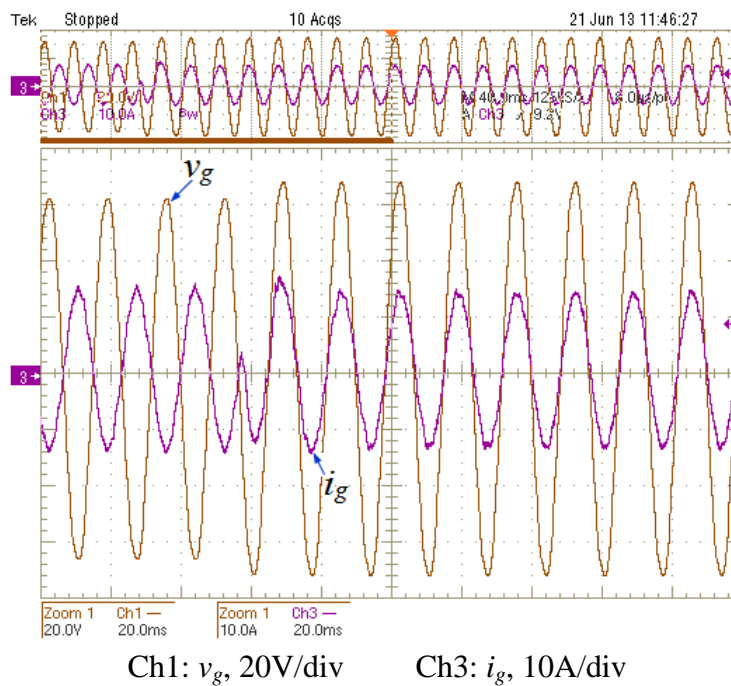


Figure 4.48 Change of operating mode: from charging to discharging

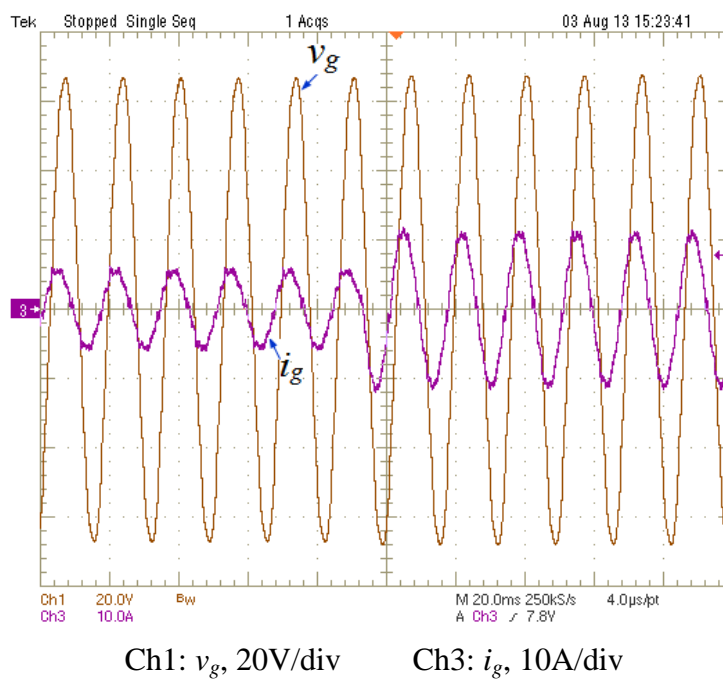


Figure 4.49 Step change of output power from 180W to 360W with reactive power injection

### 4.4.3 Efficiency Test

One advantage of the proposed system is that it has only one power conversion stage and thus should have high efficiency. To verify this, the efficiency of the system needs to be measured. Since all the H-Bridge modules are the same, only one H-Bridge module is tested. The setup configuration is given in Figure 4.50. The parameters of this setup are given in Table 4.5. Note that a DC side inductor is added to filter the input current to make it easier to accurately measure this current. The WT3000 precision power analyzer from YOKOGAWA is used to measure the efficiency, which has a basic power accuracy of 0.02%. The measured quantities are  $v_{in}$ ,  $i_{in}$ ,  $v_o$  and  $i_o$ , as shown in Figure 4.50.

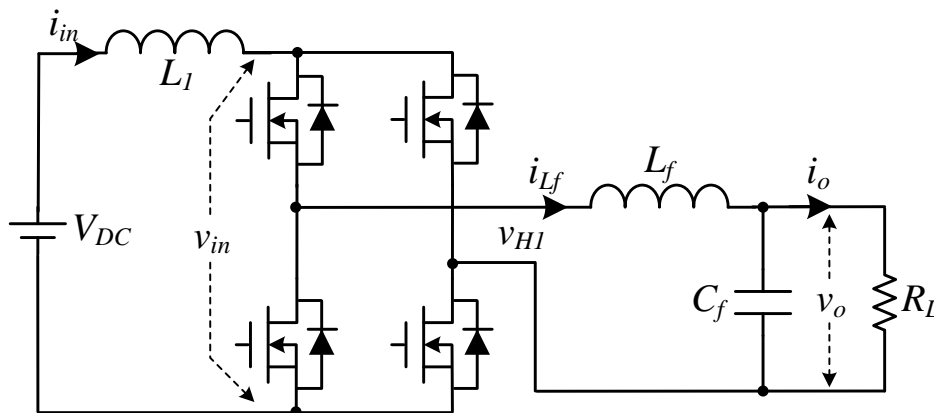


Figure 4.50 Configuration of the setup for efficiency test

Table 4.5 Parameters of setup for efficiency test

Parameter	Value
DC side voltage ( $V_{DC}$ )	28 V (unless otherwise specified)
Inductor ( $L_f$ )	200 $\mu$ H
DC side inductor ( $L_l$ )	1 mH
Capacitor ( $C_f$ )	230 $\mu$ F
ESR of $L_f$ ( $R_{L_f}$ )	12.5 m $\Omega$
ESR of $C_f$ ( $R_{C_f}$ )	11 m $\Omega$
H-Bridge switching frequency ( $f_{sw}$ )	20 kHz (unless otherwise specified)
H-Bridge modulation index (m)	0.8 (unless otherwise specified)

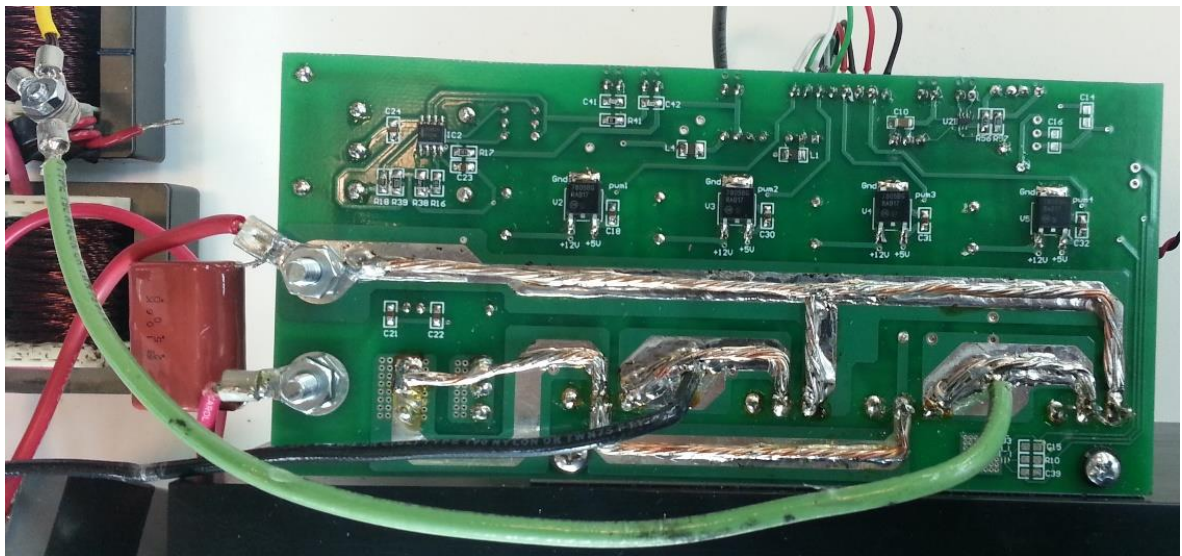


Figure 4.51 Reinforcement of the PCB traces

Through some initial tests, it has been found that the efficiency decreases as the power goes up, and all the measured efficiencies are below 95%. One explanation of this result is that the conduction losses dominate in the power losses of this system. However, the on-state

drain-to-source resistance of the MOSFET (IRFP4310ZPbF) is fairly low ( $4.8\text{ m}\Omega$ ). The ESR of the output filter ( $L_f$ ) is also low, as seen in Table 4.5. Then the only place that could have high conduction loss will be the PCB traces of the power stage. Based on this theory, the PCB traces are reinforced with additional wires, as seen in Figure 4.51. All the wires that connect the H-Bridge and output filters and load are replaced with thicker wires.

With all the adjustments, the results are very promising. As seen in Figure 4.52, the efficiencies for all test points are above 95.5% and the maximum efficiency is 97.6%. However, the peak efficiency happens when the load is low and after that the efficiency decreases as the power increases. Therefore, the conduction losses still dominate the power losses. To further confirm this, the switching frequency is reduced from 20 kHz to 10 kHz. As shown in Figure 4.52, there is no substantial difference on the efficiency for different switching frequencies. With that, it is safe to predict that the efficiency can be even higher if the PCB is redesigned to shorten the power stage traces and thicker wires are used.

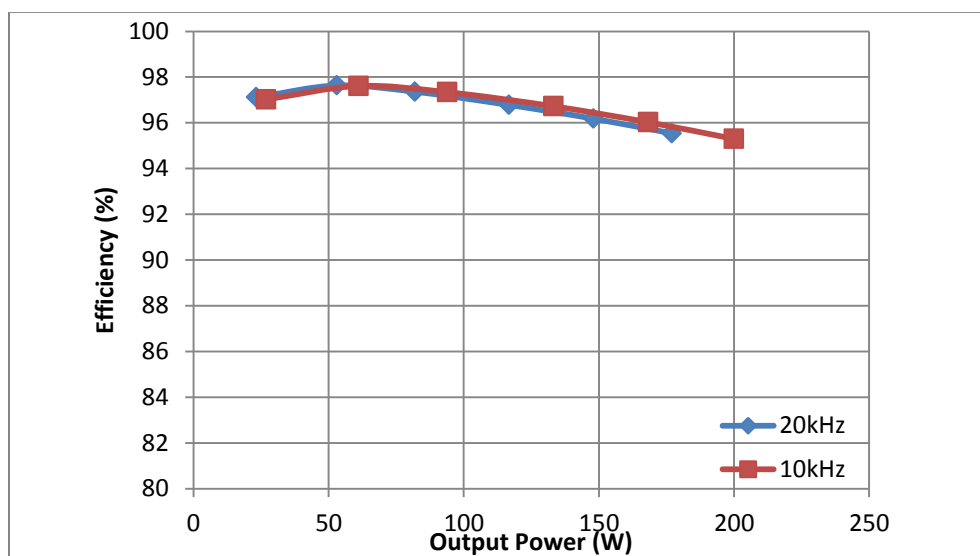


Figure 4.52 Efficiency of the H-Bridge with different load and switching frequency

Since the conduction loss dominates, it should be beneficial to increase the voltage such that the current is lower for a certain power and thus the conduction loss is lower (conduction loss is proportional to the square of the current). To confirm this, the efficiencies are measured for different DC side voltages, as given in Figure 4.53. It can be seen that except for the very low load, higher DC side voltage gives substantial improvement on the efficiency.

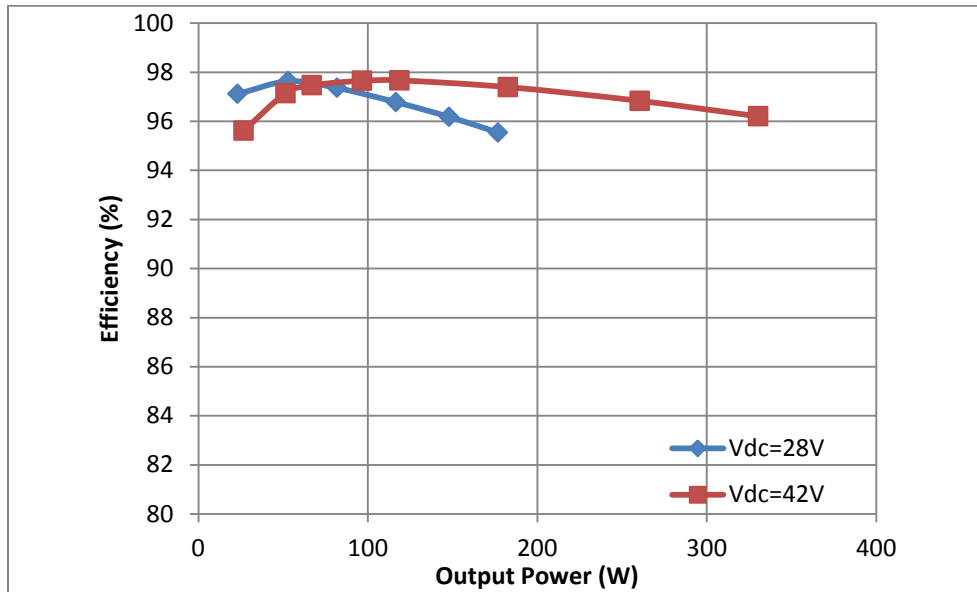


Figure 4.53 Efficiency of the H-Bridge with different load and DC side voltage

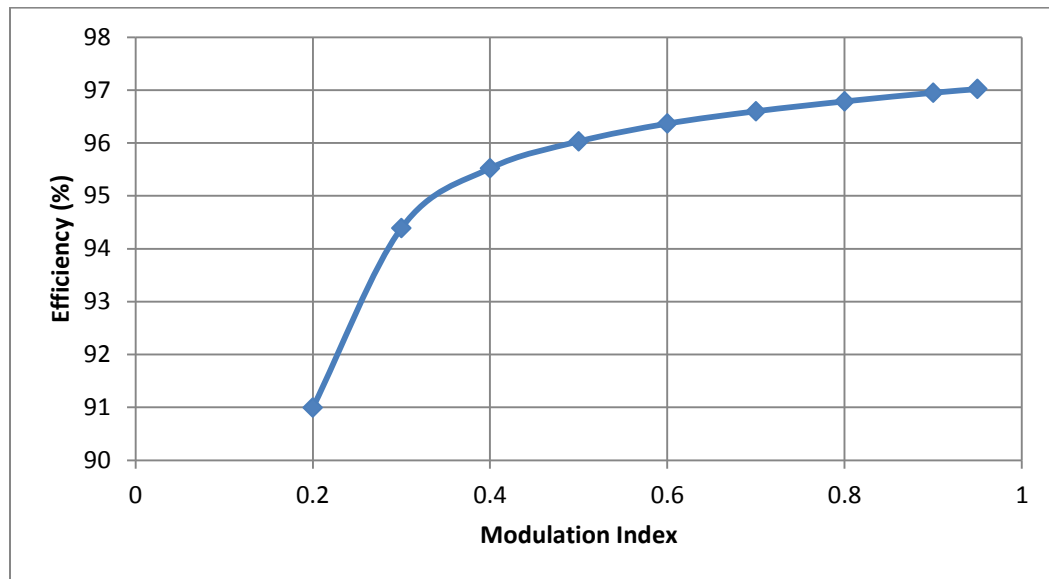


Figure 4.54 Efficiency of the H-Bridge with different modulation index ( $R_L=1.67 \Omega$ )

The efficiencies for different modulation indices are also measured, as given in Figure 4.54. Since the load resistance is fixed, the ratio of the conduction losses and output power should be fixed if we consider the H-Bridge as a voltage source in series with resistive impedance. Then other losses (mainly the switching loss) will determine the efficiency. If the switching loss is considered to be roughly constant, then the efficiency should increase as the output power increases, as seen in Figure 4.54.

It is necessary to mention that all the efficiency results are measured and calculated without taking into account of the power consumption of the gate driver, the controller and the voltage or current sensor. However, these power consumptions are also measured, as given in Table 4.6. The power consumptions are fairly low and could be further reduced. The DSP board is a general purpose experiment kit which has onboard emulator and other circuitry. A dedicated control board for this system should have lower power consumption.

Moreover, the voltage and current sensors (LV 20-P and LA150-P from LEM) can be replaced with low cost low power sensors.

Table 4.6 Power consumptions of auxiliary components

Parameter	Power consumption
4 gate drivers	1.08 W
DSP board	0.96 W
Voltage/current sensor	0.50 W

## 4.5 Conclusions

In this chapter a Community Energy Storage (CES) system is proposed by utilizing dissimilar batteries. Since the batteries come from different sources, they may have different chemistry, different terminal voltages (12V~48V for this project), different capacities, etc. On the other hand, the grid voltage is 120V/240V which is much higher than the battery voltages. It is obvious that these unlike batteries cannot be directly connected in series to get enough voltage to interface with the grid. And it is very difficult to design a converter that can have high voltage step-up ratio and wide input voltage range at the same time. Therefore, the cascaded H-Bridge leaves to be a suitable topology for this application. Since the batteries are different, the power flow from each battery needs to be independently controllable. Modular design is also preferable considering that there will be a number of batteries integrated in the system. However, for cascaded H-Bridge topology, all the H-Bridge modules are physically linked together. It is not easy to have independent control of

each H-Bridge and have modular design. Several control strategies have been proposed in [83]–[86] to have independent control of each H-Bridge. But all these control strategies are centralized control. To have modular design and independent power flow control of each H-Bridge module, a distributed control strategy is proposed in this chapter. With this new control strategy, each H-Bridge module can have its own controller and communications between these controllers are avoided. The power flow from each module can be independently controlled and the power commands are sent through wireless communication by the system level controller. Experiment setup is built to verify the effectiveness of the proposed control strategy with great success. Efficiency test of the H-bridge shows higher than 97% efficiency. A small scale CES unit is also built to demonstrate the integration of the distributed energy storage system into the FREEDM system. The CES unit consists of four H-bridge modules, each of which has a controller that communicates with the SCADA server via Zigbee wireless communication. All the operations of this system are tested with great success.

## **Chapter 5. Conclusions and Future Work**

In this dissertation, the integration of DC energy storage devices into the DC and AC distribution system is investigated. Multiple contributions are made during the process of this research work, as summarized in section 5.1. Some potential topics that worth investigation in the future are given in section 5.2.

### **5.1 Summary of the Contributions**

The contributions made in this dissertation are summarized as follows:

(1) The power demand of the fast charging station is studied, which is one of the earliest work on this topic. The power level for the fast charger is determined first, with the conclusion that the DC level 3 charging method proposed by SAE J1772 is suitable for the fast charger. The power demand profile of the fast charging station is then derived from simulations. The results show that the average power demand is much lower than the peak power demand. This finding suggests that the power delivery architecture of the fast charging station can be optimized.

(2) Based on the studies of the fast charging station power demand, the power delivery architecture is proposed with DC power distribution line and energy storage integration. With the energy storage system to provide peak power, the AC/DC frontend for the charging station can be sized based on the average power demand which is substantially lower than the peak power demand. Simulation results show that a fast charging station that has 10 fast

chargers (with rate power of 240 kW) only needs a 1.1 MW grid tie and 20 kWh energy storage system to provide more than 98% of the power demand.

(3) The 12-pulse diode rectifier is justified to be the suitable topology for the AC/DC frontend of the fast charging station. As an alternative, the PWM rectifier is not preferable because of its high cost, low efficiency (compared with the diode rectifier), complicated control and thus low reliability. Power losses on the switches for 12-pulse diode rectifier and PWM rectifier are calculated and compared.

(4) A new approach is proposed to eliminate AC side current harmonics of the proposed 12-pulse diode rectifier. This approach utilizes DC side DC/DC converters to directly shape the rectifier output currents and thus indirectly improve the power quality on the AC side. Moreover, the same DC/DC converter can also be used to integrate the energy storage devices. Comparing with existing methods, this approach has multiple advantages such as eliminating the use of low frequency transformers for shaping the rectifier output current, providing energy storage interface to the system, and functioning regardless of the continuity of the initial rectifier output current.

(5) A new procedure to design the output LC filters of the proposed 12-pulse diode rectifier is developed, which results in substantially lower inductance and capacitance for the LC filter and lower harmonics on the AC side. Traditionally, the LC filter is designed to attenuate the voltage and current ripples on the rectifier output. However, for the proposed 12-pulse diode rectifier it has been found that it is beneficial to design the LC to resonant at 6 times of the line frequency such that the current ripples will be amplified.

(6) With the new procedure to design LC filters, a novel approach is developed to shape the rectifier output currents and improve the AC side power quality. Instead of directly shaping the rectifier output currents, as proposed previously, the DC/DC converter is used to inject virtual resistance into the LC filter and thus shape the rectifier output currents. This implementation provides even better results in terms of harmonics elimination and minimizing VA rating of the DC/DC converter. It also provides the third functionality of the DC/DC converter, which is compensating the voltage ripple of the DC bus.

(7) Further studying of the virtual resistance injection approach reveals that the DC/DC converter can not only inject virtual resistance but also virtual reactance. This feature can be used to compensate the detuning of LC resonant circuit.

(8) The challenges of utilizing dissimilar batteries in community energy storage systems are identified. After investigating all possible topologies, the cascaded H-Bridge is selected as the most suitable topology for this application.

(9) A new control strategy is proposed for cascaded H-Bridge. Unlike existing control strategies which utilize single central controller to control all the H-Bridges, the proposed control strategy utilizes one controller for each H-Bridge and eliminates interconnections between the controllers. With this control strategy, modular design of the cascaded H-Bridge becomes possible.

(10) A small scale CES unit is built to demonstrate the integration of the distributed energy storage system into the FREEDM system. The CES unit consists of 4 H-Bridge modules. Each of the modules has its own controller and Zigbee wireless communication module to communicate with the FREEDM SCADA server.

## 5.2 Future Work

To make this dissertation more comprehensive, some continuous work is suggested in this section for the future investigation.

For the power delivery architecture design of the fast charging station, the power demand study is based on simulation results because there is no real world data available at the time of writing. However, the electric vehicle industry is under fast developing. With new information comes in, it is necessary to check this design and make proper adjustments.

For the proposed 12-pulse diode rectifier with energy storage integration, the functionalities have been verified with small scale experiment setup. However, this design is intended for high power applications. Therefore, it would be better to build an experiment setup with higher power ratings (tens of kW) and test it with battery chargers as the load. It is also worthwhile to investigate the system level stability of the proposed DC distribution system for the fast charging station.

For the modular design of the cascaded H-bridge, a battery monitoring system is needed to collect the battery information and send the information to the SCADA system. The power command for each module will be determined based on its battery status. An alternative approach is to generate power commands by the local controller on each module, instead of by the SCADA server. Either way, an algorithm needs to be developed to determine the power command based on battery status. A preliminary idea is to make use of the concept of droop control and develop a droop curve for each module based on the battery characteristics. During normal operation, the battery status will be continuously monitored and will be fed into the droop controller. Based on the battery status, the droop controller will

generate the power command which is the maximum power the battery can provide. Since this algorithm can be implemented either on the SCADA server or the local controllers, a trade-off decision needs to be made after comprehensive comparison between these two approaches. There are also some challenging questions that need to be answered, such as: (1) How to effectively determine the droop curve for different batteries (different chemistry, different state of health, etc.)? (2) How to get the total power command for the whole system if the droop control is implemented in the local controllers?

One important advantage of the modular design is the fault tolerance capability, which means when fault happens in any of the modules, that module can be safely isolated from the system and the normal operation of the whole system is not affected. The proposed control strategy enables modular design of the system and makes it possible to have fault tolerance. But additional control strategies and/or additional hardware need to be developed to implement this fault tolerance capability.

## REFERENCES

- [1] U.S. Energy Information Administration (EIA), “International Energy Outlook: DOE/EIA-0484(2011),” 2011.
- [2] C. Han, A. Huang, and M. Baran, “STATCOM impact study on the integration of a large wind farm into a weak loop power system,” *Energy Conversion, IEEE Transactions on*, vol. 23, no. 1, pp. 226–233, 2008.
- [3] H. Bevrani, a. Ghosh, and G. Ledwich, “Renewable energy sources and frequency regulation: survey and new perspectives,” *IET Renewable Power Generation*, vol. 4, no. 5, p. 438, 2010.
- [4] Z. Chen, “Grid power quality with variable speed wind turbines,” *Energy Conversion, IEEE Transactions on*, vol. 16, no. 2, pp. 148–154, 2001.
- [5] H. Lee, B. Y. Shin, S. Han, S. Jung, B. Park, and G. Jang, “Compensation for the Power Fluctuation of the Storage Applications,” *Applied Superconductivity, IEEE Transactions on*, vol. 22, no. 3, p. 5701904, 2012.
- [6] A. A. Hussein, S. Harb, and N. Kutkut, “Design considerations for distributed micro-storage systems in residential applications,” in *Telecommunications Energy Conference (INTELEC), 32nd International*, 2010, pp. 1–6.
- [7] Z. Yang, C. Shen, and L. Zhang, “Integration of a StatCom and battery energy storage,” *Power Systems, IEEE Transactions on*, vol. 16, no. 2, pp. 254–260, 2001.
- [8] P. Ribeiro and B. Johnson, “Energy storage systems for advanced power applications,” *Proceedings of the IEEE*, vol. 89, no. 12, pp. 1744–1756, 2001.
- [9] S. Westphalia, A. Sciences, D. Soest, and L. Ring, “Challenges in Integrating Distributed Energy Storage Systems into Future Smart Grid,” pp. 1627–1632, 2008.
- [10] S. Yeleti, S. Member, and Y. Fu, “Impacts of energy storage on the future power system,” in *American Power Symposium (NAPS), 2010*, 2010, pp. 1–7.
- [11] J. Makansi and Abboud, “Energy Storage, the Missing Link in the Electricity Value Chain,” *ESC (Energy Storage Council) White Paper*, 2002.
- [12] S. Vazquez, S. M. Lukic, E. Galvan, L. G. Franquelo, and J. M. Carrasco, “Energy Storage Systems for Transport and Grid Applications,” *IEEE Transactions on Industrial Electronics*, vol. 57, no. 12, pp. 3881–3895, Dec. 2010.

- [13] Global Wind Energy Council, "Global Wind Report Annual market update," 2011.
- [14] European Photovoltaic Industry Association, "Global Market Outlook for Photovoltaics until 2016," 2012.
- [15] E. Naswali, C. Alexander, H.-Y. Han, D. Naviaux, A. Bistrika, A. von Jouanne, A. Yokochi, and T. K. a. Brekken, "Supercapacitor energy storage for wind energy integration," *2011 IEEE Energy Conversion Congress and Exposition*, pp. 298–305, Sep. 2011.
- [16] M. Bragard, N. Soltau, and S. Thomas, "The balance of renewable sources and user demands in grids: power electronics for modular battery energy storage systems," *Power Electronics, IEEE Transactions on*, vol. 25, no. 12, pp. 3049–3056, 2010.
- [17] A. Oudalov and T. Buehler, "Utility scale applications of energy storage," in , *2008. ENERGY 2008.*, 2008, no. November.
- [18] N. Miller, D. Manz, J. Roedel, P. Marken, and E. Kronbeck, "Utility scale Battery Energy Storage Systems," *IEEE PES General Meeting*, pp. 1–7, Jul. 2010.
- [19] J. Castaneda, J. Enslin, D. Elizondo, N. Abed, and S. Teleke, "Application of STATCOM with energy storage for wind farm integration," *Ieee Pes T&D 2010*, pp. 1–6, 2010.
- [20] A. Y. Saber and G. K. Venayagamoorthy, "Optimization of vehicle-to-grid scheduling in constrained parking lots," in *Power & Energy Society General Meeting, 2009. PES '09. IEEE*, 2009, pp. 1–8.
- [21] L. Malesani, L. Rossetto, and P. Tenti, "Active power filter with hybrid energy storage," *IEEE Transactions on Power Electronics*, vol. 6, no. 3, pp. 392–397, Jul. 1991.
- [22] F. Carastro, M. Sumner, and P. Zanchetta, "An Enhanced Shunt Active Filter with Energy Storage for Microgrids," in *2008 IEEE Industry Applications Society Annual Meeting*, 2008, pp. 1–7.
- [23] F. Carastro and M. Sumner, "Mitigation of voltage dips and voltage harmonics within a micro-grid, using a single shunt active filter with energy storage," in *IEEE Industrial Electronics, IECON 2006 - 32nd Annual Conference on*, 2006, vol. 00, pp. 2546–2551.
- [24] H. Tappeiner, "Progressive UPS-technology," *Telecommunications Energy Conference, 1985. INTELEC '85. Seventh International*, pp. 99–102, 1985.

- [25] V. John and N. Mohan, "Standby power supply with high frequency isolation," *Proceedings of 1995 IEEE Applied Power Electronics Conference and Exposition - APEC '95*, pp. 990–994, 1995.
- [26] M. James, "Development and Experience of UPS Systems During the 1970's," in *Telecommunications Energy Conference, 1981. INTELEC 1981. Third International*, 1981, pp. 201–204.
- [27] S. Bai, Y. Du, and S. Lukic, "Optimum design of an EV/PHEV charging station with DC bus and storage system," in *IEEE 2010 Energy Conversion Congress and Exposition (ECCE)*, 2010, pp. 1178–1184.
- [28] B. Parkhideh, H. Mirzaee, R. Beddingfield, and S. Bhattacharya, "Enabling energy storage integration in high power multi-motor applications with active filter solutions," in *Industry Applications Society Annual Meeting (IAS), 2011 IEEE*, 2011, pp. 1–5.
- [29] B. Parkhideh, H. Mirzaee, and S. Bhattacharya, "Hybrid front end converters for large multi-motor applications integrated with energy storage," *2012 Twenty-Seventh Annual IEEE Applied Power Electronics Conference and Exposition (APEC)*, pp. 607–614, Feb. 2012.
- [30] J. Barrado, "Standalone self-excited induction generator with a three-phase four-wire active filter and energy storage system," in *Industrial Electronics, 2007. ISIE 2007. IEEE International Symposium on*, 2007, pp. 600–605.
- [31] E. Cready, J. Lippert, J. Pihl, I. Weinstock, P. Symons, and R. G. Jungst, "Technical and economic feasibility of applying used EV batteries in stationary applications," *Sandia Report, SAND2002-4084*, 2003.
- [32] V. Sithimolada, "Facility-level DC vs. typical ac distribution for data centers: A comparative reliability study," *TENCON 2010-2010 IEEE Region*, pp. 2102–2107, 2010.
- [33] H. Zhang, F. Mollet, C. Saudemont, and B. Robyns, "Experimental Validation of Energy Storage System Management Strategies for a Local DC Distribution System of More Electric Aircraft," *IEEE Transactions on Industrial Electronics*, vol. 57, no. 12, pp. 3905–3916, Dec. 2010.
- [34] SAE Std. J1772, *SAE Electric Vehicle Conductive Charge Coupler*. 2001.
- [35] CHAdeMO Association, "CHAdeMO Protocol." [Online]. Available: <http://www.chademo.com>.

- [36] D. Aggeler, F. Canales, H. Zelaya, D. La Parra, A. Coccia, N. Butcher, and O. Apeldoorn, "Ultra-fast DC-charge infrastructures for EV-mobility and future smart grids," in *2010 IEEE PES Innovative Smart Grid Technologies Conference Europe (ISGT Europe)*, 2010, pp. 1–8.
- [37] IEEE Std. 141-1993, *IEEE Recommended Practice for Electric Power Distribution for Industrial Plants*. 1993.
- [38] Y. Du, X. Zhou, S. Bai, S. Lukic, and A. Q. Huang, "Review of non-isolated bi-directional DC-DC converters for plug-in hybrid electric vehicle charge station application at municipal parking decks," in *2010 Twenty-Fifth Annual IEEE Applied Power Electronics Conference and Exposition (APEC)*, 2010, no. 1, pp. 1145–1151.
- [39] Y. Du, S. Lukic, B. Jacobson, and A. Huang, "Review of high power isolated bi-directional DC-DC converters for PHEV/EV DC charging infrastructure," *2011 IEEE Energy Conversion Congress and Exposition*, pp. 553–560, Sep. 2011.
- [40] *IEEE recommended practices and requirements for harmonic control in electrical power systems*. IEEE Std. 519-1992, 1993.
- [41] R. Crosier, S. Wang, and M. Jamshidi, "A 4800-V grid-connected electric vehicle charging station that provides STACOM-APF functions with a bi-directional, multi-level, cascaded converter," in *2012 Twenty-Seventh Annual IEEE Applied Power Electronics Conference and Exposition (APEC)*, 2012, pp. 1508–1515.
- [42] S. Wang, R. Crosier, and Y. Chu, "Investigating the power architectures and circuit topologies for megawatt superfast electric vehicle charging stations with enhanced grid support functionality," in *2012 IEEE International Electric Vehicle Conference*, 2012, pp. 1–8.
- [43] B. M. Grainger, A. R. Sparacino, R. J. Kerestes, and M. J. Korytowski, "Advancements in medium voltage DC architecture development with applications for powering electric vehicle charging stations," in *Energytech, 2012 IEEE*, 2012, pp. 1–8.
- [44] M. Vasiladiotis, A. Rufer, and A. Beguin, "Modular converter architecture for medium voltage ultra fast EV charging stations: Global system considerations," in *2012 IEEE International Electric Vehicle Conference*, 2012, pp. 1–7.
- [45] G. Gamboa, C. Hamilton, R. Kerley, S. Elmes, A. Arias, J. Shen, and I. Batarseh, "Control strategy of a multi-port, grid connected, direct-DC PV charging station for plug-in electric vehicles," in *2010 IEEE Energy Conversion Congress and Exposition*, 2010, pp. 1173–1177.

- [46] ANSI C84.1, *American National Standard for Electric Power Systems and Equipment—Voltage Ratings (60 Hertz)*. 2006.
- [47] D. A. Paice, *Power Electronic Converter Harmonics: Multipulse methods for clean power*. New York: IEEE Press, 1995.
- [48] Y. H. Liu, N. R. Watson, and J. Arrillaga, “A new concept for the control of the harmonic content of voltage source converters,” in *Power Electronics and Drive Systems, 2003. PEDS 2003. The Fifth International Conference on*, 2003, vol. 1, pp. 793–798.
- [49] S. Choi, P. N. Enjeti, H. H. Lee, and I. J. Pitel, “A new active interphase reactor for 12-pulse rectifiers provides clean power utility interface,” *Industry Applications, IEEE Transactions on*, vol. 32, no. 6, pp. 1304–1311, 1996.
- [50] S. Miyairi, S. Iida, K. Nakata, and S. Masukawa, “New method for reducing harmonics involved in input and output of rectifier with interphase transformer,” *IEEE Transactions on Industry Applications*, vol. IA-22, no. 5, pp. 790–797, Sep. 1986.
- [51] S. Fukuda, M. Ohta, and Y. Iwaji, “An auxiliary-supply-assisted harmonic reduction scheme for 12-pulse diode rectifiers,” *IEEE Transactions on Power Electronics*, vol. 23, no. 3, pp. 1270–1277, May 2008.
- [52] M. E. Villablanca, J. I. Nadal, and M. a. Bravo, “A 12-pulse AC–DC rectifier with high-quality input/output waveforms,” *IEEE Transactions on Power Electronics*, vol. 22, no. 5, pp. 1875–1881, Sep. 2007.
- [53] S. Bai and S. Lukic, “New method to achieve AC harmonic elimination and energy storage integration for 12-Pulse diode rectifiers,” *Industrial Electronics, IEEE Transactions on*, vol. in Press.
- [54] S. Bai and S. Lukic, “Design considerations for DC charging station for plug-in vehicles,” in *IEEE 2011 Vehicle Power and Propulsion Conference (VPPC)*, 2011, pp. 1–6.
- [55] D. Rendusara, a. von Jouanne, P. Enjeti, and D. a. Paice, “Design considerations for six pulse and twelve pulse diode rectifier systems operating under voltage unbalance and pre-existing voltage distortion with some corrective measures,” *IAS '95. Conference Record of the 1995 IEEE Industry Applications Conference Thirtieth IAS Annual Meeting*, pp. 2549–2556, 1995.
- [56] R. W. Erickson and D. Maksimovic, *Fundamentals of Power Electronics*, Second Edi. Springer Science+Business Media, 2001.

- [57] H. Fujita, "A practical approach to harmonic compensation in power systems-series connection of passive and active filters," *Industry Applications, IEEE Transactions*, vol. 21, no. 6, pp. 1020–1025, 1991.
- [58] J.-H. Sung, S. Park, and K. Nam, "New hybrid parallel active filter configuration minimizing active filter size," in *Electric Power Applications, IEE Proceedings*, 2000, pp. 93–98.
- [59] S. Dewan, "Design of an input filter for the six-pulse bridge rectifier," *Industry Applications, IEEE Transactions on*, vol. 21, no. 5, pp. 1168–1175, Sep. 1985.
- [60] P. Cheng and S. Bhattacharya, "Application of dominant harmonic active filter system with 12 pulse nonlinear loads," *Power Delivery, IEEE Transactions on*, vol. 14, no. 2, pp. 642–647, 1999.
- [61] J. Sung and S. Park, "New hybrid parallel active filter configuration minimising active filter size," *Electric Power Applications, IEE*, vol. 147, pp. 93–98, 2000.
- [62] P. a. Dahono, Y. R. Bahar, Y. Sato, and T. Kataoka, "Damping of transient oscillations on the output LC filter of PWM inverters by using a virtual resistor," *4th IEEE International Conference on Power Electronics and Drive Systems*, vol. 1, pp. 403–407, 2001.
- [63] P. A. Dahono, "A control method to damp oscillation in the input LC filter of AC-DC PWM converters," in *IEEE Power Electronics Specialists Conference*, 2002, pp. 1630–1635.
- [64] Z. Pantic and S. M. Lukic, "Framework and Topology for Active Tuning of Parallel Compensated Receivers in Power Transfer Systems," *IEEE Transactions on Power Electronics*, vol. 27, no. 11, pp. 4503–4513, Nov. 2012.
- [65] Q. Lei, F. Peng, and S. Yang, "Multiloop Control Method for High-Performance Microgrid Inverter Through Load Voltage and Current Decoupling With Only Output Voltage Feedback," *IEEE Transactions on Power Electronics*, vol. 26, no. 3, pp. 953–960, 2011.
- [66] B. Mather and D. Maksimovic, "A simple digital power-factor correction rectifier controller," *IEEE Transactions on Power Electronics*, vol. 26, no. 1, pp. 9–19, 2011.
- [67] H. Akagi and R. Kitada, "Control and Design of a Modular Multilevel Cascade BTB System Using Bidirectional Isolated DC/DC Converters," *IEEE Transactions on Power Electronics*, vol. 26, no. 9, pp. 2457–2464, Sep. 2011.

- [68] J. Chatzakis, "Designing a new generalized battery management system," *IEEE Transactions on Industrial Electronics*, vol. 50, no. 5, pp. 990–999, 2003.
- [69] N. H. Kutkut, H. L. N. Wiegman, D. M. Divan, and D. W. Novotny, "Design considerations for charge equalization of an electric vehicle battery system," *IEEE Transactions on Industry Applications*, vol. 35, no. 1, pp. 28–35, 1999.
- [70] C. Lin and H. Chao, "Battery management system with dual-balancing mechanism for LiFePO<sub>4</sub> battery module," *TENCON 2011 - 2011 IEEE Region 10 Conference*, pp. 863–867, Nov. 2011.
- [71] H. Park, C. Kim, and K. Park, "Design of a charge equalizer based on battery modularization," *IEEE Transactions on Vehicular Technology*, vol. 58, no. 7, pp. 3216–3223, 2009.
- [72] A. Nourai, "Community Energy Storage (CES): A Game Changer," 2009.
- [73] D. Rastler, "Electricity energy storage technology options: a white paper primer on applications, costs and benefits," 2010.
- [74] P. Thomas, "Demonstration of Community Energy Storage fleet for load leveling, reactive power compensation, and reliability improvement," in *IEEE Power and Energy Society General Meeting*, 2012, pp. 1–4.
- [75] O. C. Onar, M. Starke, G. P. Andrews, and R. Jackson, "Modeling, controls, and applications of community energy storage systems with used EV/PHEV batteries," *2012 IEEE Transportation Electrification Conference and Expo (ITEC)*, pp. 1–6, Jun. 2012.
- [76] Y. Luh, C. Pan, and J. Su, "A study on modular design representation," *2007 IEEE International Conference on Industrial Engineering and Engineering Management*, pp. 1327–1331, Dec. 2007.
- [77] A. K. W. Lau, "Managing modular product design: Critical factors and a managerial guide," *PICMET '09 - 2009 Portland International Conference on Management of Engineering & Technology*, pp. 2045–2057, Aug. 2009.
- [78] G. Dupont and P. Baltus, "Dimensioning and grid integration of mega battery energy storage system for system load leveling," in *PowerTech, 2009 IEEE Bucharest*, 2009, pp. 1–6.
- [79] K. Mattern, A. Ellis, and S. Williams, "Application of inverter-based systems for peak shaving and reactive power management," in *Transmission and Distribution Conference and Exposition, 2008. IEEE/PES*, 2008, pp. 1–4.

- [80] Y. Du, M. Wang, R. T. Meitl, S. Lukic, and A. Q. Huang, "High-frequency high-efficiency DC-DC converter for distributed energy storage modularization," *IECON 2010 - 36th Annual Conference on IEEE Industrial Electronics Society*, pp. 1832–1837, Nov. 2010.
- [81] Z. Wang and H. Li, "A Soft switching three-phase current-fed bidirectional DC-DC converter with high efficiency over a wide input voltage range," *Power Electronics, IEEE Transactions on*, vol. 27, no. 2, pp. 669–684, 2012.
- [82] L. Liu, H. Li, Z. Wu, and Y. Zhou, "A Cascaded Photovoltaic System Integrating Segmented Energy Storages With Self-Regulating Power Allocation Control and Wide Range Reactive Power Compensation," *IEEE Transactions on Power Electronics*, vol. 26, no. 12, pp. 3545–3559, Dec. 2011.
- [83] O. Alonso, P. Sanchis, and E. Gubia, "Cascaded H-bridge multilevel converter for grid connected photovoltaic generators with independent maximum power point tracking of each solar array," *Power Electronics*, vol. 2, pp. 731–735, 2003.
- [84] E. Villanueva, "Control of a single-phase cascaded H-bridge multilevel inverter for grid-connected photovoltaic systems," *Industrial Electronics, IEEE Transactions on*, vol. 56, no. 11, pp. 4399–4406, 2009.
- [85] J. A. Barrena, L. Marroyo, M. A. R. Vidal, and J. R. T. Apraiz, "Individual Voltage Balancing Strategy for PWM Cascaded H-Bridge Converter-Based STATCOM," *Industrial Electronics, IEEE Transactions on*, vol. 55, no. 1, pp. 21–29, 2008.
- [86] A. Dell'Aquila, M. Liserre, V. G. Monopoli, and P. Rotondo, "Overview of PI-based solutions for the control of DC buses of a single-phase H-bridge multilevel active rectifier," *Industry Applications, IEEE Transactions on*, vol. 44, no. 3, pp. 857–866, 2008.
- [87] S. Essakiappan, H. S. Krishnamoorthy, P. Enjeti, R. S. Balog, and S. Ahmed, "Independent control of series connected utility scale multilevel photovoltaic inverters," *2012 IEEE Energy Conversion Congress and Exposition (ECCE)*, pp. 1760–1766, Sep. 2012.
- [88] L. Gong, K. Dai, J. Chen, Y. Huang, and Y. Kang, "Design and implementation of distributed control system for cascaded H-Bridge multilevel STATCOM," *IEEE Applied Power Electronics Conference and Exposition (APEC)*, pp. 1544–1551, Mar. 2011.
- [89] R. Teodorescu, F. Blaabjerg, M. Liserre, and P. Loh, "Proportional-resonant controllers and filters for grid-connected voltage-source converters," *IEE Proceedings on Electric Power Applications*, vol. 153, no. 5, 2006.

- [90] Y. Sato, T. Ishizuka, K. Nezu, and T. Kataoka, "A new control strategy for voltage-type PWM rectifiers to realize zero steady-state control error in input current," *IEEE Transactions on Industry Applications*, vol. 34, no. 3, pp. 480–486, 1998.
- [91] Y. Tzou, "DSP-based fully digital control of a PWM DC-AC converter for AC voltage regulation," *IEEE Electronics Specialists Conference, 1995. PESC'95 ...*, pp. 138–144, 1995.
- [92] D. G. Holmes, "Analysis of multi-loop control strategies for power conversion applications," *38th IAS Annual Meeting on Conference Record of the Industry Applications Conference, 2003.*, vol. 3, pp. 1778–1785, 2003.
- [93] M. Liserre, F. Blaabjerg, and S. Hansen, "Design and control of an LCL-filter-based three-phase active rectifier," *IEEE Transactions on Industry Applications*, vol. 41, no. 5, pp. 1281–1291, 2005.
- [94] C. Wessels, J. Dannehl, and F. W. Fuchs, "Active damping of LCL-filter resonance based on virtual resistor for PWM rectifiers — stability analysis with different filter parameters," in *2008 IEEE Power Electronics Specialists Conference, 2008*, pp. 3532–3538.
- [95] B.-G. Cho, S.-K. Sul, H. Yoo, and S.-M. Lee, "LCL Filter Design and Control for Grid-connected PWM Converter," in *Power Electronics and ECCE Asia (ICPE & ECCE), 2011 IEEE 8th International Conference on*, 2011, pp. 756–763.
- [96] T. H. Kim, S. H. Kim, B. K. Kwon, and B. S. Kim, "A procedure to design LCL filter for energy storage system," in *8th International Conference on Power Electronics - ECCE Asia*, 2011, no. 1, pp. 2974–2978.
- [97] A. Q. Huang, M. L. Crow, G. T. Heydt, J. P. Zheng, and S. J. Dale, "The Future Renewable Electric Energy Delivery and Management (FREEDM) System: The Energy Internet," *Proceedings of the IEEE*, vol. 99, no. 1, 2010.